UNIVERSITY OF CALIFORNIA
Santa Barbara

Validation of Vegard's Law for Lattice Matching $In_xAl_{1-x}N$ to GaN
&
The MOCVD Growth of $Al_xGa_{1-x}N$/AlN for Deep UV LEDs

A dissertation submitted in partial satisfaction of the
requirements for the degree Doctor of Philosophy
in Materials

by

Humberto Miguel Foronda

Committee in charge:
Professor James Speck, Co-Chair
Professor Steven DenBaars, Co-Chair
Professor Shuji Nakamura
Professor Glenn Beltz

December 2017

The dissertation of Humberto Miguel Foronda is approved.

_____

Professor Glenn Beltz

_____

Professor Shuji Nakamura

_____

Professor Steven DenBaars, Committee Co-Chair

_____

Professor James Speck, Committee Co-Chair

September 2017

Validation of Vegard's Law for Lattice Matching $In_xAl_{1-x}N$ to GaN
&
The MOCVD Growth of $Al_xGa_{1-x}N$/AlN for Deep UV LEDs

Humberto Miguel Foronda

Education

- Ph.D. Materials, University of California, Santa Barbara, 2017
- B.S. Materials Science and Engineering (Cum Laude), Minor: German, University of Florida, 2012

Research Experience

- PhD Candidate, NSF-GRF, Materials Department, UC Santa Barbara, Fall 2012-Present, Thesis Advisor: James Speck and Steven DenBaars
    - National Science Foundation Graduate Research Fellow, 2014
    - MOCVD growth and electrical/microstructural characterization of AlGaN/AlN thin films for UV-C LEDs
    - MOCVD growth and microstructural characterization of InAlN/GaN thin films.
    - Microstructural and mechanical characterization of bulk GaN wafers
    - Designed over 500 MOCVD growth recipes
    - Consultant for UV LEDs for Jonak Law Group, P.C.

- Undergraduate Research Student, Materials Science and Engineering Department, University of Florida, Spring 2009-Summer 2012, Advisor: Jacob L. Jones
    - Processing and property testing of doped lead-free piezoelectric-ceramics
    - U.S. Army Undergrad Research Apprenticeship Program (URAP), Summer 2012
    - Conducted research abroad with International Research Experience for Students (IRES) Program, University of Leoben, Austria, 2011
    - University Scholars Research Program, University of Florida, 2009

Publications

1. **H.M. Foronda**, F.Wu, C. Zollner, M.E. Alif, B. Saifaddin, A. Almogbel, M. Iza, S. Nakamura, S.P. DenBaars, J.S. Speck, Low Threading Dislocation Density Aluminum Nitride on Silicon Carbide Through the Use of Reduced Temperature Interlayers, J. of Cryst. Growth, (in submission), (2017)
2. **H.M. Foronda**, B. Mazumder, E.C. Young, M.A. Laurent, Y.Li, S.P. DenBaars, J.S. Speck, "Analysis of Vegard's Law for lattice Matching InxAl1-xN to GaN by Metalorganic Chemical Vapor Deposition", J. of Cryst. Growth, 475, (2017)
3. S. Marcinkevicius, T. Uzdavinys, **H.M Foronda**, D.A. Cohen, C. Weisbuch, J.S. Speck, "Intervally energy of GaN conduction band measured by femtosecond pump-probe spectroscopy" Phys. Rev. B 94, 235205, (2016)
4. **H.M. Foronda** , A.E. Romanov , E.C. Young , C. Robertson , G.E. Beltz , and J.S. Speck, Curvature and Bow of Bulk GaN Substrates, J. of Appl. Phys., 120, 035104 (2016)
5. **H.M. Foronda**, M.A. Laurent, B. Yonkee, S. Keller, S.P. DenBaars, J.S. Speck, Improving Source Efficiency for AlN by MOCVD, Semiconductor Science and Technology, 31, 8, (2016)

6. **H. Foronda**, M. Deluca, E. Aksel, J.S. Forrester, J.L. Jones, "Thermally-induced loss of piezoelectricity in ferroelectric Na0.5Bi0.5TiO3–BaTiO3"Materials Lett., Vol. 115, Pg.132–135, (2014)
7. E. Aksel, J. S. Forrester, **H. M. Foronda,** R. Dittmer, D. Damjanovic, and J. L. Jones, "Structure and Properties of La-modified Na0.5Bi0.5TiO3 at Ambient and Elevated Temperatures," J. of Appl. Phys., 112, 054111, (2012).
8. **H. Foronda**, E. Aksel, and J. L. Jones, "Phase Purity and Site Selection with Lanthanum Doping in Sodium Bismuth Titanate (Na0.5Bi0.5TiO3) piezoelectric ceramic," University of Florida J. of Undergraduate Research, Vol. 11, No. 4, pp. 1-4 (2010).
9. E. Aksel, **H.Foronda**, K. Calhoun, J.L. Jones, S.Schaab, TGranzow, "Processing and Properties of Na0.5Bi0.5TiO3 Piezeolectric Ceramics Modified with La, Mn, and Fe" Functional Materials Lett., Vol.3, pp. 45-48, (2010)

Presentations

- **H.M. Foronda**, B. Mazumder, E.C. Young, M.A. Laurent, Y.Li, S.P. DenBaars, J.S. Speck, "Analysis of Vegard's Law for lattice Matching InxAl1-xN to GaN by Metalorganic Chemical Vapor Deposition" Oral Presentation in proceedings of Compound Semiconductor Week Conference, Berlin, 2017
- **H.M. Foronda**, M.A. Laurent, B. Yonkee, S. Keller, S.P. DenBaars, J.S. Speck, Improving Source Efficiency for AlN by MOCVD, Oral Presentation in Proceedings of the International Conference for Metalorganic Vapor Epitaxy, San Diego, 2016
- **H.M. Foronda** , A.E. Romanov , E.C. Young , C. Robertson , G.E. Beltz , and J.S. Speck, Curvature and Bow of Bulk GaN Substrates, Oral Presentation in Proceedings of the Compound Semiconductor Week Conference, Toyama, 2016
- **H.M. Foronda,** M.Laurent, B.Yonkee, S. Nakamura, S.DenBaars, J.Speck, Optimizing Aluminum Nitride Buffer Layers on Silicon Carbide for Deep Ultraviolet Light Emitting Diodes, Poster in proceedings with the 2015 IEEE Summer Topicals Meeting, Nassau, 2015

Teaching Experience

- Mentored undergraduate in Research in Science and Engineering (RISE) UCSB 2014
- TA MATRL 101, Introduction to Materials Science, UC Santa Barbara, Winter 2014
- Nominated for GSA Excellence in Teaching Award , Winter 2014
- Trained over 10 incoming graduate students, visiting researchers, and postdocs in MOCVD growth and materials characterization

Awards and Honors

- Outstanding Graduate Student Research Award, UCSB Solid State Lighting and Electronics Center, 2016
- National Science Foundation Graduate Research Fellowship Program (NSF GRFP) 2014
- TELC B2 Examination Certificate in German Language 2010

ABSTRACT

Validation of Vegard's Law for Lattice Matching $In_xAl_{1-x}N$ to GaN
&
The MOCVD Growth of $Al_xGa_{1-x}N$/AlN for Deep UV LEDs

by
Humberto Miguel Foronda

The first section of this thesis presents an experimental investigation for validating Vegard's Law for $In_xAl_{1-x}N$ on GaN. Vegard's law is useful for correlating materials composition and band gap to the a-lattice parameter, however it is primarily utilized for materials synthesized from powders and deviations for InAlN have been reported in the literature. Coherent $In_xAl_{1-x}N$ (x = 0.15 to x = 0.28) films were grown by metalorganic chemical vapor deposition on GaN templates to investigate if the films obey Vegard's Law by comparing the film stress-thickness product from wafer curvature before and after $In_xAl_{1-x}N$ deposition. The In composition and film thickness were verified using atom probe tomography and high resolution x-ray diffraction, respectively. *Ex-situ* curvature measurements were performed to analyze the curvature before and after the $In_xAl_{1-x}N$ deposition. At ~$In_{0.18}Al_{0.82}N$, no change in curvature was observed following InAlN deposition; confirming that the films obey Vegard's law and that ~$In_{0.18}Al_{0.82}N$ is lattice matched to GaN. The relaxed a_0- and c_0- lattice parameters of $In_xAl_{1-x}N$ were experimentally determined and are in agreement with lattice parameters predicted by Vegard's law.

The second section of this thesis will present the growth and characterization of AlGaN/AlN for deep UV LEDs. Growth studies on AlN buffer and n-AlGaN will be discussed. First, we explore the dependence of the interlayer growth temperature on the AlN crystal quality, defect density, and surface morphology. The crystal quality was

characterized using omega rocking curve scans and the threading dislocation density was determined by plan view transmission electron microscopy. The growth resulted in a threading dislocation density (TDD) of 7 x 10^8 cm^{-2}, indicating a significant reduction in the dislocation density of AlN in comparison to direct growth of AlN on SiC (~10^{10}-10^{11} cm^{-2}). Atomic force microscopy images demonstrate a clear step-terrace morphology that is consistent with step flow growth at high temperature. Reducing the interlayer growth temperature increases the TD inclination and thus enhances TD-TD interactions. The TDD is decreased via fusion and annihilation reactions. Following that, we will discuss the growth studies conducted for growing AlGaN. First we will discuss finding the optimal conditions for growing smooth UID-AlGaN for a variety of alloy compositions as the UV LED will need AlGaN with Al% between 40-65%. Then the growth and electrical characterization of n-AlGaN will be discussed. After processing, the electron mobility, resistivity, and carrier concentration of n-$Al_{0.43}Ga_{0.57}N$ was 96 cm^2/Vs, 15 mΩ-cm, and 4 x 10^{18} cm-^{3}, respectively.

Section 1

Chapter 1: Introduction to Indium Aluminum Nitride

Chapter 2: Calculating Indium Composition for $In_xAl_{1-x}N$

Chapter 3: Gallium Nitride as a Substrate or Template?

List of Figure Captions

Chapter 1: Introduction to Indium Aluminum Nitride

Chapter 2: Calculating Indium Composition for $In_xAl_{1-x}N$

Chapter 3: Gallium Nitride as a Substrate or Template?

Chapter 4: Verifying Vegard's Law for $In_xAl_{1-x}N$/GaN

Chapter 5: Introduction to UV LEDs

Chapter 6: Reactor Designs and Substrates

Chapter 7: Growth of AlN

Chapter 8: Growth of AlGaN

Section 1:

Validation of Vegard's Law for Lattice Matching $In_xAl_{1-x}N$ to GaN

Chapter 1: Introduction to Indium Aluminum Nitride

1.1 Properties of Indium Aluminum Nitride

Indium Aluminum Nitride ($In_xAl_{1-x}N$) has a multitude of favorable properties for device applications such as high electron mobility and thermal conductivity [1, 2]. Such applications make this material system useful for high frequency devices and sensors. These properties allow devices to operate at higher temperatures and give breakdown electric field strengths much higher than Si based devices [1]. High quality growth of InAlN material offers large flexibility in device development and applications due to the fact that this ternary alloy spans the extremes of the III- nitrides system.

The direct band gap of $In_xAl_{1-x}N$ material system ranges from 1.9 eV in InN to 6.2 eV in AlN, and can be adjusted to any value within this range by varying the alloy composition, and offers many possibilities for device engineering. This range of band gaps allows InAlN to operate in the red to ultraviolet regions of the spectrum. A major advantage of this material system is that, according to Vegard's law, ~$In_{0.18}Al_{0.82}N$ is lattice matched to GaN as shown in Fig. 1.1, meaning it can be used for device applications [3].

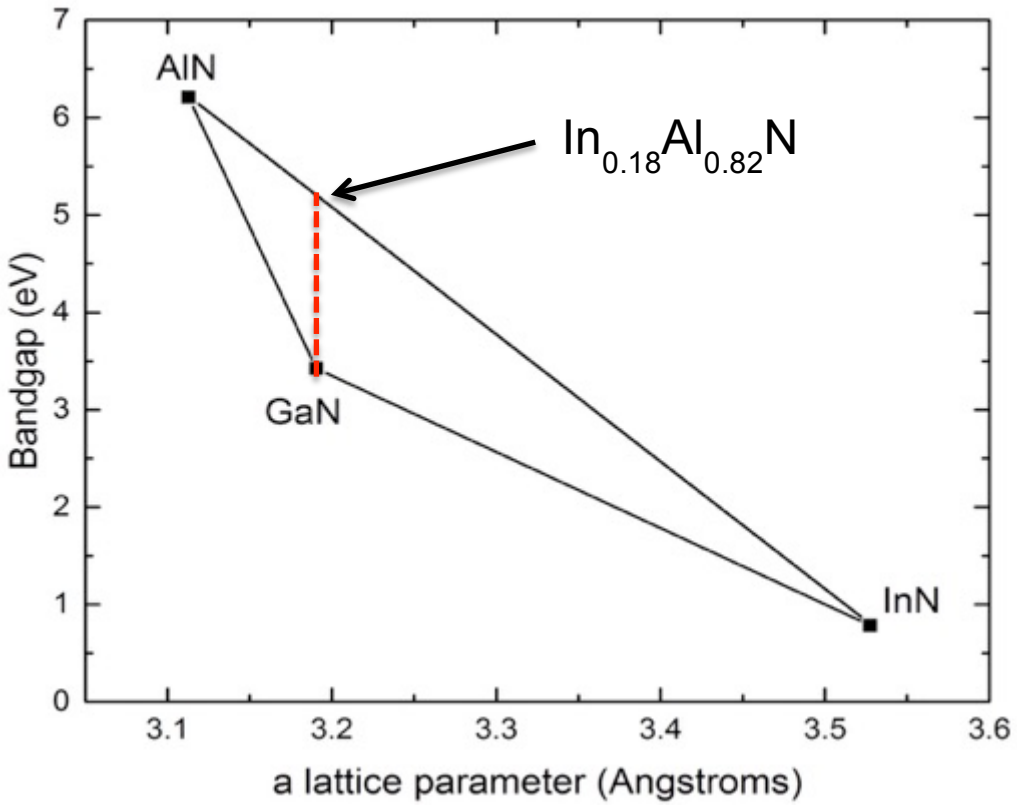

Fig. 1.1 a lattice parameter of AlN, GaN, and InN. The $In_xAl_{1-x}N$ alloy is lattice matched to GaN at an approximate composition of x=0.18.

At ~$In_{0.18}Al_{0.82}N$, the thin film deposited over GaN would contribute no additional stress. When not at the lattice-matched composition, the hetero-epitaxial deposition of $In_xAl_{1-x}N$ on GaN will either cause a tensile or compressive mismatch stress depending on alloy composition. In the case of composite $In_xAl_{1-x}N$/GaN, the addition of the $In_xAl_{1-x}N$ will cause the overall structure's curvature to change. Namely tensile (compressive) stress in the $In_xAl_{1-x}N$ layer causes the curvature to become concave (convex) as shown in Fig. 1.2 a, b, and c. However, given that Vegard's law is primarily utilized for materials synthesized from powders, it is difficult to determine actual materials composition with thin films composed of binary alloys, such as InN and AlN.

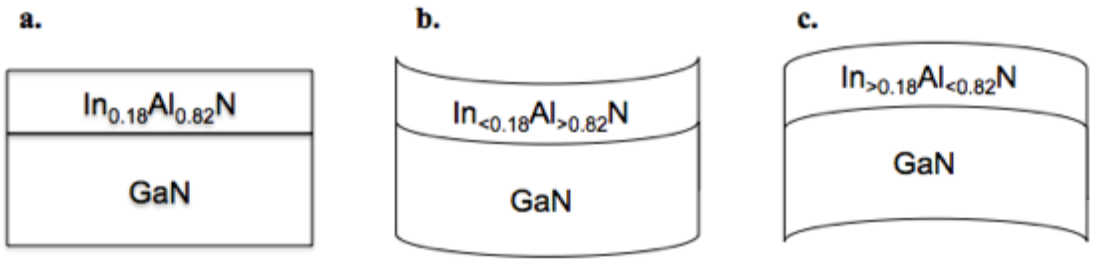

Fig. 1.2 InAlN **(a.)** lattice Matched to GaN **(b.)** concave bending **(c.)** convex bending

Additionally, there are also reports in the literature indicating that pseudomorphic InAlN films show deviations from Vegard's Law [4-7]. Darakchieva *et al* (2008) state that there is a strain-driven deviation of the alloy's lattice parameters from Vegard's Law. Differences in materials composition determined by x-ray diffraction (XRD) and Rutherford backscattering spectrometry (RBS) were discovered for highly strained pseudomorphic Al-rich InAlN films on GaN buffers.

Lorenz *et al* (2006) reports on pseudomorphic InAlN layers grown on GaN buffers that change from tensile to compressive strain with increasing In composition. In this study, they use Monte Carlo simulations to correct channeling results, which give rise to agreement between RBS and XRD strain measurements. They state that materials compositions derived from XRD have limited accuracy due to deviations from Vegard's Law and go on to estimate possible correction factor, which lead to a lattice matched composition of In = 17.1%. Further deviations from Vegard's Law are attributed to varying literature values for the in-plane lattice parameter for Wurtzite InN.

Due to the strong bonds between nitrogen and the group III atoms (approximately 2-3 eV), the InAlN material system is physically and chemically stable. In ambient

conditions, group III-nitrides crystallize in a hexagonal, wurtzite crystal structure with the space group $P6_3mc$ (C^4_{6v}). Thin films tend to crystallize in the zinc blende crystal structure with the space group F43m (T_d^2). The crystal structure of wurtzite and zinc blende are shown below in Figs 1.3a and b.

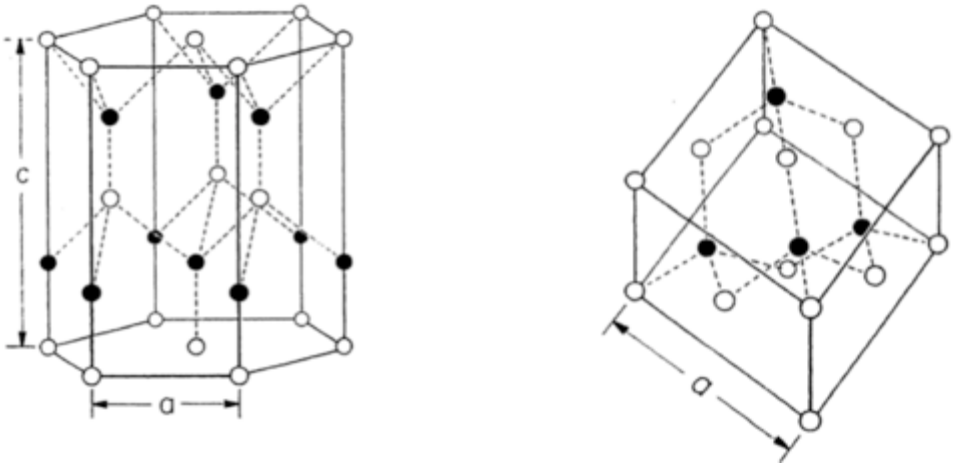

Fig. 1.3 (a) Wurtzite crystal structure, (b) zinc blend crystal Structure

$In_xAl_{1-x}N$ has not been extensively studied compared to Indium Gallium Nitride (InGaN) or Aluminum Gallium Nitride (AlGaN) due to the difficulty in growing epitaxial, high quality $In_xAl_{1-x}N$ by metal organic chemical vapor deposition (MOCVD) or molecular beam epitaxy (MBE). This is attributed to the large lattice mismatch between AlN (3.112 Å) and InN (3.545 Å), leading to inhomogeneity in the microstructure and composition [8]. The large growth temperature difference between AlN (~1100 °C) and InN (~600 °C) also presents a challenge in growing high quality $In_xAl_{1-x}N$ by MOCVD [9]. This leads to thermal instability resulting from the spinodal phase separation phenomenon, which is more prominent in InAlN than other nitride alloys such as InGaN.

1.2 MOCVD Growth of $In_xAl_{1-x}N$

The most common deposition techniques are MBE and MOCVD. Both techniques have advantages and disadvantages, however in this thesis the focus will be on MOCVD. The growth studies shown in this chapter are from the literature, primarily work done here at UC Santa Barbara on the Veeco P-75 Turbodisc reactor, and were useful in developing the $In_xAl_{1-x}N$ layers for the verification of Vegard's Law.

MBE deposits epitaxial thin films by condensing thermally generated molecular beams, which originate from evaporation cells within an ultra-high vacuum chamber onto a heated substrate. The major advantage of MBE is that it has the capability of growing single monolayer thick heterostructures. *In-situ* film characterization is an advantage of MBE as well as real time growth monitoring by reflection high-energy electron diffraction (RHEED). The disadvantage to MBE is the high cost of operation and maintenance, and the low growth rate.

In MOVCD, metal organic reactants in the gas phase flow over a heated substrate and adsorb onto the substrate, where they diffuse along the substrate surface and react during nucleation and film growth. After growth, volatile and hazardous reaction products desorb from the surface and are vented out. It is important to understand that growth via MOCVD is a non-equilibrium process that is governed by mass flow transport and kinetics. The factors that influence the stoichiometry of the epitaxial film are the gas concentrations and the substrate surface temperature. These factors also influence the quality of the epitaxial film and the ability of the hazardous reaction products to desorb. When high gas concentrations are introduced, the film has a higher chance of

contamination due to gas phase nucleation. At low growth temperatures, the surface diffusion is slow in comparison to the rate of atoms reaching the surface. This usually creates films that are amorphous. At high growth temperatures, surface diffusion occurs relatively quickly compared to the atoms reaching the surface, thus giving the atoms enough time to diffuse to step growth sites and produce crystalline films [8]. The precursors used for InAlN are TrimethylIndium (TMIn), TrimethylAluminum (TMAl), and Ammonia (NH_3).

$In_xAl_{1-x}N$ materials system was grown on GaN. The orientation of GaN will alter the growth conditions and properties, which can either, be an advantage or disadvantage to the system. The orientations of interest are polar, nonpolar, and semipolar; as shown in Fig. 1.4. The polar plane is the basal (0001) c-plane. The non-polar m-plane is orthogonal to the polar c-plane as shown in the Fig.1.4. Semipolar planes are the planes between the c-plane and nonpolar planes.

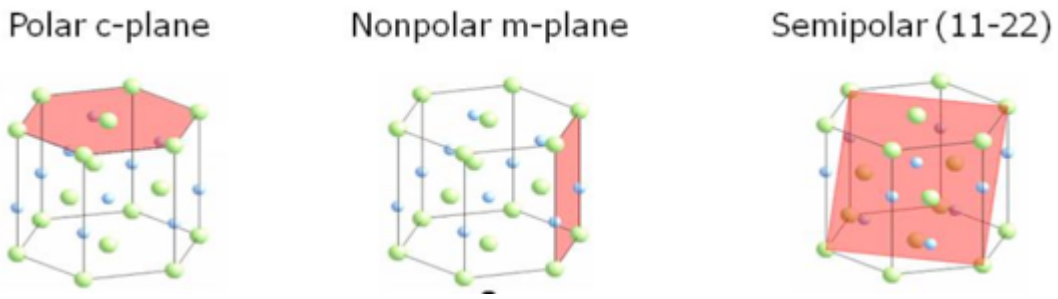

Fig. 1.4 Polar, nonpolar, and semipolar orientations of the wurtzite structure.

Light emitting didoes (LEDs) grown along the c-plane direction generally suffer from discontinuities in the spontaneous polarization and piezoelectric fields. These

discontinuities cause band bending and separate the electrons in the conductions band from the holes in the valence band, which ends up reducing the radiative recombination efficiency; this is known as the quantum confined stark effect (QCSE). LEDs grown on nonpolar and semipolar GaN substrates have been shown to reduce these polarization effects [10-12].

In the following sections of this chapter, the growth of InAlN by MOCVD will be discussed. Growths on varying orientations, impurity incorporation, and changing growth parameters will be examined. These studies in this chapter were done by Dr. Roy Chung and are a great guideline for growing InAlN on the Veeco P-75 Turbodisc reactor. For further details on the growth of this material system, please take a look at his thesis [2].

1.2.1 Growth Conditions on c-Plane

Unintentionally doped (UID) GaN as a pseudo substrate is grown on (0001) sapphire, this is known as a GaN template. $In_xAl_{1-x}N$ is then deposited under various growth conditions. The effect on TMIn and TMAl on indium incorporation is vital to understanding and optimizing the growth of $In_xAl_{1-x}N$. Fig. 1.5 illustrates how the indium composition (orange) and growth rate (blue) varies with respect to changing the flow rate of TMAl and holding TMIn constant, and vice-versa. [13,14].

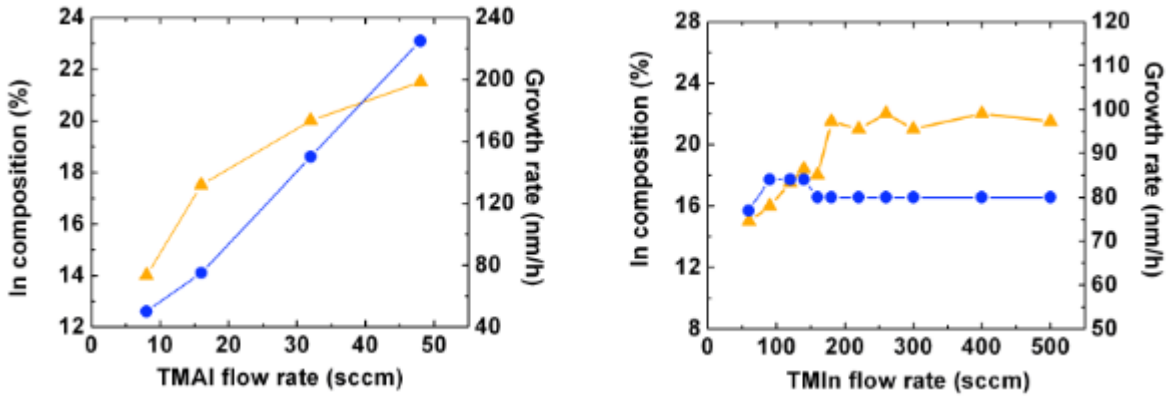

Fig. 1.5 Indium composition and MOCVD growth rate with respect to varying TMAl and TMIn flow rates [2].

The indium composition increases with increasing flow rate of TMAl at a fixed flow rate of 120 sccm for TMIn at a growth temperature of 800 °C. This can be accredited to the increased growth rate suppressing indium desorption, which is also seen in InGaN growth via MOCVD [13,14]. Increasing the flow rate of TMIn at a fixed value of TMAl (16 sccm at a growth temperature of 800 °C) increased the indium composition, however it saturated at approximately 200 sccm as did the growth rate. A Langmuir adsorption model can be used to explain the saturation of the indium incorporation with the increasing flow rate of TMIn.

Fig. 1.6a and b shows how the indium incorporation varies in the InAlN film with respect to changing the flow rates of ammonia and hydrogen, respectively by Chung *et al*. The orange line is once again the indium composition and the blue line is the growth rate. Fig. 1.6a shows how increasing the flow rate of ammonia increases the indium incorporation; however, the growth rate remains relatively constant. This implies that an increased ammonia flow rate suppresses indium desorption. The lack of change in the growth rate implies that for all the ammonia flow rates, the pre-reactions between TMAl and NH_3 were negligible [15]. Fig. 1.6b shows the effect of the hydrogen flow rate on

InAlN. There is a decrease in the indium composition with respect to increasing the hydrogen flow rate and the growth rate remains constant. This is similar to the effect of varying the flow rate of hydrogen in InGaN, as it also limited the indium incorporation. Therefore, it can be noted that the growth characteristics of InAlN are very similar to that of InGaN. The window for optimal growth for high quality InAlN on GaN is therefore narrower because of the differences in the growth environment of InN and AlN.

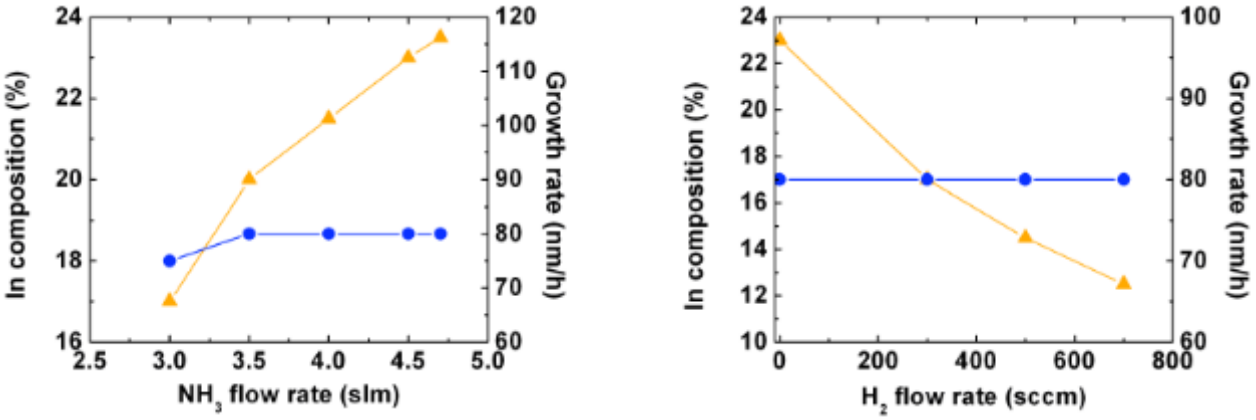

Fig. 2.6 Dependence of indium composition and growth rate with respect to varying (a) ammonia and (b) hydrogen flow [2].

1.2.2.Impurity Incorporation in InAlN

InAlN is expected to have higher impurity incorporation in comparison with InGaN or AlGaN due to its narrow growth regime described earlier because of its low growth temperature and low growth pressure [16]. The impurities are predominantly carbon and oxygen. The carbon incorporation comes from the metalorganic precursors, as an excessive amount of TMIn compared to TMAl is used. The adsorption of the carbon impurities is enhanced in the system due to the combination of low growth temperature, high Al composition and high partial pressures of TMIn. Fig. 1.7 shows a plot of the impurity concentration (carbon and oxygen) with respect to growth pressure

(ranging from 40 to 140 Torr) for ~$In_{0.18}Al_{0.82}N$ by Chung *et al*. One can note from the plot that the carbon impurities in InAlN grown under 140 torr were much higher than the carbon impurity concentration at 70 torr. The oxygen concentration on the other hand was not strongly affected by the growth pressure. The AFM image belongs to the surface of the InAlN sample grown at 70 torr, where the increase in carbon concentration begins.

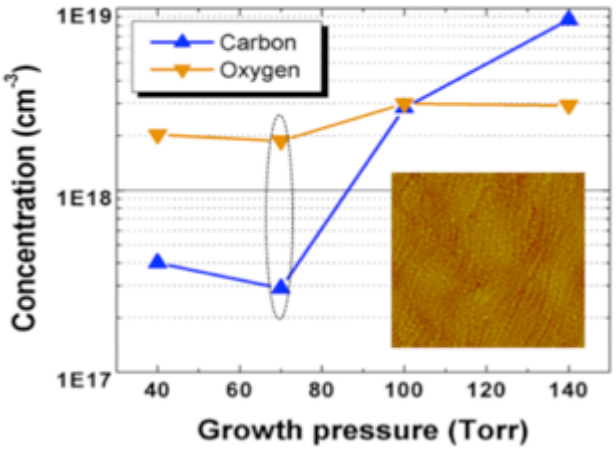

Fig. 1.7 Dependence of unintentional carbon and oxygen concentration with growth pressure for $In_{0.18}Al_{0.82}N$ [2].

Fig. 1.8 shows the carbon and oxygen concentrations as a function of growth pressure by Chung *et al*, however in this case it ranged from 120 to 320 torr. One can note that at higher growth pressures, neither carbon nor oxygen concentrations were seriously affected by the growth pressure. This indicates that the carbon concentration is affected by low growth pressures and eventually saturates at higher growth pressures, while oxygen is barely affected and remains constant at approximately ~10^{18} cm^3. The reduced carbon impurity concentration in InAlN at growth pressures below 100 torr is believed to be due the low ambient pressures resulting in an increased desorption of CH_3 groups from the surface.

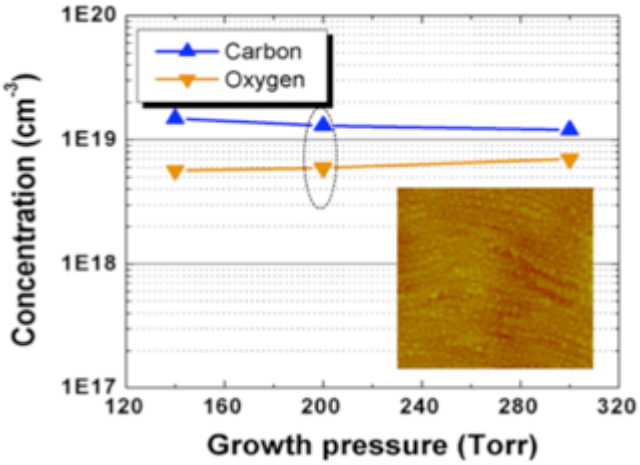

Fig. 1.8 Dependence of unintentional carbon and oxygen concentration on growth pressure in $In_{0.18}Al_{0.82}N$ films for high growth pressures [2].

Fig. 1.9 shows the impurity concentrations with respect to growth rate by Chung *et al*. There is an increase in the carbon concentration with respect to growth rate, until it reaches 150 nm/hr, where it saturates. The oxygen concentration once again remains fairly unchanged. This increase in carbon concentration is similar to the addition of TMIn, where a higher concentration of CH_3 molecules leads to an increased C incorporation into the films.

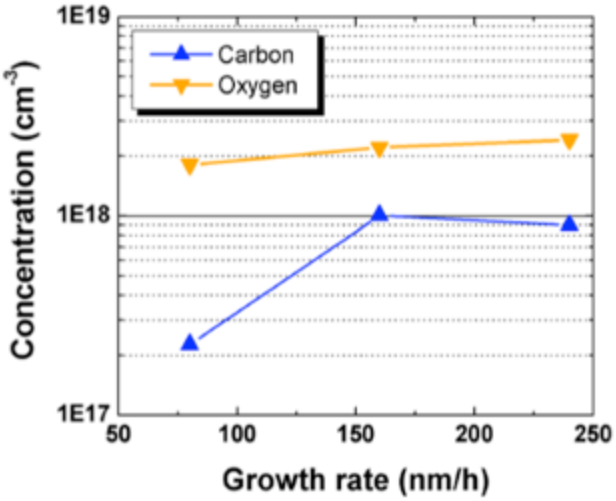

Fig. 1.9 Dependence of unintentional carbon and oxygen concentration on growth rate in $In_{0.18}Al_{0.82}N$ films for high growth pressures [2].

In general, the oxygen concentration is not strongly affected by either the growth pressure or growth rate and is maintained fairly constant throughout. In the case of InAlN, the oxygen impurity concentration is quite high, values greater than 1 x 10^{18} cm^{-3} were reported. The high oxygen concentration in the MOCVD InAlN is attributed to the strong affinity of oxygen to aluminum, which occurs at low growth temperatures, around 800 °C, and at high Al compositions. The InAlN materials systems oxidize when there is a high Al composition.

1.2.3 Growth of Semipolar InAlN on Bulk GaN substrates

Up to now we have discussed c-plane (polar) InAlN, which is closely lattice matched to a pseudo GaN template on a sapphire substrate. The lattice matching of InAlN to GaN, while maintaining a large bandgap energy and low refractive index around 2.2 at 420 nm, is a striking and prominent characteristic. However, the problem with c-plane InAlN is that the crystal quality degrades quickly when the composition is varied and when certain growth conditions, such as growth rate, are varied. When the indium composition is below 18%, tensile stress is introduced in the film and at around 13%, and therefore cracks. In order to attain an indium composition greater than 22%, the growth temperature must be decreased, however this would in turn reduce the surface mobility of the aluminum adatoms and create surface roughness.

The focus will now switch to semipolar InAlN. In comparison to epitaxial growth, the semipolar plane has certain benefits over c-plane [17-19]. A major advantage for

semipolar InAlN is that in this system, it has been experimentally and theoretically proven that the indium incorporation efficiency is greater than on c-plane. So, growing semipolar InAlN would provide a larger range of growth conditions, since it can be grown at higher temperatures while maintaining the same indium composition and also higher growth rates. Semipolar InAlN could also be less constrained in composition due to strain relaxation from shear stresses in the semipolar orientation with c-plane inclined, which could prevent InAlN from cracking, even at low indium compositions [20,21].

Fig. 1.10 shows the dependence of indium composition of semipolar (11-22) InAlN on growth temperature by Chung et al. One can note that there is a fairly linear decrease in the indium composition as the growth temperature increased, with a change in slope at 780 °C where the decrease slows down. The growth temperature was higher by about 10-15°C than that of c-plane InAlN. The growth rate of semipolar InAlN was also greater than that of c-plane InAlN (both grown under the same conditions) due to the fact that there was greater indium incorporation efficiency because of the improved growth temperature values.

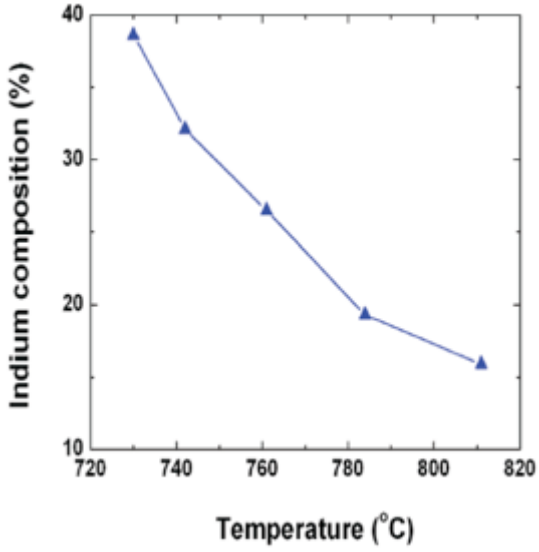

Fig. 1.10 Dependence of indium composition on the MOCVD growth temperature for s-plane InAlN [2].

1.3 Indium Aluminum Nitride in Device Applications

InAlN is promising for high electron mobility transistors (HEMT) applications as a barrier material, due to its large bandgap and lattice matching capabilities with GaN [22,23]. InAlN also has a large refractive index to GaN ($(\Delta n/n \sim 7$ % at 420 nm). Because of this, high quality laser diodes with n-type $In_{0.18}Al_{0.82}N$ cladding have shown improvements in threshold current density. High quality $In_{0.18}Al_{0.82}N$ distributed bragg reflector (DBR) lasers have also been achieved as well as micro-cavity LEDs [24]. InAlN can be oxidized because of its high aluminum content, which can then be wet etched using potassium hydroxide (KOH) solution. Oxidized InAlN layers are currently being used as micro-disk surface emitting lasers and as air gap optical confinement layers in laser diodes [24].

1.3.1 Indium Aluminum Nitride Based Active Layer

Photoluminescence (PL) measurements examine the optical properties of emitters. An example of indium in the active region is shown in Fig. 1.11 [2]. A multi-quantum well structure was grown by Chung *et al* on a GaN template on a c-plane sapphire substrate. The quantum well region contains 1.5 nm $In_{0.18}Al_{0.82}N$ and the barrier contains 5nm thick $Al_{0.52}Ga_{0.48}N$. The PL measured a peak emission wavelength at 330 nm using an excitement laser with a wavelength of 193 nm. It can be noted from the PL that the MQW has a broad full width half max (FWHM) and low intensity, indicating that the optical property of the system is not sufficient for an active layer. The cause of such poor results is most likely due to a high concentration of point defects, i.e. vacancies and impurities, for example oxygen and carbon impurity concentrations. Electroluminescence (EL) was unsuccessful for this wavelength/ sample structure.

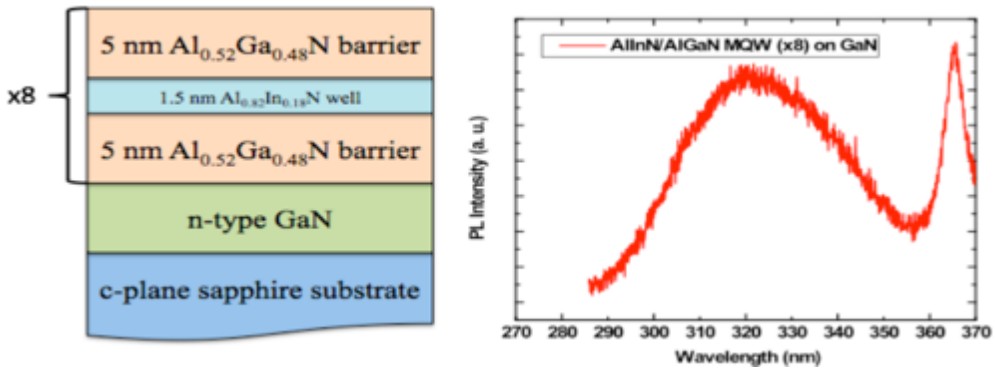

Fig. 1.11 Device structure with $In_{0.18}Al_{0.82}N$ quantum wells alongside respective PL measurement [2].

Similar experiments have been performed on semi-polar (11-22) LEDs with InAlN in the well and GaN in the barrier of the active region. Given that longer wavelengths were targeted, EL from InAlN could now be measured. Fig. 1.12 shows a

simple LED structure with InAlN in the well as described previously, with the peak wavelength emission around 420 nm at 30mA. This corresponds to an In composition around 25-30%. The results show that the current was taken up to 140 mA with no wavelength shift in the EL. For a similar composition in InGaN, a blue shift in wavelength emission would be observed on a semimpolar plane, due to band filling [25].

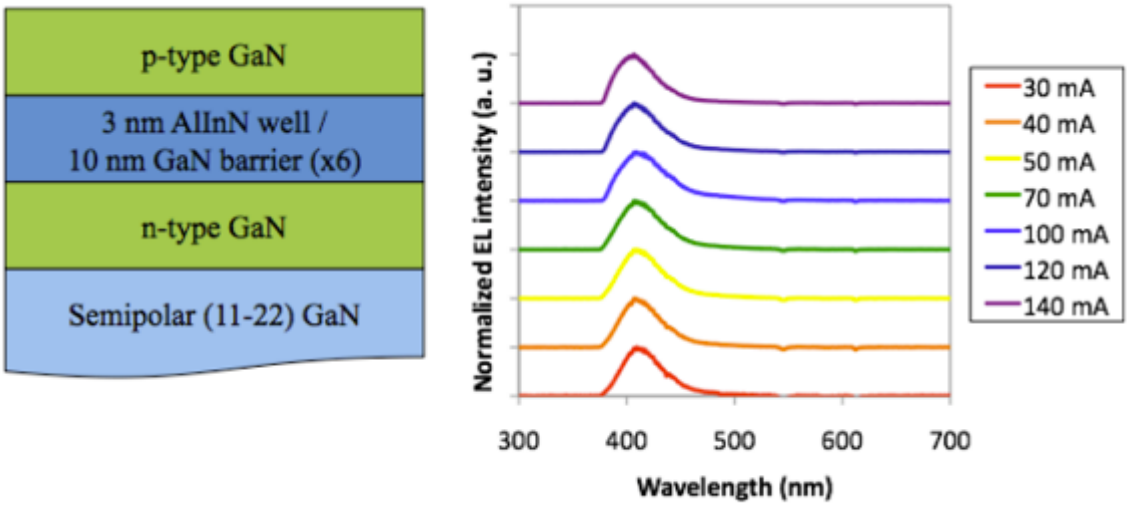

Fig. 1.12 Schematic diagram of semipolar (11-22) LEDs with InAlN active layer, and EL spectra at various injected current level [2].

1.3.2 Indium Aluminum Nitride Based Electron Blocking Layers

Electron blocking layers (EBLs), are used in LEDs to decrease the quantity of carrier overflow into p-type GaN from the active region. AlGaN is a materials system used for EBLs in conventional LEDs, however the strong tensile strains associated with increasing Al composition limits the thickness and composition. The crystal quality of the EBL also degrades due to strain relaxation, which is harmful to the performance of the device. Using InAlN as an EBL allows one to avoid these problems as it has a larger band gap and smaller valence offset with respect to GaN, so that there is negligible strain

and large conduction band offset indicating no degradation to the crystal quality [26]. Super lattice electron blocking layers (SL-EBLs) made up of $In_{0.18}Al_{0.82}N$ (2nm) / GaN (2 nm) have been developed by Chung *et al*. It has been shown that increasing the thickness of the InAlN layers gives a higher operating voltage and lower output because of the compensation and structural degradation effects of the layer, and were therefore kept thin. LEDs with SL-EBL operate at comparable voltages and output powers to LEDs with AlGaN EBL and have similar EQEs at lower current densities as shown in Fig. 1.13.

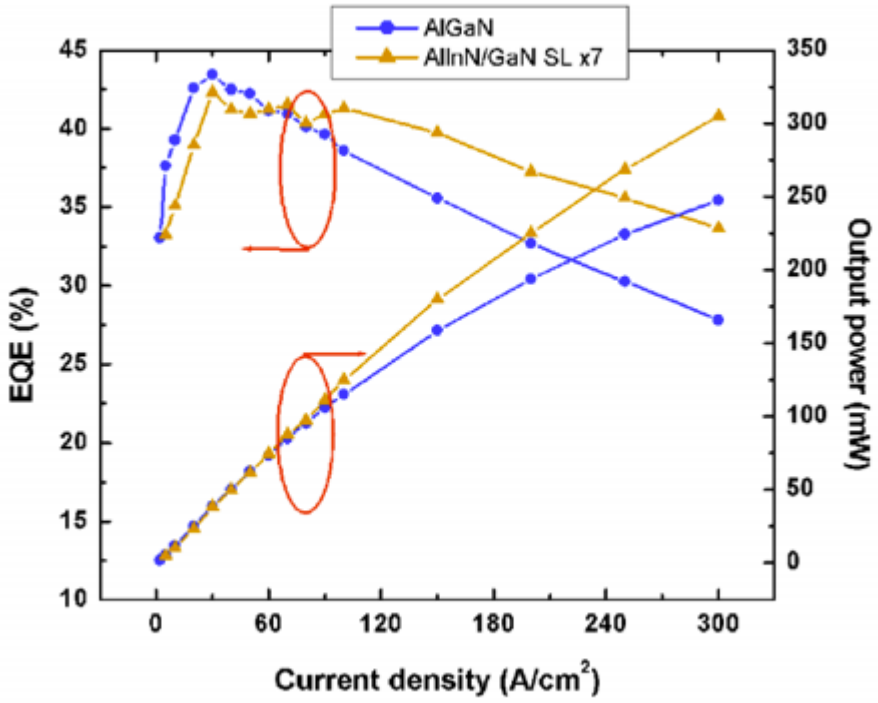

Fig. 1.13 EQE and output power of SL-EBL LEDs (blue) and AlGaN EBL LEDs(orange)as a function of current density [2].

1.4 Section Overview

In the following chapters of this section, an experimental investigation for validating Vegard's Law for $In_xAl_{1-x}N$ to GaN will be discussed. Vegard's law is useful

for correlating materials composition and band gap to the a-lattice parameters. InAlN will be grown by MOCVD with the principles discussed in this chapter.

$In_xAl_{1-x}N$ was grown over a wide composition range (from x= 0.15 to x=0.28) on GaN to investigate if the films obey Vegard's law by comparing the curvature and stress of the films before and after $In_xAl_{1-x}N$ deposition. The study was initially on bulk c-plane GaN substrate, however the high quality freestanding substrates had significant curvature caused by internal stresses from within the substrate, which will be discussed in detail.

After settling on GaN templates on sapphire, The In composition and film thickness of $In_xAl_{1-x}N$ was verified using high resolution x-ray diffraction (HRXRD) from $\omega - 2\theta$ scans in triple axis geometry and were compared with compositional analysis by atom probe tomography (APT). Additionally, reciprocal space maps were used to verify that the films were coherently deposited on the GaN templates.

Ex-situ radius of curvature (R_C) measurements using XRD were performed on the GaN templates and $In_xAl_{1-x}N$ layers to analyze the curvature before and after the $In_xAl_{1-x}N$ deposition. The relaxed a_0- and c_0- lattice parameters of $In_xAl_{1-x}N$ were determined from a combination of the XRD results and linear elasticity for coherent films.

References

[1] M. Lukitsch, Growth and Characterization of Indium Aluminum Nitride Thin Films Grown by Plasma Source Molecular Beam Epitaxy, Wayne State University, (2007)

[2] R.Chung, Comprehensive Material Study of MOCVD grown InAlN And Development of Relaxed Template for Ultraviolet Diode Lasers, (2011)

[3] L. Vegard, Zeitschrift für Physik **5**, 17 (1921)

[4] V Darakchieva, M. Beckers, M.Y. Xie, L. Hultman, B. Monemar,1 J.F. Carlin, E. Feltin, M. Gonschorek, and N. Grandjean, J. of Appl. Phys. **103**, 103513, (2008)

[5] K Lorenz, N. Franco, E. Alves, I. M. Watson, R. W. Martin, and K. P. O'Donnel, Phys. Rev. Lett. **97**, 085501 (2006)

[6] J. Kuzmík, IEEE Electron Device Lett. **22**, 510 (2001).

[7] R Butte, J.F. Carlin, E Feltin, M Gonschorek, S Nicolay, G Christmann, D Simeonov, A Castiglia, J Dorsaz, H J Buehlmann, S Christopoulos, G Baldassarri Hoger von Hogersthal, AJD Grundy, M Mosca, C Pinquier, M.A. Py, F Demangeot, J Frandon, P G Lagoudakis, J J Baumberg and N Grandjean, J. of Phys. D: Appl. Phys. **40**, 6328 (2007)

[8] S.Y. Karpov, N. I. Podolskaya, I.A. Zhmakin, and A.I. Zhmakin, , Phys. Rev. B **70**, 235203(2004)

[9] S. Choi, F. Wu, R. Shivaraman, E. C. Young, J.S. Speck, , Appl. Phys. Lett., **100**, 232102 (2012)

[10] F. Sala, A. Carlo, P. Lugli, F. Bernardini, V. Fiorentini, R. Scholz, and J. Jancu,App. Phys. Lett. **74**, 2002 (1999).

[11] F. Bernardini and V. Fiorentini, Phys. Status Solidi B **216**, 391 (1999).

[12] A.E. Romanov, T.J. Baker, S. Nakamura, and J.S. Speck, J. Appl. Phys. **100**, 023522 (2006).

[13] S. Keller, B. Keller, D. Kapolnek, U. Mishra, S.P. DenBaars, I.K. Shmagin, R.M. Kolbas, and S. Krishnankutty, J. Cryst. Growth **170**, 349 (1997).

[14] F. Jiang, R. Wang, A. Munkholm, S.K. Streiffer, G.B. Stephenson, P.H. Fuoss, K. Latifi, and C. Thompson, Appl. Phys. Lett. **89**, 161915 (2006)

[15] E.L. Piner, M.K. Behbehani, N.A. El-Masry, F.G. McIntosh, J.C. Roberts, K.S. Boutros, and S.M. Bedair, Appl. Phys. Lett. **70**, 461 (1997).

[16] D.D. Koleske, A.E. Wickenden, R.L. Henry, and M.E. Twigg, J. Crystal Growth **242**, 55 (2002).

[17] T. Akiyama, T. Yamashita, K. Nakamura, and T. Ito, Jap. J. of Appl. Phys. **48**, 120218 (2009).

[18] J.E. Northrup, Appl. Phys. Lett. **95**, 133107(2009).

[19] H. Sato, R.B. Chung, H. Hirasawa, N. Fellows, H. Masui, F. Wu, M. Saito, K. Fujito, J.S. Speck, S.P. Denbaars, and S. Nakamura, Appl. Phys. Lett. **92**, 221110 (2008).

[20] A. Tyagi, F. Wu, E.C. Young, A. Chakraborty, H. Ohta, R. Bhat, K. Fujito, S.P. Denbaars, S. Nakamura, and J.S. Speck, Appl. Phys. Lett. **95**, 251905 (2009).

[21] M.T. Bulsara, V. Yang, A. Thilderkvist, E.A. Fitzgerald, K. Haüsler, and K. Eberl, J. Appl. Phys. **83**, 592 (1998).

[22] M. Gonschorek, J.F. Carlin, E. Feltin, M.A. Py, N. Grandjean, V. Darakchieva, B. Monemar, M. Lorenz, and G. Ramm, J. Appl. Phys. **103**, 093714 (2008).

[23] R. Butté, J.F. Carlin, E. Feltin, M. Gonschorek, S. Nicolay, G. Christmann, D. Simeonov, and N. Grandjean, J. Phys. D: Appl. Phys.**40**, 6328 (2007).

[24] A. Castiglia, E. Feltin, G. Cosendey, A. Altoukhov, J. -F. Carlin, R. Butté, and N. Grandjean, Appl. Phys. Lett. **94**, 193506 (2009).

[25] M.J. Galtrey, R.A. Oliver, M.J. Kappers, C. Mcaleese, D. Zhu, C.J. Humphreys, P.H. Clifton, D. Larson, and A. Cerezo, Appl. Phys. Lett. **92**, 041904 (2008)

[26] A.T. Cheng, Y.K. Su, and W.C. Lai, Phys. Status Solidi C **5**, 1685 (2008).

Chapter 2: Calculating Indium Composition for $In_xAl_{1-x}N$

As mentioned previously in Chapter 1, our goal is to verify if Vegard's Law is valid for the InAlN materials system deposited on GaN. Therefore we must be confident that we are investigating the correct alloy composition and how it relates to GaN. We must also have a strong understanding of how to determine the alloy composition. $In_xAl_{1-x}N$ grown over a wide composition range is necessary to observe a change from tensile to compressive mismatch stress when deposited on GaN. However, before investigating whether the thin films bend as predicated by Vegard's law, it is important to verify that we get an accurate determination of the alloy compositions for the $In_xAl_{1-x}N$ thin films. Therefore, before investigating if the films obeys Vegard's law by comparing the curvature and stress of the films before and after $In_xAl_{1-x}N$ deposition, the alloy composition must be verified by experimental methods.

Four $In_xAl_{1-x}N$ thin films on GaN were grown by MOCVD. Al-rich, In-rich and the lattice-matched InAlN composition to GaN were targeted. The MOCVD growth was performed in a Veeco P-75 Turbodisc reactor. The precursors for $In_xAl_{1-x}N$ were trimethylindium (TMIn), trimethylaluminum (TMAl) and Ammonia (NH_3).

2.1 $\omega - 2\theta$ Scan

The approximate indium composition and thickness of the $In_xAl_{1-x}N$ thin films can be experimentally determined using high resolution x-ray diffraction (HRXRD) from $\omega - 2\theta$ scans for the (0002) reflection using a Panalytical X'Pert Materials Research Diffractometer (MRD) in triple axis geometry. The incident beam is a Ge (220) two

bounce Bartels monochromator with a pre-collimating mirror. The diffracted beam optics used is a Ge (220) triple bounce analyzer crystal.

Fig. 2.1 is the structure which was grown for the study, and will be discussed in detail later on. Fig. 2.2 displays the $\omega - 2\theta$ scans for the (0002) reflection of GaN, where GaN was the substrate peak and the $In_xAl_{1-x}N$ films were the layer peaks. The four samples grown for this study were plotted alongside each other. Note the shift in the $In_xAl_{1-x}N$ peak to the smaller 2θ values thus indicating an increasing c lattice constant as the indium composition increased.

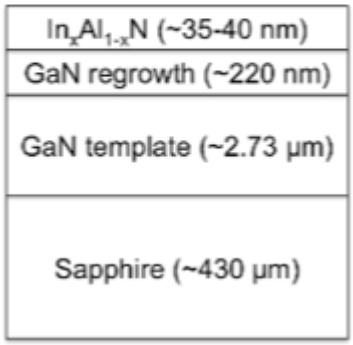

Fig. 2.1 $In_xAl_{1-x}N$ and GaN buffer layer deposited on GaN template

We determined the alloy composition by assuming a coherent InAlN film and then taking the separation between the GaN substrate peak and the $In_xAl_{1-x}N$ layer peak, which is the change in 2θ in Fig. 2.1; and using the tabulated elastic constants from Wright *et al* [1,2]. The indium compositions using this method are 15.32%, 19.35%, 23.31%, and 27.65%,

The indium composition was also determined using the software package X'Pert Epitaxy, which simulates diffraction patterns based on the Takagi-Taupin equations of

dynamical X-ray scattering. The nominal indium composition varies incrementally (15%, 19%, 22%, 28%), in agreement with the calculation taking into account the peak separation between the substrate and layer peak.

It is important to note however that these initial compositions are assuming coherently strained films with relaxed lattice constants that follow Vegard's Law. Therefore before we can verify whether Vegard's Law holds for these films, we must first check to see if the films are pseudomorphic to GaN, and then determine the indium composition independent of Vegard's Law, as this is the law that we are trying to prove and apply to the $In_xAl_{1-x}N$ materials system in the first place.

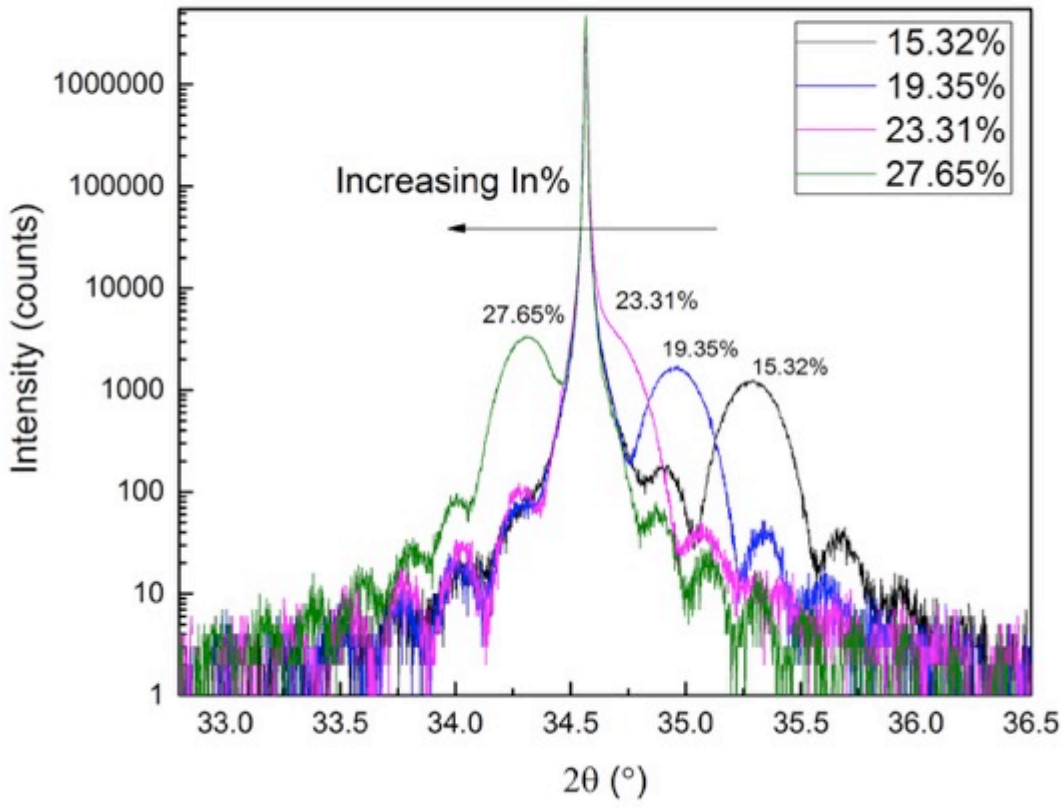

Fig. 2.2 High resolution $\omega - 2\theta$ scans from $In_xAl_{1-x}N$ films with nominal composition from 15% In to 28% In.

2.2 Determining Coherency of $In_xAl_{1-x}N$ films on GaN

In the previous section, we had to assume a coherently strained thin film on GaN to determine the alloy composition by HRXRD. To verify this assumption, one must use a reciprocal space map (RSM) to determine if the film ($In_xAl_{1-x}N$) is pseudomoprhic to the much thicker template/substrate (GaN). Reciprocal space maps (RSMs) were recorded using a Panalytical X'Pert Materials Research Diffractometer using a 3D Pixcel Detector. The incident beam was a Ge (220) two bounce Bartels monochromator with a pre-collimating mirror.

Fig. 2.3 displays the reciprocal space maps for the $(10\bar{1}5)$ reflection for the four indium composition grown. This reflection was chosen so as to have adequate separation between the film and substrate peak as shown in the Fig 2.3. The horizontal streak in the GaN peak is an artifact of the XRD measurement using the Pixcel detector, which is optically similar to a triple axis diffractometer. As a result an analyzer streak is visible along 2θ [3].

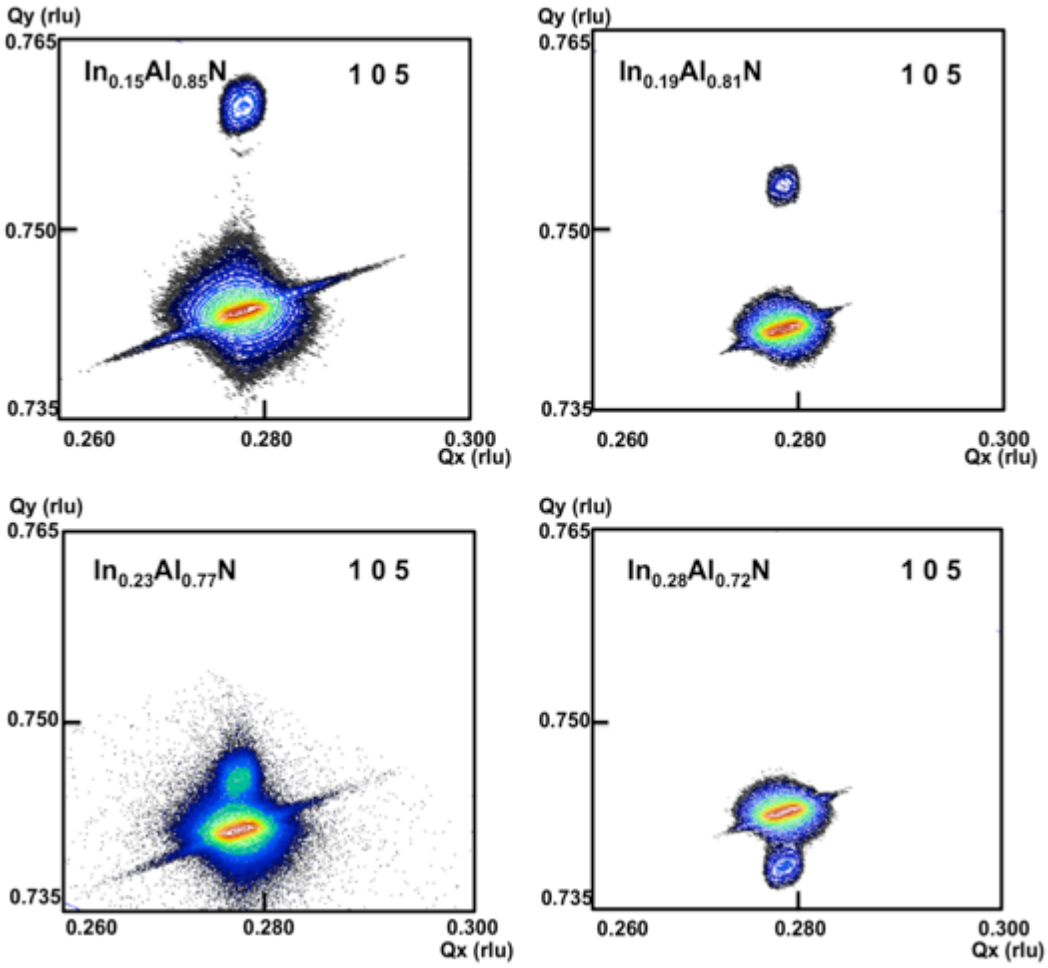

Fig 2.3 Reciprocal space maps of $In_xAl_{1-x}N$ with nominal compositions x = 0.15, 0.19, 0.23, and 0.28. The scan was performed using the (105) orientation of GaN. Positions in Q_x & Q_y are reciprocal lattice units that relate to the tilt of the planes.

The larger peak with the analyzer streak is GaN for all cases and one can see that it does not change position, as expected. The smaller peak is layer peak ($In_xAl_{1-x}N$) and it changes its Q_y position as the alloy composition is changed, however the Q_x value remains the same for all compositions. Additionally, the GaN peak and the $In_xAl_{1-x}N$ peak have approximately the same Q_x value for all four compositions shown. This indicates that the $In_xAl_{1-x}N$ film is pseudomorphic to the GaN in all cases, regardless of

composition. The $In_xAl_{1-x}N$ is coherently strained to GaN primarily because for all cases they are thin, approximately 35 nm for the four samples grown in this study. Similar scans have been done in the literature to verify coherency for $In_xAl_{1-x}N$ on GaN for a variety of compositions. [4-6]

2.3 Determining Materials Composition via Atom Probe Tomography

Now that we have verified that our $In_xAl_{1-x}N$ films are coherent to GaN, which was an assumption made in a previous section; we can focus on determining the alloy composition independent of Vegard's Law. In order to do this we will use Atom Probe Tomography (APT). Professor Baishahki Mazumder did the APT measurements when she was a post doc here at UCSB.

Atom probes are unlike scanning electron microscopes, because the magnification effect comes from the small radius of curvature at the simple tip, rather than an electron beam. The method is destructive in nature removing ions from a sample surface in order to image and identify them. Through coupling of this magnification method with time of flight mass spectrometry, ions evaporated by electric pulses can have their mass-to-charge ratio computed [7]. Through successive evaporation of material, layers of atoms are removed from a specimen, allowing for probing not only of the surface, but also through the material itself [8]. Computer methods are utilized to rebuild a three-dimensional view of the sample, prior to it being evaporated, providing atomic scale information on the structure of a sample, as well as providing the type atomic species information [9]. The instrument allows the three-dimensional reconstruction of up to billions of atoms from a sharp tip.

To perform APT specimen preparation, an additional GaN layer (200 nm) followed by Ni cap layer (50 nm) was deposited on the $In_xAl_{1-x}N$/GaN heterostructures as shown in Fig. 2.4. An FEI Nova Nanolab 200 FIB system was employed to prepare needle-shaped atom probe specimens by a liftout and annular milling method similar to that described by Thompson *et al* [10]. The analysis was carried out in a Local Electrode Atom Probe (LEAP) 3000X HR from CAMECA, operated in laser pulsing mode (green laser $\lambda \sim 532$ nm). All specimens were maintained at a base temperature of 30 K under ultrahigh vacuum ($<10^{-11}$ mbar). A standing voltage of a few kV, which was close to the threshold needed for field evaporation, was applied to each specimen. To achieve controlled field evaporation from the surface of each specimen, a laser pulse energy of 0.3-0.5 pJ with pulsing frequency of 200 kHz was used with an average detection rate of 0.005 atoms/pulse. APT conditions were the same for all specimens. The atom position of field evaporated ions and time of flight were recorded by a position sensitive detector, and the reconstruction was performed using CAMECA Image Visualization and Analysis Software (IVAS). The instrumentation details and reconstruction algorithms are discussed in the literature [11-13]. Several measurements were taken to ensure reproducibility of the data; however, only the most representative data sets from each sample are reported here.

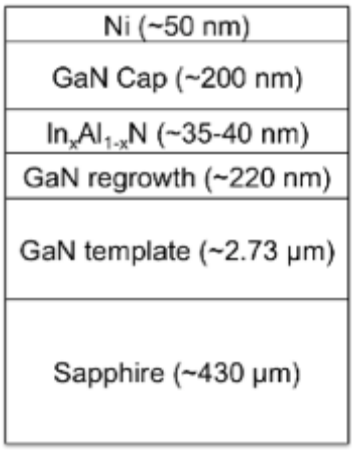

Fig. 2.4 200 nm GaN cap and 50 nm of Ni over structure B for APT.

Fig. 2.5 shows the depth dependence of the layer composition, as determined from atom probe tomography. Fig. 2.5 a, c, and e are the 3D elemental maps of GaN/$In_xAl_{1-x}N$/GaN stack with nominal compositions: In = 15%; 19%; and 28%, respectively. Blue, red and purple dots represent Ga, Al and In atoms, respectively. Fig. 2.5 b, d and f are the 1D composition profiles corresponding to Fig. 2.5 a, c, and e respectively.

A distinct layer of $In_{0.15}Al_{0.85}N$ having a nominal thickness of 35 nm grown on GaN is shown in Fig 2.5a. The group III-site concentrations of each layers were calculated for the mentioned volume shown in Fig. 2.5a and plotted in Fig. 2.5b. Similarly a distinct layer of $In_{0.19}Al_{0.81}N$ and $In_{0.28}Al_{0.72}N$ with thickness ~ 35 nm are shown in Fig. 2.5c and Fig. 2.5e, respectively. The group III-site concentrations of volume shown in Fig. 2.5c and 2.5e are plotted in Fig. 2.5d and 2.5f, respectively. These results show that target In composition (x = 15-28%) for each layer agree with the compositions determined from high resolution X-ray diffraction, which assume Vegard's Law and are plotted alongside each other in Table 2.1.

Table 2.1: In composition with HRXRD and APT

In % HRXRD	In % APT
15.32	15
19.35	19
23.31	N/A
27.65	28

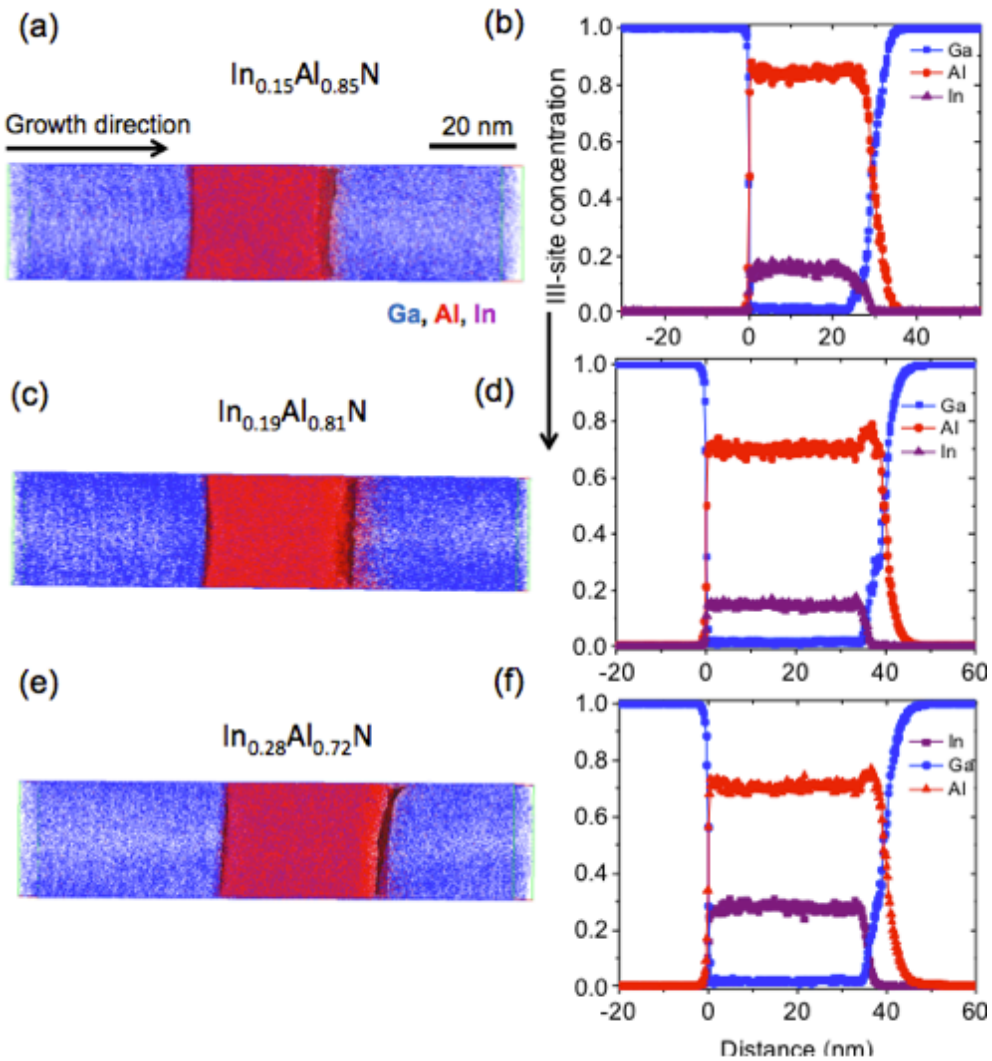

Fig. 2.5. Atom probe analysis of $In_xAl_{1-x}N$. (a),(c), (e) are the 3D elemental maps of GaN/$In_xAl_{1-x}N$/GaN stack with In compositions of 15%; 19%; and 28%, respectively.

(b), (d), and (f) are the 1D composition profiles corresponding to (a) ,(c), (e), respectively.

2.4 Conclusions

A series of $In_xAl_{1-x}N$ thin films with x=15-28% were deposited by MOCVD on GaN. The In composition and film thickness of $In_xAl_{1-x}N$ was determined using HRXRD from $\omega - 2\theta$ scans in triple axis geometry. APT was used alongside HRXRD to verify the In compositions and film thicknesses of the $In_xAl_{1-x}N$. Additionally, reciprocal space maps were used to verify that the films were coherently to the underlying GaN.

References

[1] G. Bauer and W. Richter, Optical characterization of epitaxial semiconductor layers High Resolution X-Ray Diffraction, Berlin: Springer, Ch. 6, (1996)

[2] A. F. Wright, J. Appl. Phys. **82**, 2833 (1997)

[3] T. Boettcher, S. Einfeldt, S. Figge, R. Chierchia, H. Heinke, and D. Hommel, J. S. Speck, Appl. Phys. Lett. **78**, 14 (2001)

[4] V. Darakchieva, M. Beckers, M.Y. Xie, L. Hultman, B. Monemar, J.F. Carlin, E. Feltin, M. Gonschorek, and N. Grandjean, J. of Appl. Phys. **103**, 103513 (2008)

[5] K Lorenz, N. Franco, E. Alves, I. M. Watson, R. W. Martin, and K. P. O'Donnell, Phys. Rev. Lett. **97**, 085501 (2006)

[6] R Butte, J.F. Carlin, E Feltin, M Gonschorek, S Nicolay, G Christmann, D Simeonov, A Castiglia, J Dorsaz, H J Buehlmann, S Christopoulos, G Baldassarri Hoger von Hogersthal, A.J.D. Grundy, M Mosca, C Pinquier, M.A. Py, F Demangeot, J Frandon, P G Lagoudakis, J J Baumberg, N Grandjean, J. of Phys. D: Appl. Phys. **40**, 6328 (2007)

[7] E.W. Müller, "The Atom-Probe Field Ion Microscope". Naturwissenschaften. **5**, 222 (1970)

[8] M. Miller, G. Smith, MRS. ISBN 0-931837-99-5, (1989).

[9] M. Miller, Atom Probe Tomography: Analysis at the Atomic Level. Kluwer Academic/Plenum Publishers. ISBN 0-306-46415-2, (2000).

[10] K. Thompson, D. Lawrence, D.J. Larson, J.D. Olson, T.F. Kelly, B. Gorman, Ultramicroscopy, **107**, 131 (2007)

[11] T. F. Kelly and D. J. Larson, Mater. Charact. **44**, 59 (2000).

[12] P. Bas, A. Bostel, B. Deconihout, and D. Blavette, Appl. Surf. Sci. **298,** 87 (1995).

[13] B. P. Geiser, D. J. Larson, S. S. A. Gerstl, D. Reinhard, T. F. Kelly, T. J. Prosa, and J. D. Olson, Microsc. Microanal. **15**, 302 (2009).

Chapter 3: Gallium Nitride as a Substrate or Template?

Gallium Nitride (GaN) is a binary III-V direct band-gap semiconductor material with a Wurtzite crystal structure. GaN-based device structures have traditionally been grown heteroepitaxially on sapphire or silicon carbide substrates. However, large lattice mismatch between GaN and these foreign substrates yield threading dislocation (TD) densities (TDDs) up to 10^8-10^9 cm^{-2} [1]. Studies have shown that TDs in GaN are electrically active and detrimental to carrier transport in emission properties of semiconductor heterostructures [2-7].

Prior to analyzing the stress state and curvature of the $In_xAl_{1-x}N$ layers, the growth of GaN and its contribution to the curvature and stress state to the overall structure must be determined. The options are GaN as a thick template (2 micron) on a sapphire substrate or a bulk c-plane commercial GaN substrate. In this chapter, we will focus on the substrate selection process along with the advantages and disadvantages for both methods and how to apply it to verifying Vegard's Law. Additionally, we will discuss how we measure the ex-situ radius of curvature (R_C) for GaN, given that at UCSB we do not have in-situ monitoring capabilities for our MOCVDs to measure the curvature and strain state during growth.

3.1 Bulk c-plane GaN vs. GaN Templates on Sapphire

Reports in literature show that there have been successful methods to grow bulk GaN by the ammonothermal method, the sodium (Na)-flux method, and hydride vapor phase epitaxy (HVPE), with reduced TDD (10^3-10^6 cm^{-2}) [8-13]. The ammonothermal method has produced very high quality, low TDD ($<10^4$ cm^{-2}) GaN wafers; however,

poor growth rates (<4 μm/hr) and purity issues limited the commercial availability of ammonothermal substrates. Imanishi *et al* (2015) has demonstrated GaN crystals with TDD ~10^3 cm^{-2} via Na-flux growth [14], however challenges with the Na-flux method are primarily the feasibility for upscaling and cost.

The majority of commercially available c-plane bulk GaN is grown by HVPE, with TDD on the order of 10^4 cm^{-2} to 10^6 cm^{-2}. An advantage over other methods is its high growth rate (>100 μm/hr), which is approximately two orders of magnitude greater than the ammonothermal and Na-flux method [15]. This achievement has led to suitable GaN substrates for GaN laser diodes (LDs), light emitting diodes (LEDs), and vertical power electronic devices.

A major drawback to using c-plane bulk GaN is the price. Depending on the suppliers, 2-inch wafers can cost as much as a couple thousand dollars. From a research stand point this is not practical, given that growth runs must be calibrated and substrate pieces are very valuable to come by. This is where GaN templates on sapphire come into play. Though their TDD can be up to 10^8-10^9 cm^{-2}, they are much more affordable than bulk c-plane GaN, and there is no worry of running out of sample pieces or size of a sample for calibration runs. However, in order to properly select between HVPE GaN and GaN templates on sapphire for the InAlN Vegard's Law verification, we must look at the radius of curvature.

3.1.1 Ex-Situ Radius of Curvature measurement for GaN

Research grade GaN crystals from the commercial vendors Nanowin, Furukawa, Mitsubishi Chemical Company (MCC), and Hitachi Cable, designated as samples A, B,

C, and D, respectively, were acquired. All substrates were c-plane (0001). The substrate thicknesses were 300 μm, 630 μm, 420 μm, and 400 μm, respectively. A GaN template on sapphire was also acquired to compare alongside the bulk GaN substrates. The GaN template was grown as described by Nakamura *et al* (1991) [16], employing a low temperature (450-600 °C) GaN buffer layer and a GaN film grown between 1050-1100 °C, with a total thickness of approximately 2.73 μm. The MOCVD growth was performed in a Veeco P-75 Turbodisc reactor. All growths were performed on flat (0001) sapphire substrates (430 μm). The precursors used for the GaN template were trimethylgallium (TMGa) and ammonia (NH_3).

The radius of curvature was measured by XRD using a Rigaku Smartlab high-resolution x-ray diffractometer. The Rigaku diffractometer is a horizontal θ-θ diffractometer, which facilitates wafer placement on the stage to be free of constraints that otherwise may impact the curvature. An open detector in double axis configuration with a Ge (220) 4 bounce monochromator was used to create a parallel incident beam. A 3x5 mesh with 3.5 mm spacing was mapped to measure the R_C as shown in Fig. 3.1. The direction of the scan is along the x direction which is coplanar with the scattering plane that is defined by the incident and scattered wave vector.

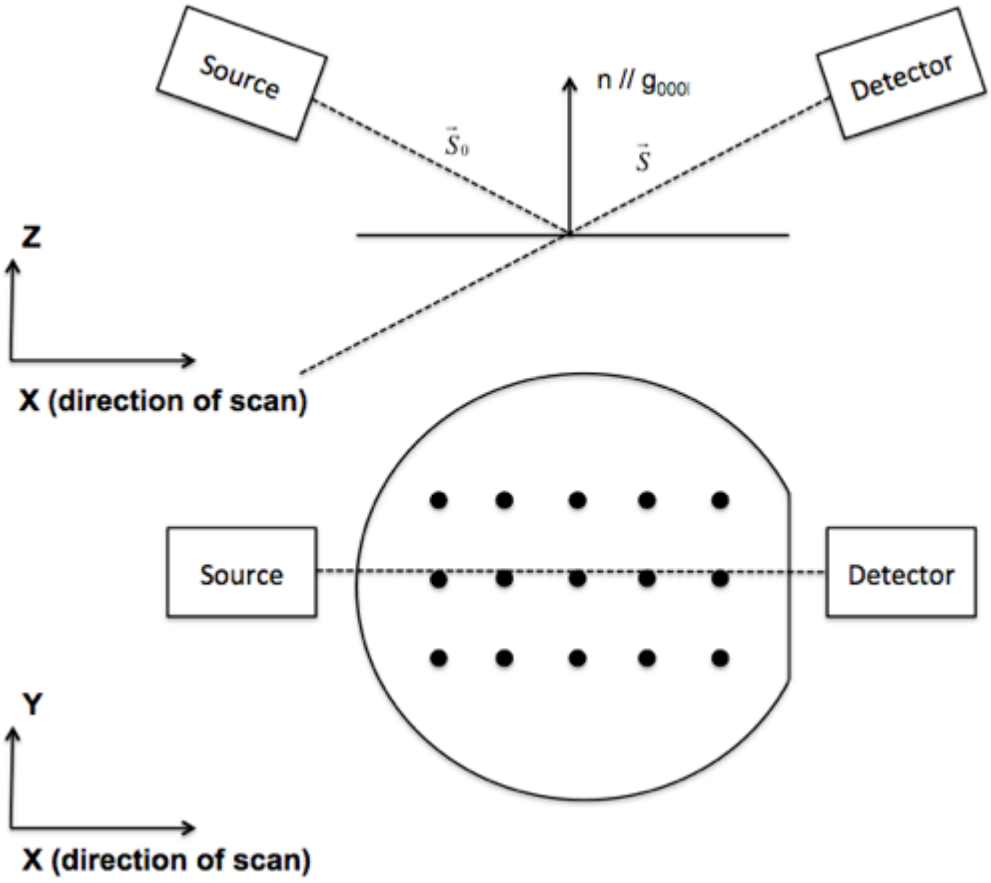

Fig. 3.1 Side view and plan view of Rigaku Diffractometer geometry showing the source, detector and 3x5 mesh with 3.5 mm spacing was mapped onto the Bulk GaN crystal substrate. The plane spanned by S_o and S is referred to as the scattering plane. The translation direction x is in the scattering plane.

The R_C was determined by performing on-axis (0002) omega scans, then translating the sample and measuring the displacement of the omega peak positions. The difference in the incident beam angle from two different regions exposed to x-rays gave the R_C. It is expressed as [17]

$$R_C = \frac{x_2 - x_1}{\omega_2 - \omega_1} \tag{1}$$

where x_1 and x_2 are respective positions along the x-direction and ω_1 and ω_2 are the omega peak positions at those positions.

Table 3.1 displays the radius of curvature of the four commercially available GaN substrates and the GaN template and the measurement's standard error. The surprising result is that the GaN template has the largest radius of curvature when compared alongside the four commercially available GaN substrates. It has a radius of curvature of 10.57± 0.16 m. Substrate A had the largest R_C with the largest standard error, 8.08± 0.97 m. Substrate B and substrate C had similar radii of curvature, 5.42± 0.23 m and 6.44±0.16 m, respectively. The smallest R_C was recorded from substrate D, with 2.75±0.17 m. There is large variability between the GaN substrates ranging from ~ 3 meters to 8 meters. The fact that there is so much variability for the HVPE GaN is particularly surprising because they were grown by the same method (HVPE). Additionally, a lower dislocation density material has improved crystal quality and is assumed to be more flat, i.e. have a larger radius of curvature. In the following section we will discuss the origin of this curvature.

Table 3.1 Radius of Curvature for GaN

Substrate	**Radius of Curvature (m)**	**Standard Error (m)**
Template	10.57	0.16
HVPE-A	8.08	0.97
HVPE-B	5.42	0.23
HVPE-C	6.44	0.16
HVPE-D	2.75	0.17

3.1.2 Analysis of Method to Measure Ex-Situ Radius of Curvature.

Equation 1 can be derived through geometric analysis of the general experimental setup and implementation of basic diffractive principles (Fig. 3.2). Modeling the substrate surface as the circumference of a circle with radius, R, a geometric relationship can be established between the two scan points, 1 and 2, that are Δx apart on the lab horizontal frame. The angle of the incident beam with the lab horizontal is ω, the angle of the incident beam with the crystal vertical is χ, the angle between the lab and crystal horizontals is Φ, and the angle between the crystal vertical and lab horizontal is δ.

Since the same peak in reciprocal space is being observed, it can be assumed that the Bragg's condition is identically satisfied at both x positions; that is, $\chi_1 = \chi_2$ in Fig. 3.2 for all positions on the surface when observing a single peak in reciprocal space. The relation between Bragg peaks can be expressed as the angle, β, between the scan positions relative to the center of the R_C

$$\beta = \omega_1 - \omega_2 \tag{2}$$

The assumption is then made that the arc length, $\gamma = R\beta$ is equal to the horizontal shift of the sample stage. This assumption holds true as long as the deviation of the arc from the chord defined by Δx, σ_r, is negligible. Mathematically, this condition would be satisfied if $\Delta x >> \sigma_r$ or $\Delta x << R$. Both are reasonable assumptions considering that radii of curvature are generally on the order of 10 m – 1000 m while translations are on the order of 5 mm. This makes the following

$$\gamma = R\beta = R(\omega_1 - \omega_2) = \Delta x \tag{3}$$

Our initial analysis of this system for a convex system was done with the lab frame using the same Cartesian unit vectors as the R_C frame. However, upon shifting to a concave derivation, the R_C frame had to be rotated about the y-axis to maintain a positive

R vector. This shift changes the sign on the Δx term as the x-axis unit vector rotates about the y-axis. This can now be simplified to

$$R = \frac{-\Delta x}{\omega_1 - \omega_2} = \frac{x_2 - x_1}{\omega_2 - \omega_1} \tag{4}$$

as previously described by Fewster *et al* (2000), and thus derived regardless of the radial frame of reference used.

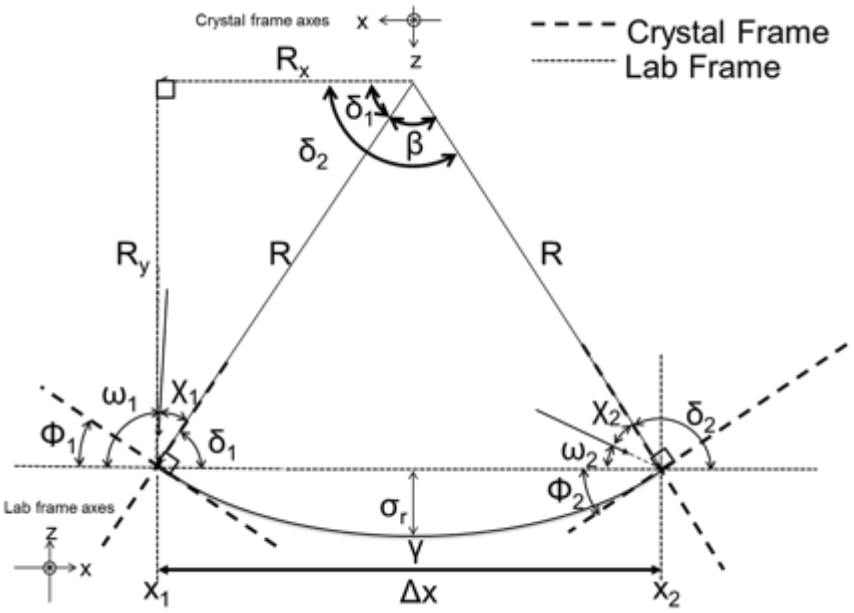

Fig. 3.2 Geometric model of curved substrate surface showing relations between beam angle and real space dimensions using the crystal and lab frame.

The radii of curvature of the bulk GaN crystals further indicate that the substrates were bowed concave up as shown in Fig. 3.3. With the substrate bowed concave up, the incident beam would reach the Bragg condition at reduced angles as it traversed the curved surface. This would, in turn, result in a Bragg peak at a smaller ω for one-

dimensional translations where $\Delta x > 0$, hence a negative slope in Equation 13 is realized. For simplicity, the R_C was represented as an absolute value.

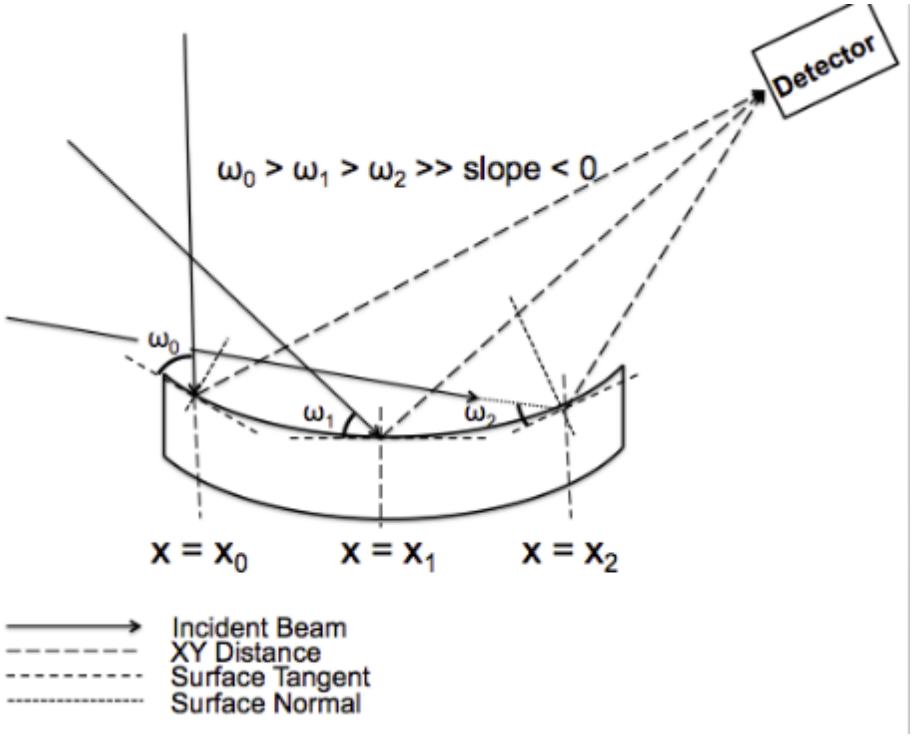

Fig. 3.3 GaN bowed concave with negative radius of curvature

3.2 Origin of Curvature in Bulk GaN

Despite the high quality of HVPE materials, the freestanding substrates have significant curvature. The curvature present in freestanding GaN is caused by internal stresses from within the substrate. The stresses undergo a change in sign and change from the bottom to the top of the substrate, where they change from compressive to tensile stress. In this section we will discuss some background information pertaining to curvature and bow in bulk structures and derive an expression for the theoretical

curvature of a bulk structure. We will then use this information to explain the origin of the curvature present in bulk GaN.

3.2.1 Background: Substrate Curvature and Bow

Fig. 3.4a illustrates an example of a single crystal substrate with no bow or curvature. This is an example of stress/strain-free material. However, such substrates can also exhibit bowing due to the effects of substrate treatment, as shown in Fig. 3.4b. Fig. 3.4c is an example of a substrate with curvature due to the change in stress state from compressive to tensile in the material. In this case, the curvature causes the substrate to bow. Such crystals can also be cut from the boule to be flat (without bow), but crystal planes remain curved from the stress gradient, as shown in Fig. 3.4d.

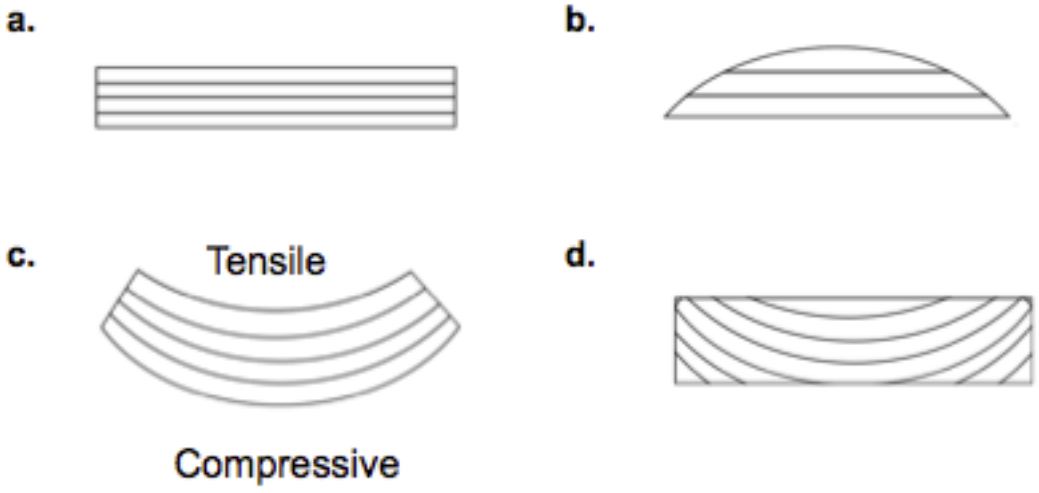

Fig. 3.4 Example of Bow and Curvature in a Substrate **(a)** Flat substrate with no curvature of the crystal planes **(b)** Bowed substrate surface with no crystal plane curvature **(c)** Bowed substrate with crystal plane curvature **(d)** Flat surface with crystal plane curvature

Radius of curvature measurements via x-ray diffraction are a true measure of the crystal strain as opposed to optical techniques (such as a multi-beam optical stress sensor) that use an array of parallel incident laser beams to reflect off the substrate surface and are collected by a detector. The latter method is heavily influenced by the substrate thickness and surface treatment, rather than actual crystal lattice elastic strain. For example, Fig. 3.4c and 3.4d have the same curvature, but only 3.4c is bowed. Therefore, to accurately measure the R_C of a substrate, regardless of which bowing state is present, XRD is the preferred method.

3.2.2 Derivation of Curvature in Bulk Structure

To accurately analyze the curvature of a bulk crystal substrate, a multi-layered structure model is used as shown in Fig. 3.5a. The total thickness H is divided into N layers with arbitrary thickness h_i. The reference length, L, included a fixed number of lattice parameters (with lattice constant, a_{ref}) with no elastic strain, stresses, or bending. The layers are then separated as shown in Fig. 3.5b, such that they are unconstrained and each layer undergoes a lattice transformation, expanding or contracting with respect to its respective reference length. The number of lattice parameters within L remain the same, introducing transformation strain ε^*_i, also known as stress free (eigen) strain [18], expressed as

$$\varepsilon_i^* = \frac{a_i - a_{ref}}{a_{ref}}, \; i = 1...N \tag{5}$$

where a_i is the lattice parameter after undergoing the lattice transformation.

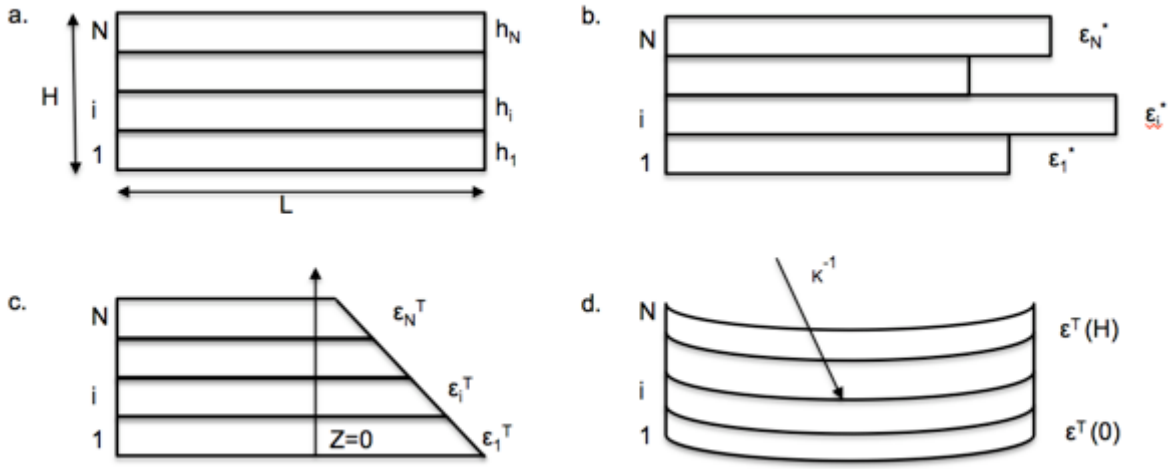

Fig. 3.5 Progression of Curvature in Bulk Multi-Layered Structure **(a)** A multi-layered structure of bulk thickness H, divided into N layers **(b)** Unconstrained layers undergoing lattice transformation **(c)** Compatible deformation of the coherent layers structure with respective coordinates **(d)** Elastic bending accompanies non-uniform elastic strain in the multilayered structure

Coherent layers deform in a compatible manner, meaning a 1:1 correspondence between the lattices at the interface of contacting layers such that during the lattice transformation, the lattice maintains continuity across the interface. The lateral strains in the layers will have a z-dependence, with the coordinate origin at the bottom of the first layer. The compatible deformation of the multilayer structure with the respective coordinates is shown in Fig. 3.5c, and the required conditions of the compatibility of total strain ε^T is shown as [19]

$$\frac{\partial^2 \varepsilon^T(z)}{\partial z^2} = 0 \tag{6}$$

The general expression for total strain can then be expressed as

$$\varepsilon^T(z) = A + Bz \tag{7}$$

where A and B are unknown coefficients used to derive an expression for curvature. Given that each layer is subjected to a different magnitude of self-strain, the compatible total deformation mentioned above, ε^T, is maintained by the layer's elastic strain layers, ε_i, written as:

$$\varepsilon_i = \varepsilon^T - \varepsilon_i^* \tag{8}$$

The elastic strain in the i^{th} layer will have a z-dependence as the compatible total deformation and self-strain have a z-dependence, therefore ε_i can be rewritten as

$$\varepsilon_i(z) = A - \varepsilon_i^*(z) + Bz \tag{9}$$

The elastic bending shown in Fig. 3.5d accompanies non-uniform elastic strain. The inherent strain in the individual layers of the structure causes the multilayered structure's curvature, thus to develop an expression for curvature, an analysis of the stress state is required. The z-dependent elastic strain is related to mechanical stress by assuming Hooke's Law and plane stress state in layers as shown:

$$\sigma_i(z) = M_i(z)\varepsilon_i(z), \quad i = 1...N \tag{10}$$

where $\sigma_i(z)$ and $M_i(z)$ are the z-dependent mechanical stress and the biaxial elastic modulus of the i^{th} layer, respectively. The two unknown coefficients, A and B, can then be determined by using mechanical equilibrium conditions for force and bending moment to yield:

$$A = \frac{J_1 I_1 - J_0 I_2}{I_0 I_2 - I_1^2}$$
$$B = \frac{J_0 I_1 - J_1 I_0}{I_0 I_2 - I_1^2} \tag{11a,b}$$

where I_k and J_k are defined as:

$$I_k = \int_0^H z^k M_i(z)dz, \qquad k = 0,1,2$$
$$J_l = \int_0^H z^l M_i(z)\varepsilon_i^*(z)dz, \qquad l = 0,1 \tag{12a,b}$$

This is done in order to simplify the expressions for the coefficients. Assuming the self-strain and biaxial moduli are known for the system, the curvature κ can be found using the relation:

$$\kappa = \frac{\varepsilon^T(H) - \varepsilon^T(0)}{H} \tag{13}$$

which reduces to:

$$\kappa = -B \tag{14}$$

The approach described above is consistent with results presented in [20-22].

3.2.3 Inclined Threading Dislocations and Stress Gradients in III-Nitride Structures

We attribute the compressive to tensile stress gradient in freestanding GaN to curvature caused by threading dislocations [23] and their inclination within the material. Cantu *et al* (2003) reported relaxation of compressively strained Si-doped (0001) $Al_{0.49}Ga_{0.51}N$ deposited on $Al_{0.62}Ga_{0.38}N$, where TEM discovered threading dislocations with initial [0001] lines directions in $Al_{0.62}Ga_{0.38}N$ inclining toward the $\langle 1\bar{1}00 \rangle$ directions within Si doped $Al_{0.49}Ga_{0.51}N$ [24].

These threading dislocations have an effective misfit dislocation component that generates stress, which may be in the same sense or different sense to other stresses in the layer. Furthermore, a model describing the conditions for dislocation inclination and relaxation due to "effective climb" of edge dislocations by Romanov *et al* (2003) [25] explains the mechanism behind the relaxation of compressive stresses in $Al_xGa_{1-x}N$.

Further growth with "frozen-in" inclined dislocations is shown to generate a tensile strain gradient as demonstrated by Cantu *et al* (2005) [26], which is responsible for cracking at a critical thickness [27]. Accord *et al* (2008) and Manning *et al* (2009) further demonstrated in situ growth wafer curvature measurements revealing compression to tension stress transition in compressed $Al_xGa_{1-x}N$. [28, 29]

The mechanism by which stresses relax/generate and form gradients are related to the inclination of the TD with respect to their original direction. The most common method of observed relaxation in lattice-mismatched semiconductor heterostructures is misfit dislocation (MD) formation at the interfaces, perpetuated by dislocation glide. This gliding process can proceed by bending the pre-existing threading dislocations or by generation of new dislocations. There is, however, a glide-free mechanism of elastic stress relaxation related to the inclination of the TD with respect to their original direction and their effective climb as shown in Romanov *et al* (2003), where the total biaxial far-field plastic relaxation at the top layer surface resulting from the triangular MD grid ε^1_{pl} is given by:

$$\varepsilon_{pl}^{top} = \frac{3}{2}\varepsilon_{pl}^{1} = \frac{3}{2} b \rho_{TD} L \tag{15}$$

where b is the Burgers vector, ρ_{TD} is threading dislocation density, and L is the projected length directly related to the layer thickness h and the inclination angle α, such that $L=h$ tan(α). The inclination angle, α, is formed when the straight dislocation originating from the substrate bends at the substrate/layer interface and becomes an angular dislocation as shown in Fig. 3.6. The lines of these dislocations are inclined with respect to the [0001]

growth direction, with α as large as 20°. The TD incline towards the $<1\bar{1}00>$ direction. From this, the average plastic relaxation for a layer is then:

$$\bar{\varepsilon}_{pl} = \frac{1}{4} b \rho_{TD} h \tan(\alpha) \tag{12}$$

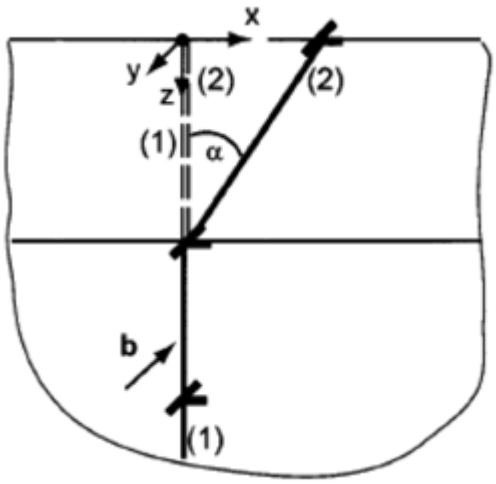

Fig. 3.6 Schematic of TD inclination forming at the interface between two layers. A Straight dislocation (1) bending at the interface by inclination angle, α, to form an angular dislocation (2).

3.3 The Role of Threading Dislocation Inclination in Curvature of Bulk GaN Substrates

In the previous section it was made clear that the origin of curvature in bulk GaN substrates is from the compressive tensile stress gradient by the inclination of threading dislocations within the material. In order to further understand the role of TD inclination and how it affects the curvature in bulk GaN we will derive a theoretical model, which shows the relation between curvature, dislocation density and threading dislocation inclination angle in free standing GaN. Following that we will verify the derived model with a well known standard in the literature and then apply it to our HVPE GaN substrates of interest, after determining their respective dislocation densities.

3.3.1 Theoretical Model

The curvature of a bulk multi-layered structure was derived to be equal to the unknown coefficient B in Eq. 14, which takes into account the thickness dependence of the self strain ε^*_i (z), defined as the lattice transformation that each layer undergoes as it expands or contracts with respect to its reference length. The self strain subjected to each layer of the structure is equivalent to the average plastic relaxation resulting form the glide free mechanism of stress relaxation related to the inclination of TD from Romanov et al (2003), as shown:

$$\varepsilon_i^*(z) = \bar{\varepsilon}_{pl} = \frac{1}{4} b \rho_{TD} h \tan(\alpha) \tag{13}$$

Equation 13 can then be used to solve for the unknown coefficient B, so that the curvature can be determined. This result derives an expression where curvature can be proportional to the TD inclination and TDD. This statement assumes the biaxial modulus no longer has z-dependence as ε^*_i is assumed to be the z-dependent plastic relaxation. After appropriate calculations are made, the curvature is

$$\kappa = \frac{1}{4} b \rho_{TD} \tan(\alpha) \tag{14}$$

The thickness dependence is eliminated, and the curvature developed by the average plastic relaxation is directly related to the TDD and the average inclination angle of the TDs. Fig. 3.7 shows a three dimensional (3D) schematic for inclined TD in wafers grown in [0001] direction.

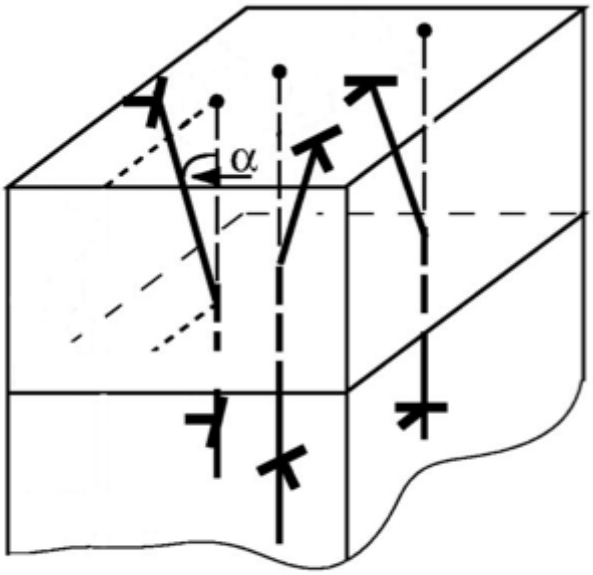

Fig. 3.7 3D schematic of inclined TDs in wafers grown in [0001] direction

Dwilinski *et al* reported on the growth of exceptionally high quality bulk GaN substrates using the ammonothermal method [30]. They reported TDD of ~5 x 10^3 cm^{-2}. Regardless of the crystal size, the R_C was reported to be greater than or equal to 1,000 m. Fig. 3.8 plots the derived model for varying inclination angles alongside the Ammonothermal bulk GaN crystal grown by Dwilinski *et al*. The substrate's radius of curvature supported the model, with an estimated inclination angle of ~15°.

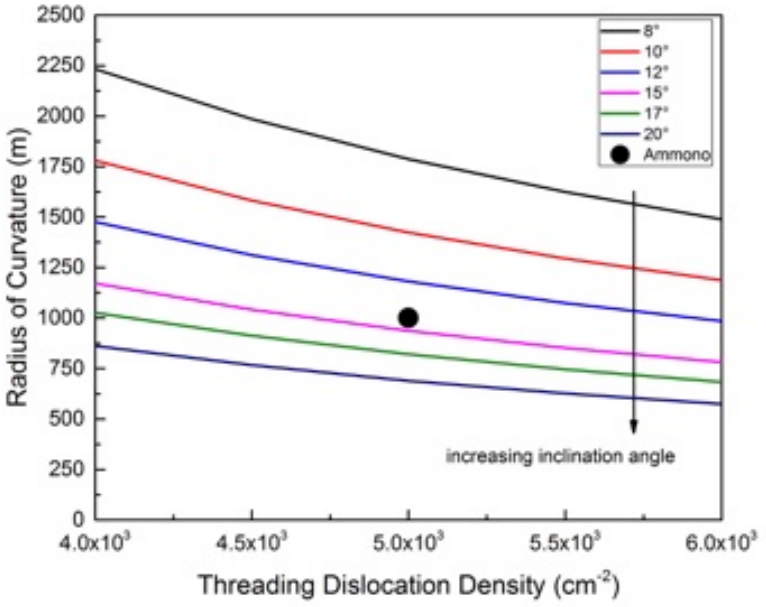

Fig. 3.8 The Ammono crystal is in agreement with the theoretical model with an estimated inclination angle of ~15°.

3.3.2 Determination of Dislocation Density in Bulk GaN Substrates

Panchromatic cathodoluminescence (CL) images for the commercial bulk GaN crystals along with the experimentally determined TDD are displayed in Fig. 3.9 and Table 3.2, respectively. The CL images show predominantly bright areas corresponding to band gap luminescence from defect free GaN as well as dark spots corresponding to non-radiative regions around defects that have been shown to be associated with threading dislocations, as in Rosner *et al* (1997). The CL images show a fairly uniform concentration of TDs along the region of the imaged surface, independent of length scale, while the corresponding SEM images of the bulk crystals all exhibited planar smooth surfaces (not shown).

Substrate A, shown in Fig. 3.9a, had lowest number of TD per scanned area, with a TDD of 4.16 x 10^5 cm^{-2}. Substrate B shown in Fig. 3.9b had a TDD of 1.35 x 10^6 cm^{-2}, with a low standard error compared to the rest of the sample set. The TDs in the substrate B are distributed in small groups or clusters. Substrate C shown in Fig. 3.9c had a TDD of 1.26 x 10^6 cm^{-2}, however this value is associated with a larger standard error, due to large variations in the distribution of dislocations at larger scales (not shown). Substrate D shown in Fig. 3.9d had the highest density of threading dislocations, at 2.92 x 10^6 cm^{-2}.

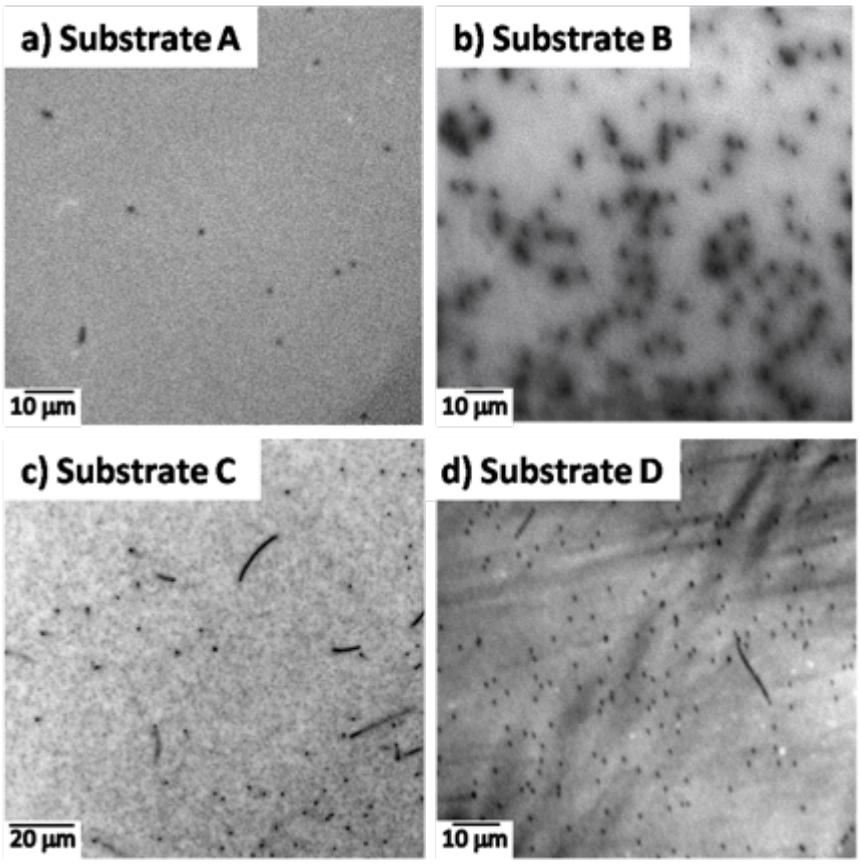

Fig. 3.9 Panchromatic CL images for the commercial bulk GaN vendors. Note the varying length scale. **(a)** Substrate A; **(b)** Substrate B; **(c)** The Substrate C; **(d)** Substrate D.

Table 3.2 Threading Dislocation Density Recorded Experimentally via Cathodoluminescence Imaging for the Commercial Bulk GaN Crystal Substrates

Substrate Designation	**Threading Dislocation Density (cm^{-2})**	**Standard Error (cm^{-2})**
A	4.16×10^5	1.14×10^5
B	1.35×10^6	3.67×10^4
C	1.26×10^6	6.05×10^5
D	2.92×10^6	2.09×10^5

3.3.3 Applying Theoretical Model to Bulk GaN Substrates

Fig. 3.10 shows the dependence of R_C with respect to TDD for the GaN substrates investigated. The experimental R_C and TDD values are plotted alongside the derived theoretical model over varying inclination angles. All of the commercial bulk GaN crystals investigated correlated well with the theoretical relations derived, supporting the proposed model relating the curvature from stress gradients to TDD and TDI.

According to the derived theoretical relation, substrate A had a TDI angle of 20°, with minimal deviation in both the R_C and TDD. Substrate B had an inclination angle of 10°. The standard error was negligible for the R_C and TDD. Substrate C was speculated to have a ~ 10° inclination angle, but the standard error is significant along the TDD, therefore it could have an inclination ranging from 10-17°. Substrate D is speculated to have an inclination angle between 8-10°. From here we can conclude that the theoretical model holds for bulk GaN crystals of large and small TDD and R_C.

The ranges of inclination angles (8°-20°) chosen for this study are based of the observed and measured inclination angles from previous studies [31,32]. TEM studies

done by Cantu *et al* (2003) reported a TDD of ~3 x 10^{10} cm^{-2}, where the TD where inclined by 10°-25° in the $\langle 1\bar{1}00 \rangle$ direction and had a misfit component, thus relieving misfit strain. Follstaedt et al's (2005) observations for compressively strained AlGaN indicated that TD inclination occurred prior to the introduction of Si, where the average inclination angle was ~19°, and the TDD is ~ 6.9 x $10^{9}cm^{-2}$. Follstaedt et al (2009) further examined AlGaN films with increasing Ga content, reporting TD inclination angles ranging from 6.7° to 17.8° and TDD of 6-7 x10^{9} cm^{-2}.

At the TDD observed in this report for HVPE bulk GaN (10^{5}-10^{6} cm^{-2}), it is difficult to measure TDI via cross-sectional TEM, as the TDD is too low. Another method to measure the TDI is via x-ray topography, however the TDD observed is too high for this technique. TD can be observed at this density when using Electron Channeling Contrast Imaging as performed by Picard et al (2009) and Carnevale et al (2015) [33, 34].

The average radius of curvature for the commercial HVPE grown GaN substrates is approximately ~ 5 m, leading to a large disparity in vicinality from edge to edge over the substrate (e.g., ~0.6° for R_C = 5 m for a 50 mm substrate). For comparison, the vicinality of GaN on sapphire is optimized for ~0.2° miscut in the m-direction of GaN which corresponds to 0.2° towards a-direction sapphire.

Therefore, even for GaN substrates suitable for LD and LEDs (TDD ~ 10^{4} cm^{-2} to 10^{6} cm^{-2}), there still exists a large non-negligible curvature. From this one can see the importance of lowering the TDD in the future so as to achieve the flattest, least bowed substrates possible, and avoid the detrimental effects to carrier transport and emission properties TD have in semiconductor heterostructures as demonstrated by Rosner *et al*.

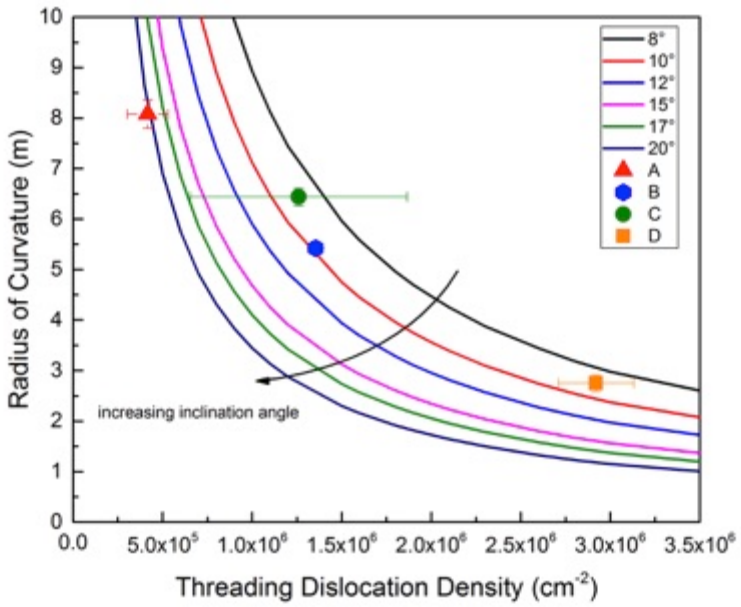

Fig. 3.10 The R_C with respect to the TDD for a range of TDI for the commercial Bulk GaN substrates plotted alongside the derived theoretical model

3.4 Conclusions

GaN templates on sapphire are compared alongside HVPE bulk c-plane GaN substrates. The curvature is surprisingly greater in the lower TDD bulk substrates than in the higher TDD GaN templates. The radius of curvature and threading dislocation density for commercially available freestanding GaN substrates were measured. Substrates with higher threading dislocation densities have smaller radii of curvature. Furthermore, a model was derived to investigate the dislocation inclination in GaN substrates and its dependence to TDD and R_C. The model was developed assuming that the curvature is caused by internal stresses within the substrate that undergo a change from compressive to tensile stress from the bottom to the top of the substrate. The experimentally determined R_C and TDD for substrates with uniform distribution of TDD confirm and support the derived theoretical model.

References

[1] S. Pimputkar, S.Kawabata , J.S.Speck , S.Nakamura, J. of Cryst. Growth, **403**, 7 (2014)

[2] J.S. Speck, S.J. Rosner, Physica B **273**, 24 (1999)

[3] S.J. Rosner, E. C. Carr, M. J. Ludowise, G. Girolami, and H. I. Erikson, Appl. Phys. Lett. **70**, 420 (1997),

[4] C. Youtsey, L.T. Romano, I. Adesida, Appl. Phys. Lett. **73**, 797 (1998).

[5] C. Youtsey, Romano, L.T. Molnar, R.J., Adesida, I, Appl. Phys. Lett. **74** 3537 (1999)

[6] J. Elsner, R. Jones, M.I. Heggie P.K. Snitch, M. Haugk, T. Frauenheim, S. Oberg, P.R. Briddon, Phys. Rev. B. **58** 12571 (1998).

[7] E.C. Kyle, S.W. Kaun , P.G. Burke, F.Wu, Y.R. Wu, YR ; J.S. Speck, J. Appl. Phys., **115**, 193702 (2014)

[8] Y.Mori, M.Imade, K.Murakami, H.Takazawa, H.Imabayashi, Y.Todoroki, K.Kitamoto, M.Maruyama, M.Yoshimura, Y.Kitaoka, T.Sasaki, J. of Cryst. Growth **350**, 72 (2012)

[9] R.T. Dwiliński, R.M. Doradziński, J. Garczyński, L.P. Sierzputowski, R. Kucharski, M. Zając, M. Rudzinski, R. Kudrawiec, W. Strupinski, J. Misiewicz, phys. status solidi, **1489**, 1489 (2011)

[10] E.R. Letts, T. Hashimoto, M. Ikari, Y. Nojima, J. of Cryst. Growth, **350**, 66 (2012)

[11] D. Tomida, Y. Kagamitani, Q. Bao, K. Hazu, H. Sawayama, S.F. Chichibu, C. Yokoyama, T. Fukuda, T. Ishiguro, J. of Cryst. Growth, **353**, 59 (2012),

[12] M. Saito, H. Yamada, K. Iso, H. Sato, H. Hirasawa, D.S. Kamber, T. Hashimoto, S.P. DenBaars, J.S. Speck, S. Nakamura, Appl. Phys. Lett., **94**, 052109 (2009)

[13] M.J. Callahan, B. Wang, K.D. Rakes, L.O.Bouthilette, S.Q. Wang, D.F. Bliss, J.W. Kolis, J. of Cryst. Growth, **287**, 376 (2006)

[14] M. Imanishi, Y. Todoroki, K. Murakami, D. Matsuo, H. Imabayashi, H. Takazawa, M. Maruyama, M. Imade, M. Yoshimura, Y. Mori, J. of Cryst. Growth **427,** 87 (2015)

[15] K. Fujito, S. Kubo, and I. Fujimura, Development of Bulk GaN Crystals and Nonpolar/Semipolar Substrates by HVPE, MRS BULLETIN, **34**, 313 (2009)

[16] S. Nakamura, , Japanese J. of Appl. Phys. **30**, 1705 (1991)

[17] P. Fewster, X-Ray Scattering From Semiconductors, Imperial College Press, (2000)

[18] T. Mura, Micromechanics of defects in Solids, 2nd Edition, 587 (1987)

[19] G.G. Stoney, Proceedings of the Royal Society (London) Ser A **82***,* 172 (1909)

[20] L.B. Freund and S. Suresh, Thin Film Materials, Cambridge University Press (2003)

[21] L.B. Freund, J. of Cryst. Growth, **132**, 341 (1993)

[22] L.B. Freund, J. of the Mechanics and Physics of Solids **44**, 723 (1996)

[23] A. Krost, A. Dadgar, G. Strassburger, and R. Clos, Phys. Status Solidi **200**, 26 (2003).

[24] P. Cantu, F. Wu, P. Waltereit, S. Keller, A. E. Romanov, U. K. Mishra, S.P. DenBaars, and J. S. Speck, Appl. Phys. Lett. **83**, 674 (2003).

[25] A. E. Romanov, J. S. Speck, Appl. Phys. Lett., **83**, 2569 (2003)

[26] P. Cantu, F. Wu, P. Waltereit, S. Keller, A. E. Romanov, S. P. DenBaars, and J. S. Speck, J. of Appl. Phys. **97**, 103534 (2005)

[27] A. E. Romanov, G. E. Beltz, P. Cantu, F. Wu, S. Keller, S. P. DenBaars,

and J. S. Speck, Appl. Phys. Lett. **89**, 161922 (2006)

[28] J.D. Acord, I.C. Manning, X. Weng, D.W. Snyder, J.M. Redwing, Appl. Phys. Lett. **93**, 111910 (2008)

[29] I. C. Manning, X. Weng, J. D. Acord, M. A. Fanton, D. W. Snyder, and J. M. Redwing, J. of Appl. Phys., **106**, 023506 (2009)

[30] R. Dwilinski, R. Doradzinski, J. Garczynski, L.P. Sierzputowski, A. Puchalski, Y. Kanbara, K. Yagi, H. Minakuchi, H. Hayashi, J. of Cryst. Growth, **310**, 3911 (2008)

[31] D. M. Follstaedt, S. R. Lee, P. P. Provencio, A. A. Allerman, J. A. Floro, and M. H. Crawford, Appl. Phys. Lett., **87**, 121112 (2005)

[32] D. M. Follstaedt, S. R. Lee, A. A. Allerman, and J. A. Floro, , J. of Appl. Phys. **105**, 083507 (2009)

[33] Y.N. Picard, M.E. Twigg, J.D. Caldwell, C.R. Eddy Jr., M.A. Mastro and R.T. Holm, Scripta Materialia **61**, 773 (2009)

[34] S.D. Carnevale, J.I. Deitz, J.A. Carlin, Y.N. Picard, D.W. McComb, M. De Graef, S. A. Ringel, and T.J. Grassman, "IEEE J. of Photovoltaics, **5**, 676 (2015)

Chapter 4: Verifying Vegard's Law for $In_xAl_{1-x}N$/GaN

In the previous chapter, we compared the radius of curvature between GaN templates and bulk GaN substrates and found the templates to have less crystallographic curvature. This makes the GaN template the more ideal choice, as we want to see the effects of curvature due to changing the indium composition in the thin film, and avoid any additional curvature from the substrate/template if possible. Furthermore, we thoroughly examined the origin of the curvature in bulk GaN and attributed it to stress gradients within the material arising from threading dislocation inclination.

In this chapter we will move forward with the verification of Vegard's Law for $In_xAl_{1-x}N$ on GaN templates. Ex-*situ* radius of curvature measurements using XRD was performed on the GaN templates and $In_xAl_{1-x}N$ layers to analyze the curvature before and after the $In_xAl_{1-x}N$ deposition. The relaxed a_0- and c_0- lattice parameters of $In_xAl_{1-x}N$ were determined from a combination of the XRD results and linear elasticity for coherent films and compared alongside Vegard's Law to see if they are in agreement with one another.

4.1 $In_xAl_{1-x}N$/GaN Template Growth and Curvature Analysis

The MOCVD growth was performed in a Veeco P-75 Turbodisc reactor. All growths were performed on flat (0001) sapphire substrates. The precursor used for the GaN template was trimethylgallium and ammonia. The precursors for $In_xAl_{1-x}N$ were trimethylindium, trimethylaluminum, and NH_3. The GaN templates were grown as described by Nakamura *et al* (1991) [1], with a total thickness of approximately 2.73 μm.

Because of the lack of *in situ* monitoring, following the deposition of the GaN template, the sample was removed from the growth chamber and taken to the XRD laboratory for the ex-situ R_C measurement as described previously. The measurement entails taking on-axis (0002) ω-scans, then translating the sample and measuring the displacement of the ω peak positions [2]. The results are shown in Table 4.1. Five templates were grown for this study labeled A through E. The radius of curvature ranged from 10.281 m to 10.990 m with an average value of 10.57 m. Note the relatively small variation in R_C compared to the different HVPE GaN substrates. Following this measurement the samples are brought back to the growth chamber for the $In_xAl_{1-x}N$ regrowth.

Table 4.1 Radius of Curvature of the GaN Templates

GaN Template	**Radius of Curvature (m)**
A	10.281
B	10.463
C	10.990
D	10.218
E	10.922

Prior to $In_xAl_{1-x}N$ deposition, a ~220 nm GaN buffer layer was regrown over the GaN template. In semiconductor growth, a homoepitaxial buffer layer is deposited to bury impurities that can impact the layer quality of subsequent layers. The GaN buffer

layer was grown under the same conditions as the GaN template. A control sample consisting of just the GaN buffer layer over GaN template A was grown to compare in addition to the $In_xAl_{1-x}N$ films.

The $In_xAl_{1-x}N$ films were deposited over the GaN buffer layer during the same run on GaN templates B through E. The approximate indium composition (verified with atom probe tomography) and thickness were measured as discussed in Chapter 2 using $\omega - 2\theta$ scans for the (0002) reflection from a Panalytical X'Pert Materials Research Diffractometer (MRD) in triple axis geometry. RSMs for the $(10\bar{1}5)$ reflection were measured to determine the coherency of the film on the GaN template as discussed previously. Following these characterization steps, *ex-situ* R_C measurements were taken once again to look at how the radius of curvature changed following the deposition of $In_xAl_{1-x}N$ and the GaN buffer layer.

Table 4.2 displays the *ex-situ* R_C results for the GaN templates and the thin film, along with the In composition determined by HRXRD and APT. With the exception of the control sample, which consists of the just the GaN buffer layer, the thin films consist of the GaN buffer layer and $In_xAl_{1-x}N$. The R_C of the GaN templates varies from 10.218 m to 10.990 m. For all cases, the R_C decreased following deposition of the homo-epitaxial buffer layer and the $In_xAl_{1-x}N$ layer, indicating convex bending. The evolution of the sample structure is shown in Fig. 4.1 and shows the three structures of interest: the GaN template, the control sample and the full structure with $In_xAl_{1-x}N$.

Table 4.2: In composition and R_C of Films and Templates

GaN Template	R_C Template (m)	In % HRXRD	In % APT	R_C Film (m)
A	10.922	Control	N/A	9.817
B	10.281	15.32	15	9.826
C	10.463	19.35	19	9.383
D	10.99	23.31	N/A	9.500
E	10.218	27.65	28	8.128

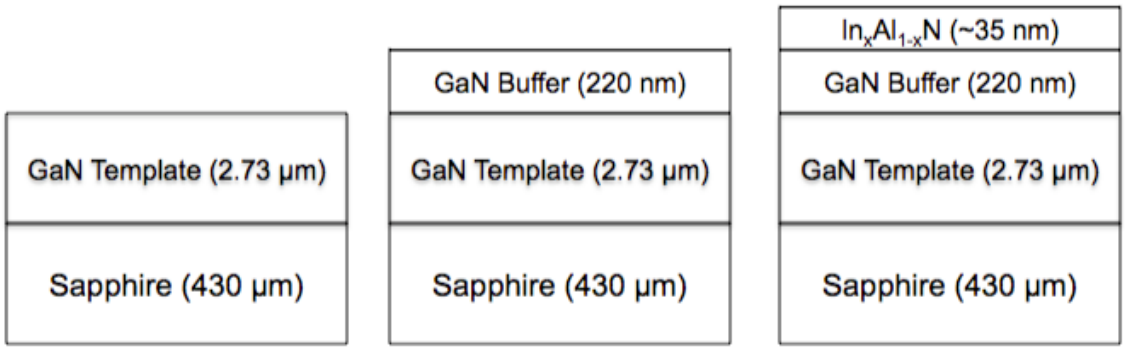

Fig 4.1 Evolution of sample Structure with the GaN template on Sapphire, the control sample consisting of just the GaN buffer on the GaN template, and finally the full structure with $In_xAl_{1-x}N$.

The deposition of the GaN template on sapphire produced a compressive mismatch stress, bending the structure convex as shown in Fig. 4.2a. At room temperature, GaN on sapphire is in a state of biaxial compressive stress due to the mismatch in the coefficient of thermal expansion (CTE) between sapphire (7.1×10^{-6} K^{-1}) and GaN (5.59×10^{-6} K^{-1}) [3,4]. Since the CTE of sapphire is greater than the CTE of GaN, the film is in compression after cooling from the MOCVD growth temperature.

The average R_C of the GaN templates was 10.57 m with a standard deviation of 0.36 m. After the ~220 nm GaN buffer layer was deposited on GaN template A for the control sample, the R_C decreased from 10.92 m to 9.817 m. The further reduction in R_C following the buffer layer deposition indicates that the structure underwent further convex bending as shown in Fig. 4.2b due to additional compressive mismatch stress introduced by the GaN buffer layer along with the initial compressive stress exhibited when just the GaN template was present.

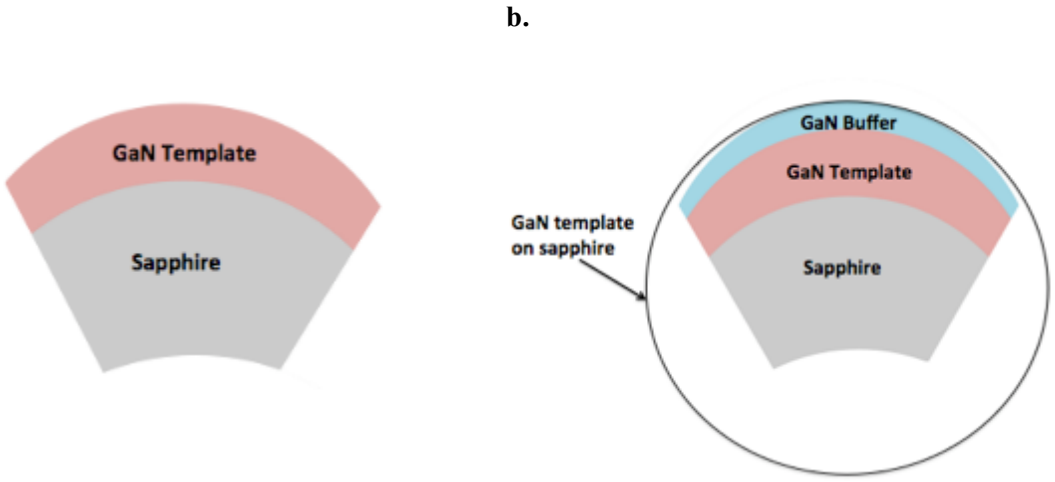

Fig. 4.2 History of curvature and bending in sample structures. **A.** GaN on Sapphire **B.** GaN Control

4.1.1Curvature and Stress State of GaN Buffer

Based off of the results in Table 4.2 it is hard to draw any concrete conclusions about what is going on following the deposition of $In_xAl_{1-x}N$ since no trends are immediately apparent. Since *in-situ* analysis of the R_C during MOCVD growth is not available in our MOCVD system, the change in the radius of curvature after the GaN

buffer layer growth on GaN templates B through E cannot be directly measured as $In_xAl_{1-x}N$ and the GaN buffer layer were deposited without interruption.

However, given that all GaN layers were grown under the same conditions, the 1.105 m R_C difference between GaN template A and the buffer layer in the control structure was applied to the GaN buffer layers deposited on GaN templates B through E. We can then demonstrate the corrected R_C after the GaN buffer layer growth on GaN templates B through E, as shown in Table 4.3.

Table 4.3: R_C of GaN Template & Corrected R_C after GaN Buffer Layer Deposition

GaN Template	**R_C Template (m)**	**Standard Error (m)**	**Corrected R_C (m)**
B	10.281	0.0769	9.176
C	10.463	0.103	9.358
D	10.99	0.0629	9.885
E	10.218	0.1759	9.113

The 1.105 m difference in R_C is mainly attributed to the increase in thickness, as the thickness of the buffer layer is ~8% of the thickness of the GaN template. However the change in curvature is also due to stress gradients in the GaN buffer layer caused by threading dislocation (TD) inclination. To determine the possible role of TD inclination in tensile stress generation at the growth temperature, the average total stress must be investigated. The average total stress in the film is equal to the sum of the stress component due to thermal expansion (σ_{TEC}) and the stress component due to threading dislocation (TD) inclination and any other growth stresses (likely due to early stage island coalescence in the GaN template [5], also known as the growth stress (σ_{GS}). The average total film stress is expressed as (σ^{avg}_f):

$$\sigma_f^{avg} = \sigma_{TEC} + \sigma_{GS} \qquad (1)$$

The σ_{TEC} can be calculated by using the tensor matrix for the hexagonal crystal structures [6]:

$$\sigma_{TEC} = (C_{11} + C_{12} - \frac{2C_{13}^2}{C_{33}})\varepsilon_{11}^{film} \quad (2)$$

where C_{11}, C_{12}, C_{13}, and C_{33} are elastic constants for GaN [7]. ε_{11}^{film} is the strain in the film, expressed as

$$\varepsilon_{11}^{film} = \int_{RT}^{GT} \alpha_{11} dT = \int_{RT}^{GT} (\alpha_{11}^{f} - \alpha_{11}^{s}) dT \qquad (3)$$

where α_{11}^{f} and α_{11}^{s} are the temperature dependent coefficients of thermal expansion for the film (GaN) and substrate (sapphire), respectively. GT and RT are the growth temperature (1080 °C) and room temperature (25 °C), respectively. α_{11}^{f} and α_{11}^{s} are polynomial expressions derived from temperature dependent thermal expansion data for GaN and sapphire [8-14]. After substituting all terms for their respective values, σ_{TEC} of the GaN on sapphire is -0.855 GPa. The negative sign indicates the film is in a state of compression.

σ^{avg}_{f} can also be expressed by Stoney's Formula, which takes into account a film under equi-biaxial stress [15-18]:

$$\sigma_f^{avg} = \frac{E_s h_s^2}{6(1-v)h_f R_C} \qquad (4)$$

where E_S, h_S are the elastic modulus and thickness of the substrate (sapphire), and h_f is the thickness of the film (GaN). R_C is the radius of curvature of the control structure measured via XRD and v is the poisson's ratio, $v = 0.30$, assuming equi-biaxial stress.

At h_{f1} = 2.73 μm (GaN template thickness), the template has a R_{C1} = 10.92 m. Using Eq. 4, σ_f is -0.672 GPa, corresponding to an elastic in-plane strain of -0.150%. After adding the ~220 nm GaN buffer layer, h_{f2} is equal to 2.95 μm and the R_{C2} is 9.81 m. At h_{f2}, σ_f is -0.692 GPa, corresponding to an elastic in-plane strain of -0.153%. One can note that the addition of this 220 nm layer introduces a negligible change in the compressive stress/strain.

If one rearranges Eq.1, such that

$$\sigma_{GS} = \sigma_f - \sigma_{TEC} \qquad (5)$$

the growth stress can be calculated in the GaN layer. At h_{f1}, σ_{GS1} = 0.183 GPa, which corresponds to an elastic in-plane strain of ~0.04%. At h_{f2}, σ_{GS2} = 0.163 GPa, which corresponds to an elastic in-plane strain of ~0.04%. There is negligible change in the tensile stress/strain following the GaN buffer deposition. Table 4.4 displays the average film stress and growth stress along with their respective in-plane strain at the two different thicknesses.

Table 4.4 Average Film Stress and Growth Stress for GaN Template before and after Buffer Layer Deposition

	GaN Template h_{f1} = 2.73 μm	GaN template + GaN buffer h_{f2} = 2.95 μm
σ_f	-0.672 GPa	-0.692 GPa
ε_f	-0.150 %	-0.153 %
σ_{GS}	0.183 GPa	0.163 GPa
ε_{GS}	0.04 %	0.04 %

Now that the growth stress is calculated, the inclination of TDs can be determined by solving for the stress gradient in the GaN buffer layer. As shown in the literature [19,20], the stress gradient in a layer can be expressed as:

$$\frac{d\sigma}{dz} = -M\kappa \qquad (6)$$

where M is the biaxial modulus and κ is curvature. Curvature can further be expressed as:

$$\kappa = \frac{1}{4} b\rho_{TD} \tan(\alpha) \qquad (7)$$

where b is the magnitude of the Burger's vector (for our case, we are concerned about pure edge TDs and b has the same magnitude as the a lattice constant of GaN), ρ_{TD} is the dislocation density, and α is the average inclination angle of the TDs. The stress gradient in the GaN buffer layer can be expressed as:

$$\Delta\sigma = -M * (\frac{1}{4} b\rho_{TD} \tan(\alpha)) * \Delta h \qquad (8)$$

where Δσ represents the difference in growth stress from h_1 to h_2, i.e. in the buffer layer, which is equal to $\Delta\sigma = \sigma_{GS@h_2} - \sigma_{GS@h_1} = 0.16314 - 0.1833 = -0.0203 GPa$. Δh is equal to the difference between h_1 to h_2, which is the thickness of the GaN buffer layer (~220 nm). ρ_{TD} is 8 x 10^8 cm^{-2}, which is typical for a GaN template on sapphire. The inclination angle for the GaN buffer layer is calculated to be 17.3°. The result presented here in is close agreement with Mathis *et al* (2001) [21], who reported an inclination angle of ~15.6° for GaN layers via modeling. We note that the stress change due to TD inclination, ~0.02 GPa is negligible compared to TEC mismatch stresses (~0.6-0.7 GPa).

4.1.2 $In_xAl_{1-x}N$

Fig. 4.3a plots the difference between the R_C of the film and template (ΔR_{Cf-t}), as a function of indium composition verified by XRD and APT along with the control sample, which is represented independent of indium composition. Fig. 4.3b plots the difference between the experimentally determined R_C of the film ($In_xAl_{1-x}N$) and the corrected R_C of the GaN buffer layers (ΔR_{Cf-c}) on GaN templates B through E as a function of indium composition verified by XRD and APT. Table 4.5 displays the ΔR_{Cf-c} along with the standard error for the R_C measurement by XRD of the $In_xAl_{1-x}N$ layer and GaN template. Fig. 4.4 plots the difference in the total average film stress between the $In_xAl_{1-x}N$ films and the GaN buffer layers on GaN templates B through E ($\Delta\sigma_{f-c}$). This calculation takes into account the corrected R_C for the GaN buffer layers deposited on GaN templates B through E.

a.

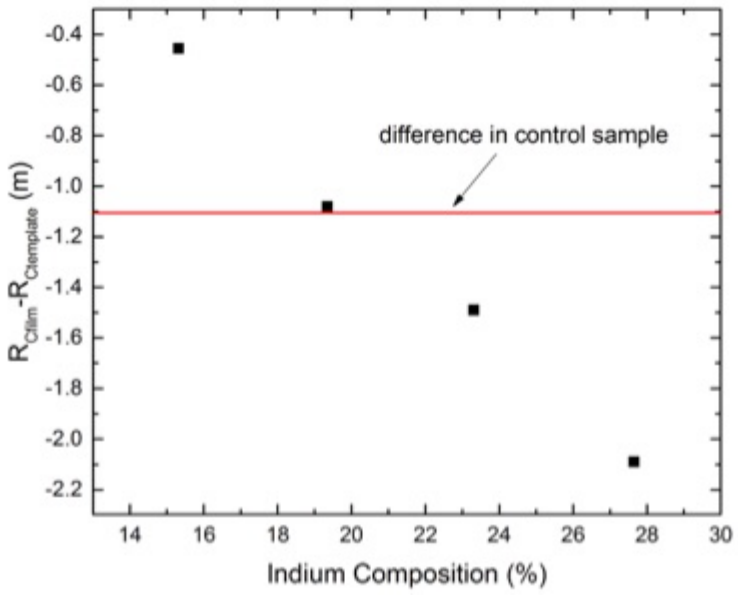

b.

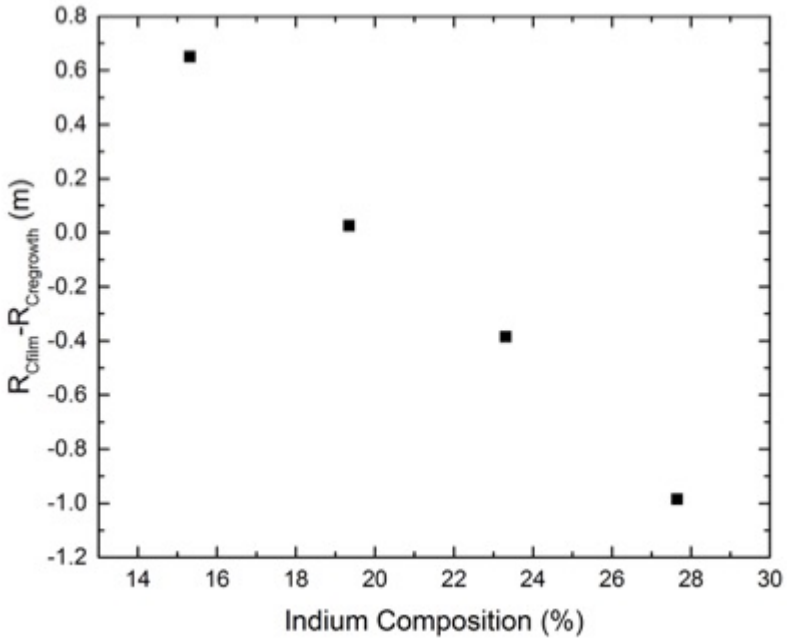

Fig. 4.3 a. R_C analysis of InAlN layers to GaN template along with control sample **b.** R_C Analysis of InAlN layers to GaN Buffer Layer

Table 4.5: Standard Error for R_C of GaN Template and R_C Film along with $\Delta R_{Cf\text{-}c}$

GaN Template	Standard Error R_C GaN Template (m)	In %	Standard Error of R_{Cf} (InAlN) (m)	$\Delta R_{Cf\text{-}c}$ (m)
A	0.089	Control	0.073	N/A
B	0.077	15.32	0.087	0.650
C	0.103	19.35	0.130	0.025
D	0.063	23.31	0.067	-0.385
E	0.176	27.65	0.039	-0.985

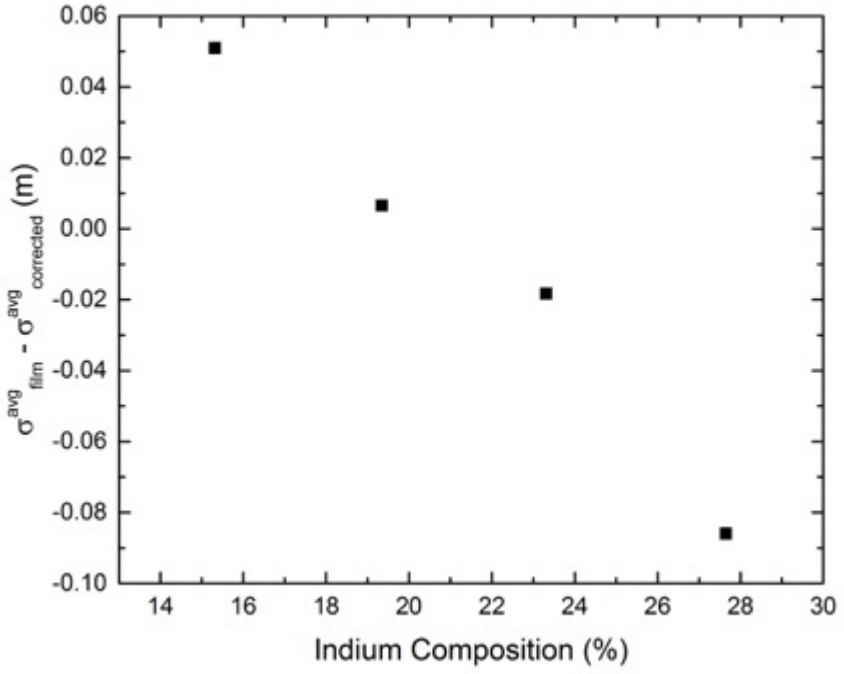

Fig. 4.4 Total average film stress between the InAlN and the GaN buffer layer

For the samples grown with higher compositions than the Vegard's Law lattice-matched 18% composition (23.31% In and 27.65% In), $\Delta R_{Cf\text{-}t}$ was -1.49 m and -2.09 m, respectively as shown in Fig. 4.3a, which is more negative than the control sample (-1.105 m). This indicates that following $In_xAl_{1-x}N$/GaN buffer layer deposition, the R_C decreases more than in the control sample, indicating further convex bending. Fig. 4.3b shows that at these indium compositions (23.31% In and 27.65% In) there is also a negative $\Delta R_{Cf\text{-}c}$. Table 4.5 then displays that $\Delta R_{Cf\text{-}c}$ is larger than the standard error for the R_C measurement of $In_xAl_{1-x}N$ and GaN template, indicating that the change in curvature following $In_xAl_{1-x}N$ deposition is statistically significant and causes convex bending. Fig. 4.4 shows that the $\Delta\sigma_{f\text{-}c}$ in these samples was negative, indicating a

compressive mismatch stress. It is clear from the information gathered that following $In_xAl_{1-x}N$ with $x > 0.18$ deposition, additional compressive stresses were introduced to cause further convex bending in addition to the original convex bending formed by compressive mismatch stresses from the GaN buffer layer and GaN template deposition. Increasing the indium composition of the deposited film past the lattice matched composition causes the structure to bow more convex with respect to the control sample as shown in Fig. 4.5a, due to additional compressive mismatch stresses. These results correlate well with Vegard's Law, as the a lattice constant of $In_xAl_{1-x}N$ with $x > 0.18$ is larger than that of GaN, causing the film to be strained in compression and bend more convex relative to the control sample.

For the sample grown near the lattice-matched composition (19.35% In), $\Delta R_{Cf\text{-}t}$ was -1.08 m. Fig. 4.3a clearly shows that this -1.108 m difference is comparable to the $\Delta R_{Cf\text{-}t}$ for the GaN control sample (-1.105 m). Given that $\Delta R_{Cf\text{-}t} = -1.105$ m for the control sample is primarily due to the added thickness of the GaN buffer layer, $\Delta R_{Cf\text{-}t} = -1.08$ m for $In_{0.19}Al_{0.81}N$ is almost entirely due to the added thickness of the GaN buffer and the $In_{0.19}Al_{0.81}N$ layer, as well as the CTE mismatch with sapphire, as previously discussed. Fig. 4.3b shows that $\Delta R_{Cf\text{-}c}$ is negligible and close to zero, stating that there is little change in the R_C after $In_{0.19}Al_{0.81}N$ deposition on the GaN buffer layer. Furthermore, Table 4.5 shows that the change in $\Delta R_{Cf\text{-}c}$ is less than the standard error for the R_C measurement of the $In_{0.19}Al_{0.81}N$ and GaN template, indicating that it is statistically insignificant. Fig. 4.4 shows that $\Delta\sigma_{f\text{-}c}$ was essentially zero, indicating no additional stress was added following $In_{0.19}Al_{0.81}N$ deposition. These results indicate that the $In_{0.19}Al_{0.81}N$ deposited over its respective GaN buffer layer had essentially no change in

R_C as shown in Fig. 4.5b, assuming the R_C mismatch between the GaN buffer layer (deposited before the $In_{0.19}Al_{0.81}N$) and GaN template are the same as the GaN control sample. Therefore $In_{0.19}Al_{0.81}N$ is in effect the most closely lattice-matched composition to GaN as minimal to no bending and change in R_C were observed when compared to the GaN control sample.

For the sample grown with In concentration below the lattice-matched composition (15.32%), $\Delta R_{Cf\text{-}t}$ = -0.455 m. In Fig. 4.3a, o $\Delta R_{Cf\text{-}t}$ for $In_{0.15}Al_{0.85}N$ is less negative than that of the control sample. This indicates that following $In_xAl_{1-x}N$/GaN buffer layer deposition, the R_C decreased less than in the control sample. Fig. 4.3b shows that this indium composition has a positive $\Delta R_{Cf\text{-}c}$, and Table 4.5 shows that $\Delta R_{Cf\text{-}c}$ is greater than the standard error for the R_C measurement of $In_xAl_{1-x}N$ and GaN template, indicating that the change in curvature following just $In_xAl_{1-x}N$ deposition is statistically significant. Fig. 4.4 shows that $\Delta\sigma_{f\text{-}c}$ was positive, indicating tensile mismatch stress between the $In_{0.15}Al_{0.85}N$ films and the buffer layer. This information gathered indicates that at this composition, though still bowing convex, the structures exhibited signs of concave bending, as shown in Fig. 4.5c. The structures began to exhibit tensile mismatch stress following $In_xAl_{1-x}N$ ($x < 0.18$) deposition, which competes with compressive mismatch stress originally present from the GaN buffer layer deposition on the GaN template, bending the structure in a convex manner. The competing mechanisms therefore reduce the mismatch. Depositing films with indium composition below the lattice matched composition lead to concave bending and tensile mismatch stress, however it was not directly observed due to the initial state of convex bending produced by the compressive mismatch stress from the GaN buffer layer and GaN template. This

correlates once again with Vegard's Law as $In_xAl_{1-x}N$'s (x <0.18) a-lattice constant is smaller than that of GaN, causing the film to be strained in tension and bend concave.

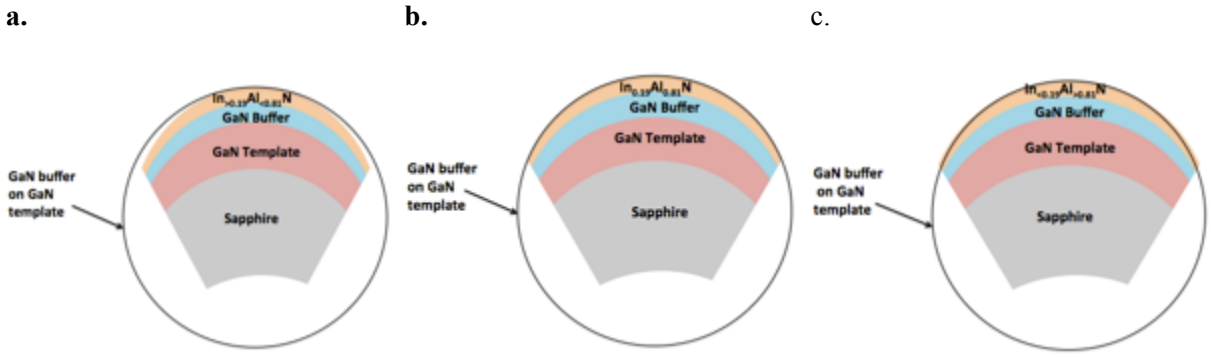

Fig. 4.5 History of curvature and bending in InAlN samples **A.** In Rich InAlN **B.** ~ lattice matched composition. **C.** Al- rich InAlN

4.2 Analysis of lattice parameters of $In_xAl_{1-x}N$

4.2.1 Coherent Lattice Parameters

The coherent lattice parameters of $In_xAl_{1-x}N$ to GaN are calculated first. The coherently strained c-lattice parameter of the $In_xAl_{1-x}N$ is determined using Bragg's law [22],

$$\lambda=2d\sin(\theta), \quad (9)$$

where λ is the wavelength of the x-ray source, CuKα = 1.5418 nm, and θ is the theta peak position of the $In_xAl_{1-x}N$ layer peak in the $\omega - 2\theta$ scan shown in Chapter 2 (Fig 2.2). The expression for d spacing in the hexagonal crystal structure is then used to related the d spacing to the c-lattice parameter,

$$\frac{1}{d^2} = \frac{4}{3}\frac{h^2 + hk + k^2}{a^2} + \frac{l^2}{c^2} \quad (10)$$

where d_{002} is used from Eq. 9. (hkl) is the orientation of interest used in the XRD scan (002) and a and c are the coherently strained lattice constants.

The coherently strained a-lattice parameter was determined from the RSM for the $(10\bar{1}5)$ reflection shown in Chapter 2 (Fig 2.3). For all compositions, the $In_xAl_{1-x}N$ peaks were coherently strained to the GaN peak, and therefore had the same a-lattice constant, 3.189 A. Table 4.6 displays the coherent lattice parameters for the $In_xAl_{1-x}N$ layer.

Table 4.6: Coherent Lattice Parameters for $In_xAl_{1-x}N$ on GaN

Indium Composition (%)	a (angstroms)	c (angstroms)
15	3.189	5.082
19	3.189	5.128
22	3.189	5.173
28	3.189	5.224

4.2.2 Relaxed Lattice Parameters

The relaxed a_0- and c_0- lattice parameters of $In_xAl_{1-x}N$ were determined from the using the coherent lattice parameters in Table 4.6 and the elastic constants of AlN and InN [23]. The relaxed a_0-lattice parameter of the $In_xAl_{1-x}N$ layers was calculated using,

$$a_0^L = \frac{\frac{c^L}{m} + 2(\frac{C_{13}}{C_{33}}) + a^L}{1 + 2(\frac{C_{13}}{C_{33}})} \quad (11)$$

where a_0^L is the relaxed lattice parameter of the film layer, c^L and a^L are the coherently strained c- and a- lattice parameters of the $In_xAl_{1-x}N$ layer, respectively, C_{33}

and C_{13} are elastic constants for the $In_xAl_{1-x}N$ layer, and *m* is the c/a ratio, which one can assume to be the same in the layer (L) or substrate (S); $m = m^L = m^S$ [24]. For the coherently strained layers, $a^L = a_0^S$. The elastic constants for the $In_xAl_{1-x}N$ layer were calculated using the elastic constants for AlN and InN and assuming Vegard's Law for the varying In compositions. They are displayed in Table 4.7 [23]. The relaxed c_0-lattice parameter (c_0^L) can be calculated using the relation for m, where $c_0^L = a_0^L m^L$. These experimentally derived relaxed lattice parameters agree closely with the lattice parameters derived from Vegard's law as shown in Fig. 4.6a and 4.6b [38,39]. This mechanical approach to verifying Vegard's Law for $In_xAl_{1-x}N$ differs from the results already existing in the literature, however verifies that pseudomorphic $In_xAl_{1-x}N$ obeys Vegard's Law for the lattice matched, Al rich, and In rich compositions.

Table 4.7: Elastic Constants for AlN, InN and $In_xAl_{1-x}N$ assuming Vegard's Law

	AlN	InN	$In_{0.15}Al_{0.85}N$	$In_{0.19}Al_{0.81}N$	$In_{0.23}Al_{0.77}N$	$In_{0.28}Al_{0.72}N$
C_{11} (GPa)	396	223	370	363	357	347
C_{12} (GPa)	137	115	133	132	132	130
C_{13} (GPa)	108	92	105	104	104	103
C_{33} (GPa)	373	224	350	344	340	331

a.

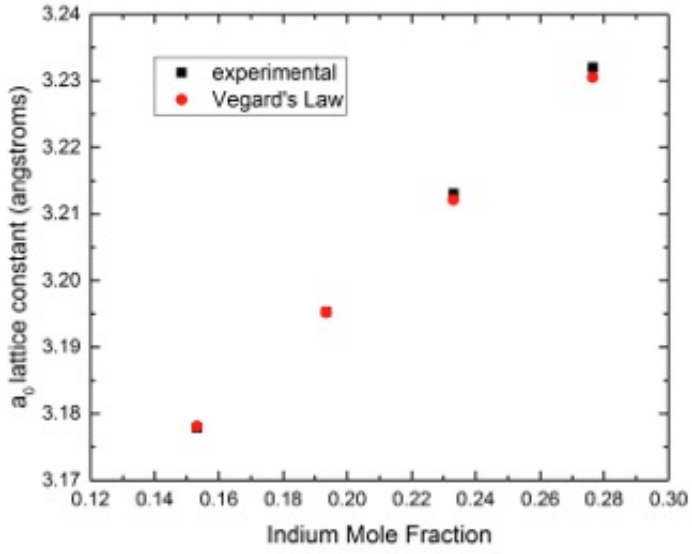

b.

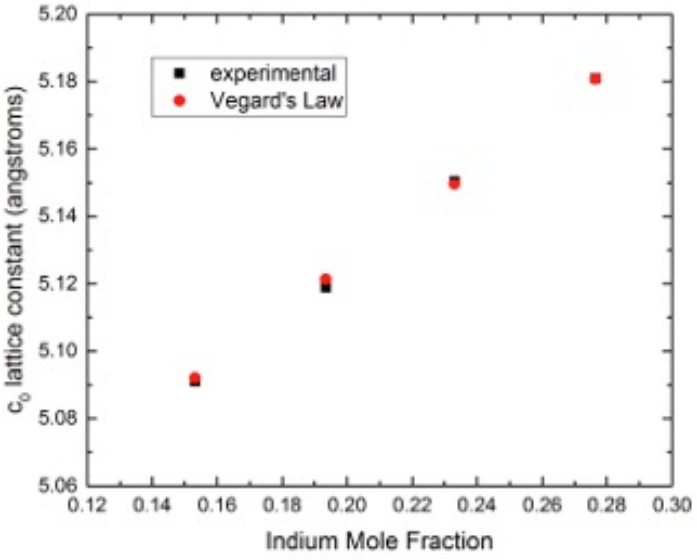

Fig. 4.6 a. Experimentally derived a_0-lattice parameter, indium mole fraction determined by XRD and APT **b.** Experimentally derived c_0-lattice parameter, indium mole fraction determined by XRD and APT

4.3 Conclusions

Ex-situ R_C measurements with ω-scans were performed after the GaN template deposition and after the $In_xAl_{1-x}N$ to investigate the strain state and verify the lattice-matched composition of $In_xAl_{1-x}N$ to GaN. Experiments analyzing the R_C between films ($In_xAl_{1-x}N$/GaN buffer layer for control sample) and GaN template confirm that Vegard's law holds and that ~$In_{0.18}Al_{0.82}N$ is lattice-matched to GaN. Furthermore, the relaxed a_0- and c_0- lattice parameters of $In_xAl_{1-x}N$ are experimentally determined and hold when compared alongside the theoretical lattice parameters derived from Vegard's law.

References

[1] S. Nakamura, Jap. J. of Appl. Phys. **30**, 1705 (1991)

[2] P. Fewster, X-Ray Scattering From Semiconductors, Imperial College Press, (2000)

[3] F. Brunner, V. Hoffmann, A. Knauer, E. Steimetz, T. Schenk, J.T. Zettler, M. Weyers, J. of Cryst. Growth **298**, 202 (2007)

[4] F. Brunner, A. Knauer, T. Schenk, M. Weyers, J.T. Zettler, J. of Cryst. Growth **310**, 2432 (2008)

[5] T. Boettcher, S. Einfeldt, S. Figge, R. Chierchia, H. Heinke, and D. Hommel, J. S. Speck, Appl. Phys. Lett. **78**, 14 (2001)

[6] J.F. Nye, Physical Prop. of Cryst., Oxford University Press, (1957)

[7] A. E. Romanov, E. C. Young, F. Wu, A. Tyagi, C. Gallinat, S. Nakamura, S.P. DenBaars, J.S. Speck, J. of Appl. Phys. **109**, 103522 (2011)

[8] G.K White, R.B. Roberts, High Temp. High Pressure. **15**, 321 (1983)

[9] E.R. Dobrovinskaya, L.A. Lytvynov, V. Pishchik, Sapphire: Material, Manufacturing, Applications, Springer Publishing, (2009)

[10] R.R. Reeber, K.Wang, J. of Mat. Research **15**, 40 (2000)

[11] R.R. Reeber, Phys. Status Solidi. **321**, 321 (1975)

[12] E. Gruneisen, Handbuch der Physik, Verlag Julius Springer, Berlin, (1926).

[13] K.Wang, R.R. Reeber, Appl. Phys. Lett. **9**, 11 (2001)

[14] S.Figge, H. Kroencke, D. Hommel, B.M. Epelbaum, Appl. Phys. Lett. **94**, 101915, (2009)

[15] G. G. Stoney, Proc. R. Soc. London, Ser. A **82** 172 (1909).

[16] L. B. Freund and S. Suresh, Thin Film Materials Cambridge University Press, (2003)

[17] L. B. Freund, J. Cryst. Growth **132**, 341 (1993).

[18] L. B. Freund, J. Mech. Phys. Solids **44**, 723 (1996).

[19] A. E. Romanov and J. S. Speck, Appl. Phys. Lett. **83**, 2569 (2003).

[20] H.M. Foronda , A.E. Romanov , E.C. Young , C. Robertson , G.E. Beltz , and J.S. Speck, J. of Appl. Phys. **120**, 035104 (2016)

[21] S.K. Mathis, A.E. Romanov, L.F. Chen, G.E. Beltz, W.Pompe, J.S. Speck, phys. Stat. sol. **179**, 125 (2000)

[22] W.H. Bragg, W.L. Bragg, Proceedings of the Royal Society A **88**, 605 (1913)

[23] A. F. Wright, J. Appl. Phys. **82**, 2833 (1997)

[24] Bauer G and Richter W, Optical characterization of epitaxial semiconductor layers High Resolution X-Ray Diffraction (Berlin: Springer) Ch. 6, (1996)

[25] W. Paszkowicz, R. Cerny, and S. Krukowski. Powder Diffr. **18**, 114 (2003).

[26] H. Angerer, D. Brunner, F. Freudenberg, O. Ambacher, M. Stutzmann, R. Hanopler, T. Metzger, E. Born, G. Dollinger, A. Bergmaier, S. Karsch, and H.-J. Kanorner. Appl. Phys. Lett. **71**, 1504 (1997).

Section 2:

The MOCVD Growth of $Al_xGa_{1-x}N$/AlN for Deep UV LEDs

Chapter 5: Introduction to UV LEDs

A light-emitting diode (LED) consists of a junction between two types of semiconducting materials: an "n-type" layer where current is carried by electrons and a "p-type" layer where carriers are positively charged holes [1]. The electrons and holes recombine at the junction to emit light under a forward bias. Since the initial discovery of the LED by Round in 1907 and Losev in 1928, there have been tremendous breakthroughs in the visible range of the electromagnetic spectrum including N. Holonyak's pioneering work on the first practical visible LED in the early 1960's, P.Marakusa and J. Pankove on blue LEDs in the early 1970's and the groundbreaking work of S. Nakamura in the 1990's [2]. Visible LEDs have now entered the age of maturity and are used in a variety of lighting applications.

The ultraviolet range is one of the relatively unexplored ranges of the electromagnetic spectrum for LEDs, ranging from 400 nm to ~100 nm. Near-Ultraviolet (N-UV) LEDs emit at 400-300 nm, Deep-Ultraviolet (D-UV) LEDS emit lower at 300 nm-200 nm and Far-Ultraviolet (F-UV) emit down in the 200 nm-122 nm range. Everything below 122 nm is ionizing radiation and is strong absorbed by the atmosphere. Ever since the discovery of III-nitride materials for optoelectronic devices, researchers have attempted to produce devices that emit at short wavelengths. The materials system (Al,In,Ga)N is perfect for short wavelength emission as it spans a wide range of wavelengths covering the deep UV, near UV, visible, and even infrared region. The band gap ranges from 0.7 eV to 6.2 eV.

UV devices with wavelengths longer than 360 nm generally have GaN or InGaN active regions. Milliwatt powers were first achieved by Mukai *et al* (1998) at 371 nm

using InGaN/AlGaN heterostructures [3]. Nakamura *et al* (1993) reported InGaN LEDs with peak wavelengths ranging from 400 nm to 410 nm [4]. UV devices at wavelengths less than 360 nm have AlGaN active regions or $Al_xGa_{1-x}N/Al_yGa_{1-y}N$ multi-quantum well (MQW) active regions. Khan *et al* (2001) [5] demonstrated LEDs with wavelengths ranging from 305 nm to 340 nm by using pulsed atomic layer epitaxy (PALE) via metalorganic chemical vapor deposition (MOCVD) of various AlGaN compositions on UV-transparent sapphire substrates. Later on, with the addition of an AlN/AlGaN superlattice, he was able to filter out even more defects, reducing the threading dislocation density (TDD), and bringing the emission wavelength down to 285 nm. Since then, it has become commonplace to use thick AlN buffer layers and with that, was able to demonstrate emission at 276 nm [6]. The efficiency of these devices is generally low, although much progress has been done in this area in the past few years. [7].

5.1 Applications for UV LEDs

We will focus on the deep UV spectrum (300 nm-200 nm) as we are most interested in applying the LEDs to light sources for disinfection and sterilization. At this spectrum the LEDS are germicidal, acting as mutagenic to bacteria, viruses and other microorganisms. At around 260-280 nm, UV will break down the molecular bonds within the microorganism's DNA, producing thymine dimers in their DNA, rendering them harmless and no longer able to grow or reproduce as shown in Fig. 5.1 [8]. Currently, mercury UV lamps are employed for this task, although soon to be replaced by LEDs. UV LEDs are more compact in structure, have lower power consumption, shorter stand by time, lower heat generation and are more environmentally friendly as they lack the use

of mercury, as shown in Fig. 5.2 [9]. Aside from replacing UV mercury lamps, UV LEDs show potential for use as fluorescent light sources for lighting, displays and chemical excitation as used for resin curing.

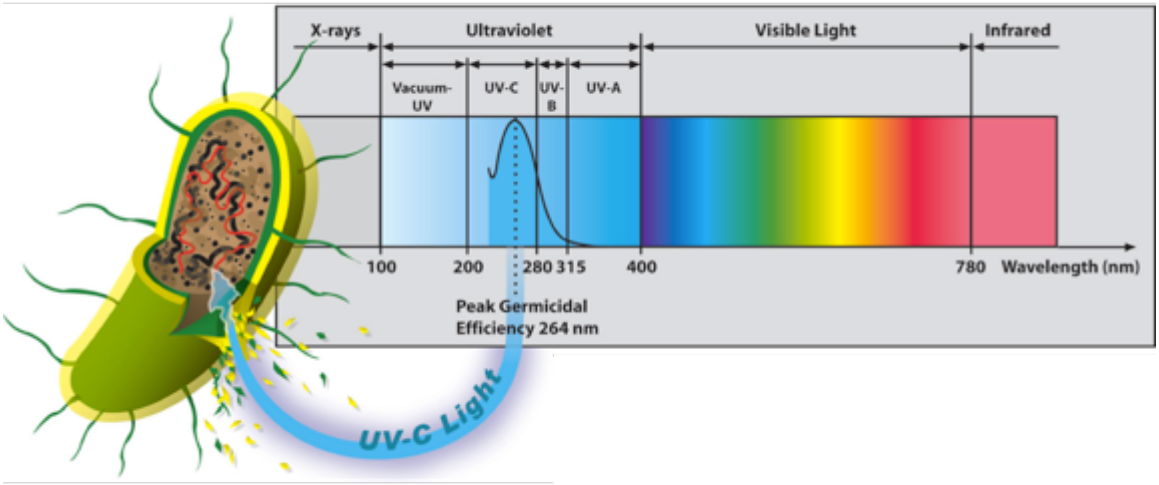

Fig. 5.1 Wavelength regime for UV spectrum. 265 nm is wavelength where UV light is has peak germicidal capabilities [8].

5.2 Areas of Special Attention in Deep UV LEDs

There are multiple issues to consider when growing $Al_xGa_{1-x}N/Al_yGa_{1-y}N$ D-UV LEDs. Increasing the Al concentration in the layers is necessary to emit at wavelengths low enough to be in the deep UV region, bringing with it a set of problems. To begin with, aluminum has a very high affinity to oxygen. This makes the incorporation of oxygen into AlGaN more likely as we increase the Al content, creating impurity sites in the forbidden region of the band gap, which are deep level defects in a semiconductor. In $Al_xGa_{1-x}N$, oxygen is known to be meta-stable as it changes from a shallow donor to deep

acceptor at the DX center with increasing Al composition and thus increasing band gap energy. The transition is reported to occur at x_{Al} ~27 % [10-12].

Increasing the Al content also makes it increasingly difficult to dope AlGaN n-type and especially p-type. Increasing above Al mole fractions of 30% leads to higher resistivity in the confinement layers and makes low resistance contacts difficult to attain as the contact barriers increase due to the high band gap of AlGaN [13-15]. On insulating substrates the n-AlGaN layer provides the lateral conductivity. However, with increasing Al content, the device becomes increasingly more resistive. Reducing the distance by which the current flows laterally mitigates this effect, which can be accomplished via micro-LEDs [16,17].

Another problem associated with AlGaN D-UV LEDs is light extraction. In order to reduce reabsorption effects, all device layers should have an Al content large enough to be transparent to the emitted light from the active region. When AlGaN is grown on relaxed GaN, the film is under tensile stress due to the smaller lattice constant of AlGaN relative to GaN. This leads to cracking when the films are grown past a critical thickness. If grown on an AlN layer, the opposite effect occurs where the film is then under compressive stress, which can also leads to cracking due to island coalescence during the initial stages of growth. Cracking can be minimized and even completely eliminated if one uses an Al-rich strain-compensating superlattice or grows a sufficiently thick buffer layer [18-21].

5.3 Epitaxial Layers in a UV LED

In this section we will introduce the epitaxial layers that make up a UV LED, specifically for the deep UV. We will discuss the buffer layer of AlN, and the growth of AlGaN for the n, p and MQWs. The basics of each layer will be discussed as well as a brief literature review for each.

5.3.1 Growth of AlN

The growth of high quality AlN is essential for the production of high performance UV optical devices. Given that high quality AlN bulk crystals are not a viable cost-effective option for large production, the growth of AlN buffer layers has been given a large amount of attention. The task of growing uniform high quality AlN layers is challenging, mainly due to the fact that the Al atoms are less mobile when compared to other group III elements such as Ga. AlN has a higher bonding energy, which further complicates crystallization. The sticking coefficient near unity of AlN also makes it difficult to grow two-dimensional AlN. All of these factors cause the growth of AlN to have poor growth rates along the lateral direction. AlN needs to be grown at high temperatures to aid the surface mobility of Al atoms and increase the diffusion length [21].

Another factor to consider is the compressive stresses of AlGaN on the underlying AlN layer. There is an in-plane lattice mismatch of ~2.4% between GaN and AlN, leading to a degradation of crystal quality due to misfit dislocations generated at the interface between AlN and AlGaN [21]. This section will discuss unique methods found in the literature of growing quality AlN layers for UV optical devices.

The two step growth method was demonstrated by Balakrishnan *et al* (2006) [22] under the supervision of Hiroshi Amano and Isaku Akasaki. Balakrishnan *et al* carried out two experimental series. The first involved growing a thick AlN layer between 1200 °C and 1400 °C. The film cools down to room temperature after growth and fully relaxes within the growth chamber, at which point a second thinner AlN layer is deposited at a higher temperature.

The initial base layer experiment improved crystal quality and growth rates with increasing growth temperate. The AlN had a FWHM of ~800 arc seconds at a growth rate of 1.61 μm/hr., when grown at 1350°C. However, the differences in thermal expansion between SiC and AlN lead to micro cracks and craters on the AlN surface, where it has a crack density of 8×10^5 cm^{-1} at 1350 °C. The surface of SiC roughens when exposed to a H_2/NH_3 environment at temperatures above 1000 °C.

In order to improve the AlN quality and overcome the crack generation problem, the second layer was deposited over the 2-micron thick base layer. Before the second layer deposition, the base layer was cooled to room temperature so as to relax completely. The growth was left in the chamber to reduce the possibility of surface oxidation. The subsequent growth of the 2nd layer used the base layer as the substrate, therefore effectively becoming homoepitaxy. The highest quality 2nd layer was obtained at 1350 °C over a base layer grown at 1250 °C, and showed an improvement in crystal quality after the second deposition. It was observed that growing the base layer too hot, at temperatures above 1250°C, led to degradation of the crystal quality as the FWHM increased. This can be attributed to the crack density increasing in the base layer;

degrading the surface and reducing the potential for smooth over layer growth of the second AlN layer.

The reduction in crack density of the second layer, down to 7 x 10^2 cm^{-2} from 3 x 10^4 cm^{-2}, was due to reduced tensile stress at 1250 °C. The presence of micro cracks and craters in the base layer acted as natural patterned trench allowing for over-layer growth. The nano-islands of AlN present in the base layer also acted as dislocation traps, reducing the density of dislocations. However, it is important to find a balance, as too many cracks on the base layer can hinder smooth over-layer growth and can decrease the smoothness of the film.

This Mg-AlN method was demonstrated by Asai *et al* (2010) [23], once again under the supervision of Hiroshi Amano and Isaku Akasaki. In this study a resistive Mg doped AlN layer was deposited over an undoped AlN layer at 1300°C. The purpose of this doped layer was to act as a basis to grow low dislocation density AlGaN, which will be discussed in the following section.

The study compared the growth of 3μm of AlGaN on an undoped and Mg-doped AlN layer, comparing the crystal quality and morphology. The manuscript reports an improvement in crystal quality over a spectrum of AlGaN compositions when AlN is doped with Mg compared to undoped AlN by a reduction in the (20-24) FWHM of the omega scan rocking curve. Additionally, TEM shows the reduction in the misfit dislocations generated by using Mg-AlN. This is due to the dislocations uniting and bending to coalesce and form loops, whereas in undoped AlN they propagate to the surface.

5.1.2 The Growth of AlGaN Layers

As mentioned previously, emitting below 360 nm requires AlGaN in the active region. AlGaN is doped n-type via disilane (Si_2H_6) and p-type via bis-cyclopentadienyl magnesium (Cp_2Mg). The barrier and buffer layer will be composed of the same composition of Al, which is to some degree greater than the Al fraction in the well. Fig. 5.2 shows the necessary Al fraction to emit at wavelengths in the deep UV from 222 nm-273 nm from Hirayama *et al* (2011) [24]. The data point for our desired emission, 280nm, is extrapolated and shown to be 42% Al for the well and 64% Al for the buffer layers (both n- and p-) as well as the barrier between the quantum wells. Maeda *et al* (2013) reports a maximum external quantum efficiency (EQE) of 5.5% for 275 nm AlGaN LEDs with a p-AlGaN contact layer, while Shatalov *et al* (2012*)* reports 10.4% [25,26]

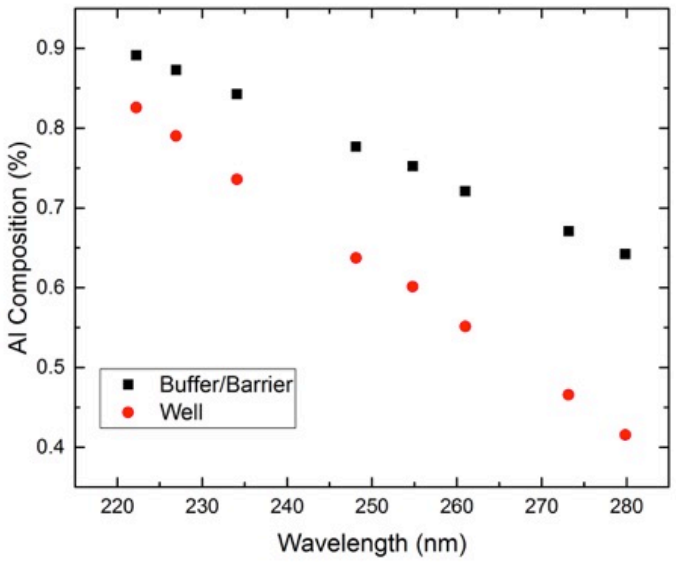

Fig. 5.2 Ideal Al Composition for Buffer/Barrier and Well for Targeted Wavelength Emission

The growth of AlGaN requires N_2 as the carrier gas as it gives a uniform Al composition across a varying V/III ratio. When grown using H_2 carrier gas or an H_2/N_2 carrier gas mix, there is a fluctuation in the Al composition as the NH_3 flow is varied. This is attributed to the increase in the vapor pressure of volatile Ga-H species present when H_2 is a component of the carrier gas, leading to a decreased Ga desorption [27]. This section will discuss the growth, optimization, and challenges of the n- and p-layers and the $Al_xGa_{1-x}N/Al_yGa_{1-y}N$ MQWs as well as current benchmarks.

5.3.2.a n-Type AlGaN

The following experiments in this section were performed by Craig Moe and can been seen in further detail in his thesis [21]. Using silicon carbide (SiC) substrates not only allows for lower dislocation density in AlGaN via reduced TDD in the AlN layer, but also broadens the growth window for which to obtain doped films of high mobility and carrier concentration. The n-doping of AlGaN is quite difficult on sapphire as oxygen, carbon and cation vacancies are all compensating acceptors in AlGaN, meaning they reduce the donor concentration via neutralizing charges. Given the low pressure required to grow AlGaN, there will be an increase in impurity levels.

In order to mitigate this, Moe *et al* investigated a range of NH_3 flows to reduce cation vacancies and impurity incorporation [28-31]. A series of AlGaN:Si (silicon doped AlGaN) films at varying NH_3 flows were grown using a constant Si concentration calibrated to 3×10^{19} cm^{-3} on SiC and sapphire substrates. The electron carrier concentration as a function of ammonia flow are plotted in Fig. 5.3. Impurity incorporation is expected to decrease as more NH_3 is flown, as it increases the V/III ratio,

therefore increasing the electron concentration. The carrier concentration is always greater on SiC, increasing with increasing NH_3 flow, while the carrier concentration decreases on sapphire. The highest electron carrier concentration was 1.7 x 10^{19} cm^{-3} at 1.4 slpm of NH_3, indicating that carbon and oxygen is suppressed. Furthermore, cation vacancies are not a significant compensation agent as in sapphire, where the impurity incorporation cannot be suppressed by increasing the V/III ratio [32].

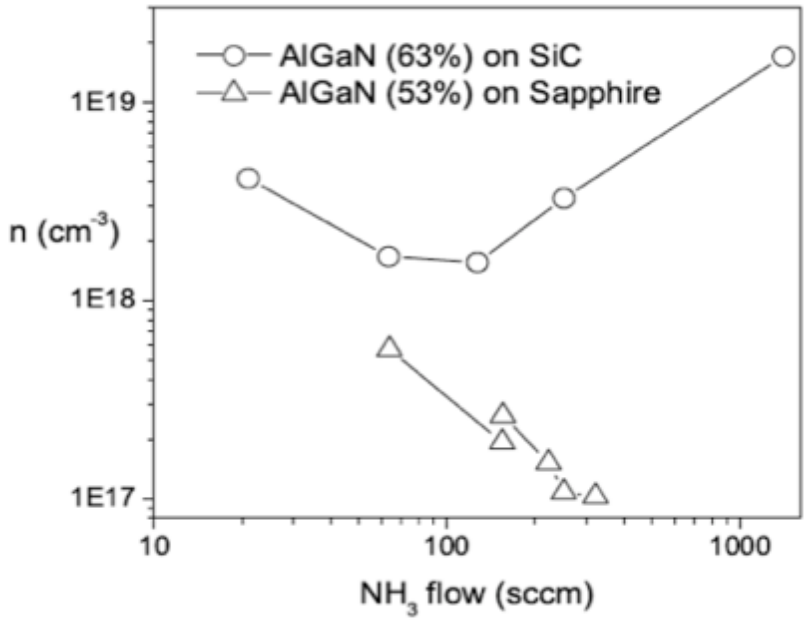

Fig. 5.3 Electron carrier concentration as a function of NH_3 Flow for AlGaN [21].

Fig. 5.4 plots the electron concentration and electron mobility of AlGaN:Si under H_2 and N_2 ambient conditions as a function of the Si/(Al+Ga) ratio. Moe *et al* increased the concentration of Si, the electron concentration increases, until it saturates at the ratio of 8 x 10^{-3}. However, the electron mobility linearly decrease with increasing Si, under both ambient condtions. This trend it to be expected. An increase in carriers causes a decrease in the mobility of carriers. The optimal ratio of Si/(Al+Ga) seems to be 8 x 10^{-3}.

Any additional increase in Si causes no change in the carrier concentration but later produces a reduction in the mobility of the n-AlGaN.

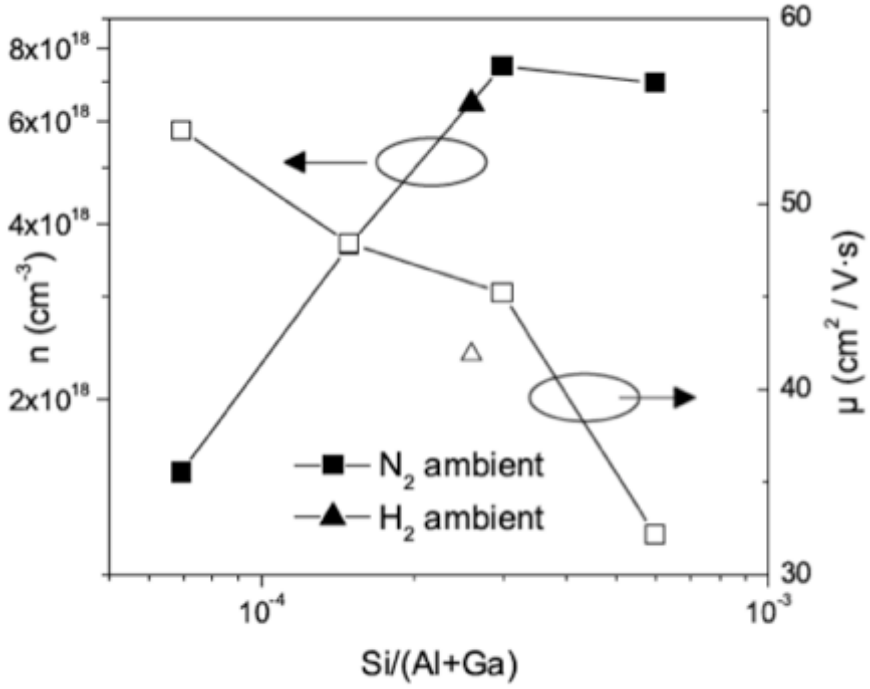

Fig. 5.4 Electron carrier concentration and mobility as a function of optimal Si flow [21].

5.3.2.b p-type AlGaN

The following experiments in this section were performed by Craig Moe unless otherwise stated and can been seen in further detail in his thesis [21]. Highly conductive p-type AlGaN is even more difficult to grow than n-AlGaN. A difference of six orders of magnitude between the magnesium content incorporated (10^{20} cm^{-3}) and the hole concentration (10^{14} cm^{-3}) has been reported for $Al_{0.7}Ga_{0.3}N$ [32]. This is in part due to a higher Al content, which in turn requires greater dopant activation energy and an increased dislocation density in more compensating sites.

To investigate the optimal growth conditions for p-AlGaN, Moe *et al* grew a series of AlGaN:Mg (magnesium doped AlGaN) growths under H_2 conditions to examine the conductivity and hole concentration in p-AlGaN. The samples were annealed at various temperatures and their resistivity was measured at 450 K. Higher temperature annealing up to 1000 °C produced the best results, with an optimal annealing time of 3 minutes. Additional annealing time showed no improvement in conductivity. The addition of a SiO_2 cap decreased the resistivity and provided better ohmic contacts after the metal deposition. This is attributed to SiO_2 preventing the formation of nitrogen vacancies on the p-GaN contact layer, which acts as an electron donor, compensating the hole concentration on the surface.

When varying the growth temperature and holding the Cp_2Mg constant, temperature dependence in the Mg incorporation was observed. The greater the growth temperature, the less Mg was incorporated, indicating that the dopant was desorbing during deposition at increasing temperatures as seen in the SIMS data in Fig. 5.5 [21].

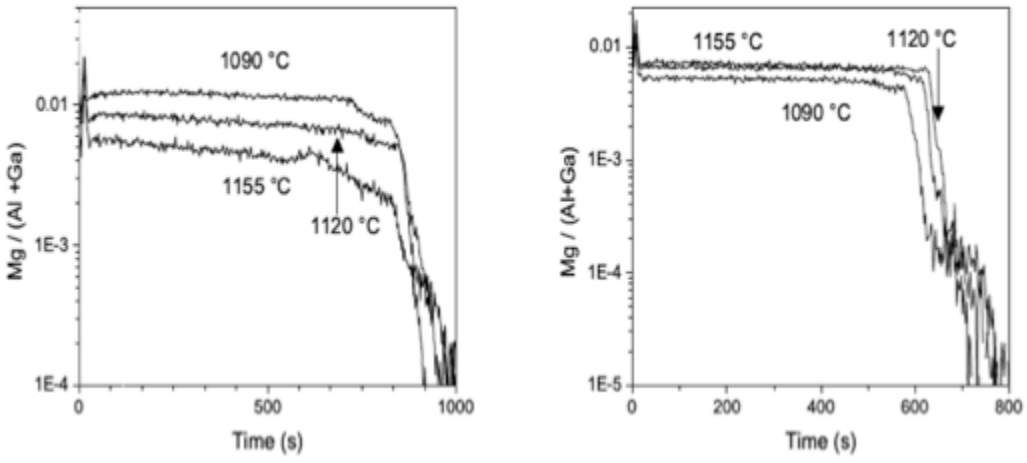

Fig. 5.5 Mg concentration varies with growth temperature via SIMS [21].

From these profiles, it is clear that the resistivity is proportional to the growth temperature, indicating that the film becomes less conductive with temperature increases, as the Mg cannot fully adsorb onto the surface. Holding the temperature constant and varying the Cp_2Mg flow showed similar results. With an increase up to 100 sccm Cp_2Mg, the surface morphology changed due to an overabundance of Mg. The resistivity increased linearly with increasing Mg, shown graphically in Fig. 5.6.

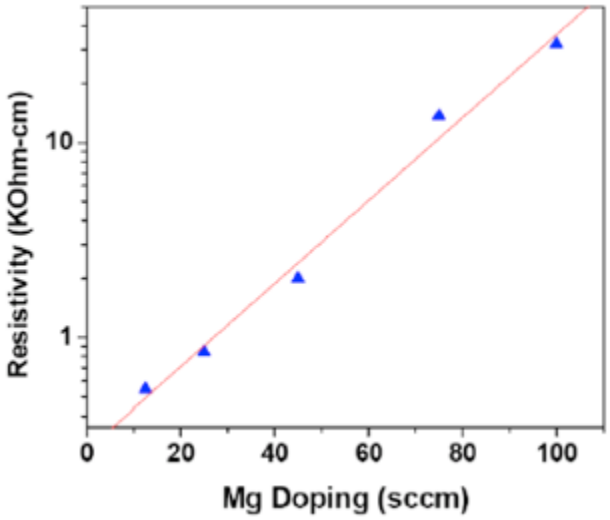

Fig. 5.6 Resistivity of AlGaN:Mg as a function of Mg doping [21].

The use of a transparent p-AlGaN contact layer in combination with a highly reflective p-type electrode by Maeda *et al* (2013) improved the light extraction efficiency (LEE). The EQE increased from 2% to 5.5%, by 1.7 times. The UV LED with a strongly UV absorbent p-GaN contact layer has a LEE of 8%. By replacing it with transparent p-AlGaN and replacing Ni/Au electrodes with highly reflective Ni/Al, we anticipate an increase in LEE to 40%.

Shatalov *et al* (2012) demonstrated a deep UV LED with an EQE of 10.4% at 20 mA at 278 nm. This result was attributed to reducing the dislocation density of their AlN on sapphire to less than 2 x 10^8 cm^{-2} by their patented pulsed growth method. They also improved the light extraction by using UV transparent p-type cladding and contact layers, UV reflecting ohmic contacts, and a UV transparent chip encapsulant with optimized shape and refractive index.

5.3.2c $Al_xGa_{1-x}N/Al_yGa_{1-y}N$ MQWs

The quantum well composition for 280 nm emission is 42% Al and 64% for the barriers separating them. Using AlGaN based MQWs with wavelengths ranging from 222-351 nm, Hirayama *et al* (2011) demonstrated 50-80% IQE and a max EQE of 1.8% and 2.8% for 247 nm and 270 nm emissions, respectively. The electroluminescence (EL) spectra obtained in Hirayama *et al* (2011) were single peaks, indicating negligible deep level emission. The quantum well thickness ranged from 1.3-1.7 nm and the barriers were ~7 nm. Thin quantum wells were necessary to obtain high IQE via suppression of the polarization field in the well, where the heterointerface must also be atomically smooth. Well thickness was investigated and showed little variation in photoluminescence (PL), with only the thinnest wells suffering a blue shift and loss in intensity. However, increasing the barrier thickness up to 10.5 nm showed a significant improvement in performance, with no shift in peak wavelength.

Fujioka *et al* (2014) at Nichia reported high output power deep UV LEDs emitting at 255/280/310 nm [33]. The active layer consisted of two pairs of 4 nm thick $Al_{0.45}Ga_{0.55}N$ wells and 2.5 nm thick $Al_{0.56}Ga_{0.44}N$ barriers along with AlGaN:Mg for hole

injection and a p-GaN contact layer. Most notable is the high output power for 280 nm emission of 18 mW using a forward current of 100 mA; however, this is only achievable when the forward voltage is driven to 16.6 V. The EQE is 2.2%, although not as high as when using an AlGaN:Mg contact layer as in Maeda *et al* (2013). The 280 nm emission has the highest light output per driven current and the lowest forward voltage.

5.3.3 State of the Art

Figure 5.7 plots the external quantum efficiency as a function of emission wavelength for the UV community. The plot ranges from the Near UV to the Deep UV. Focusing in on the deep UV, the best EQE results are from companies such as RIKEN, SETi, Nichia, UV Craftory, and Crystal IS. All growths are done on either sapphire substrates or single crystal AlN substrates and involve some sort of transparent p-AlGaN contact layer or optimized encapsulation technique for the UV LEDs. Furthermore, all growths are c-plane oriented.

The max EQE in the deep UV is 20.3% by Takano *et al* (2017) from RIKEN [34, 35]. Their UV LED, grown on c-plane oriented patterned sapphire substrates, had improved light extraction by implementing a transparent magnesium doped AlGaN contact layer, a Rh mirror electrode, and an encapsulation resin. The combination of these features significantly improved the output power and the EQE of UV-LEDs. With these features, they were able to achieve maximum EQE of 20.3% at an emission wavelength of 275 nm at a 20-mA direct current. This result is comparable to LEDs emitting in the Near UV (~365 nm) made by Nichia.

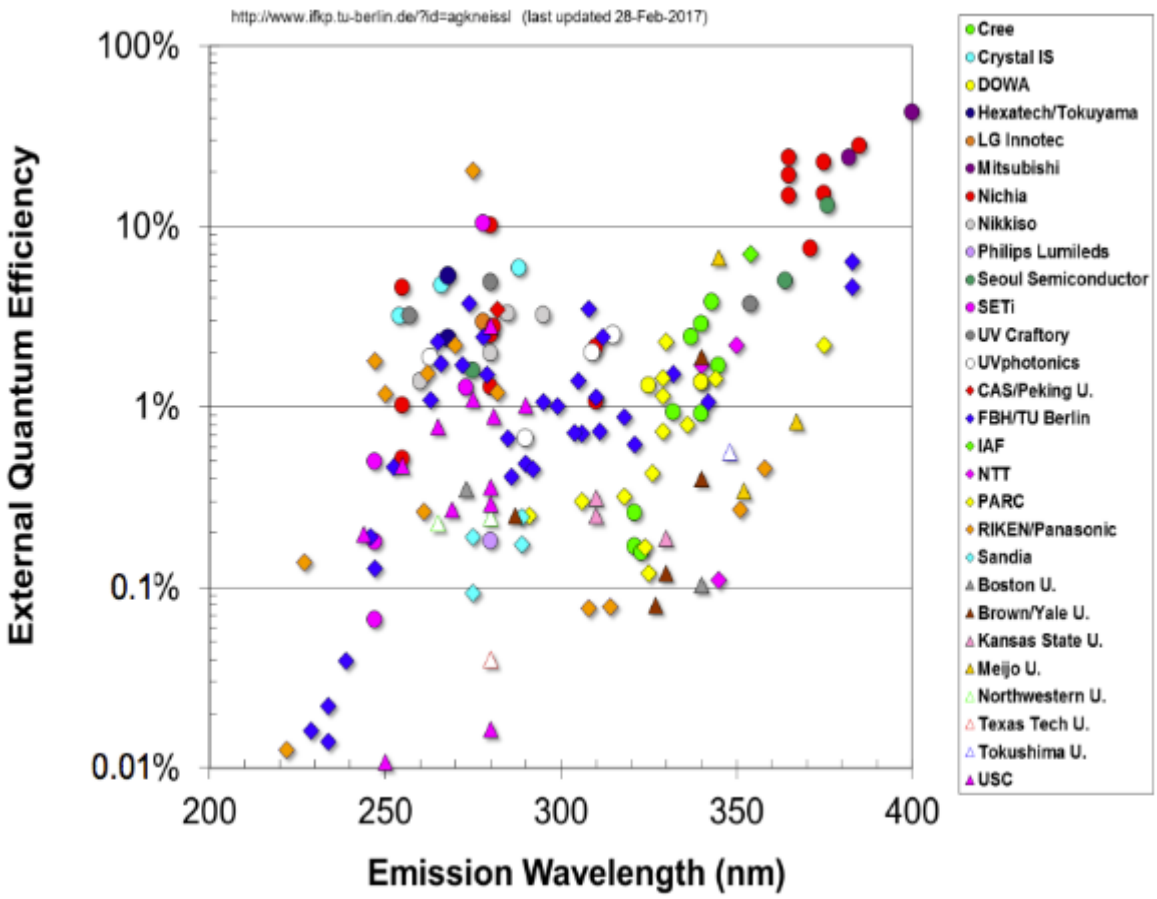

Figure 5.7. EQE as a Function of Emission Wavelength for the UV Community [34].

5.4 Section Overview

In the second section of this thesis we will focus on the MOCVD growth of AlN and AlGaN with high Al composition for deep UV devices. It will be focused heavily on growth optimization with studies focusing on changing the numerous parameters available on the MOCVD (temperature, gas flows, etc.).

The growth of AlN will be discussed first. The initial campaign on the Veeco will be introduced; primarily how the source efficiency of AlN was improved. The growth of AlN on the SR4000HT will then be discussed. We will focus on how we reduced the

dislocation density of AlN grown on the SR4000HT by changing the growth modes of the layer.

We will also discuss the growth studies conducted for growing AlGaN. First, finding the optimal conditions for growing smooth undoped AlGaN for a variety of alloy compositions as the UV LED will need AlGaN with Al% between 40-65%. Then the growth of AlGaN:Si will be discussed, primarily electrical characterization as well as SIMS to analyze the Si incorporation.

References

[1] B. Dumé, LEDs move into the ultraviolet, physicsworld.com, May 17, (2006)

[2] E.Schubert, Light Emitting Diodes 2nd edition, Cambride University Press, (2006)

[3] T.Mukai, D. Morita D, S. Nakamura , J. Cryst. Growth **189**, 778 (1998)

[4] S. Nakamura, M. Senoh, T. Mukai, Appl. Phys. Lett. **62**, L8 (1993)

[5] M. A. Khan, V. Adivarahan, J. P. Zhang, C. Chen, E. Kuokstis, A. Chitnis, M. Shatalov, J. W. Yang, G. Simin, Jpn. J. Appl. Phys. **40**, L1308 (2001)

[6] A. Yasan, R. McClintock, K. Mayes, D. Shiell, L. Gautero, S. R. Darvish, P. Kung, M. Razeghi, Appl. Phys. Lett. **83**, 4701 (2003)

[7] M.Kneissl, T.Kolbe, C.Chua, V.Kueller, N.Lobo, J.Stellmach, A. Knauer, H. Rodriguez, S. Einfeldt, Z. Yang, N. M. Johnson, and M. Weyers, Semicond. Sci. Technol. **520**, 014036 (2011).

[8] W.J. Kowalski, W.P. Bahnfleth, D.L. Witham , B.F. Severin B.F, T.S. Whittam, ."Mathematical Modeling of Ultraviolet Germicidal Irradiation for Air Disinfection", (2000)

[9] Y.Muramoto, M.Kimura and S.Nouda, Semicond. Sci. Technol. **29**, 084004 (2014)

[10] R.B. Chung, F. Wu, R. Shivaraman, S. Keller, S.P. DenBaars, J.S. Speck, S. Nakamura, J. Cryst. Grow. 324, 163 (2011)

[11] M.D. McCluskey, N.M. Johnson, C.G. Van de Walle , D.P. Bour, M. Kneissl W. Walukiewicz, Phys. Rev. Lett. **80**, 4008 (1998)

[12] C. Wetzel, H. Amano, I. Akasaki, J.W. Ager III, I. Grzegory, B.K. Meyer, Physica B **23**, 302 (2001)

[13] M. Katsuragawa, S. Sota, M. Komori, C. Anbe, T. Takeuchi, H. Sakai H. Amano I. Akasaki, J. Cryst. Growth **528**, 189 (1998)

[14] I.D. Goepfert, E.F. Schubert, A. Osinsky, P.E. Norris, Electron. Lett. **35**, 1109 (1999)

[15] H.X. Jiang, J.Y. Lin, Opto-Electron. Rev. **10**, 271 (2002)

[16] K.H. Kim, J. Li, S.X. Jin, J.Y. Lin, H.X. Jiang, Appl. Phys. Lett. **83**, 1231 (2003)

[17] M.A. Khan, Proc. SPIE **5530**, 224 (2004)

[18] S.Hearne, J. Han, S.R. Lee, I.S.T. Tsong, Appl. Phys. Lett., **76**, 1534, (2000)

[19] J. Han, K.E. Waldrip, S.R. Lee, J.J. Figiel, Hearne S. J., Petersen G. A., and Myers S. M. ,Appl. Phys. Lett. **78**, 67 (2001)

[20] J.P. Zhang, H.M. Wang, M.E. Gaevski, C.Q. Chen, Q. Fareed, J.W. Yang, G. Simin M.A. Khan, Appl. Phys. Lett. **80**, 3542 (2002)

[21] C. Moe, Growth and Fabrication of Deep Ultraviolet Light Emitting Diodes on Silicon Carbide Substrates, UCSB Thesis (2007)

[22] K. Balakrishnan, H.Amano, I.Akasaki, Phys. Stat. Sol. (c) **3**, 6, (2006)

[23] T. Asai, K. Nonaka, K. Ban, K. Nagata, K. Nagamatsu, M. Iwaya, S. Kamiyama, H. Amano, and I. Akasaki, Phys. Status Solidi C **7**, 2101 (2010)

[24] H. Hirayama, SPIE-OSA-IEEE, **7987**, (2011)

[25] N. Maeda and H. Hirayama, Phys. Status Solidi C **10**, 1521 (2013)

[26] M. Shatalov, R. Gaska, C. Moe, G. Garrett, M. Wraback, Appl. Phys. Exp. **5,** 082101 (2012)

[27] S. Keller, G. Parish, P. T. Fini, S. Heikman, C.-H. Chen, N. Zhang, S. DenBaars, U. Mishra, J. of Appl. Phys. **86**, 5850 (1999)

[28] M. D. McCluskey, N. M. Johnson, C. G. Van de Walle, D. Bour, M. Kneissl, W. Walukiewicz, Phys. Rev. Lett. **80,** 4008 (1998)

[29] S. Fisher, C. Wetzel, E. Haller, B. Meyer, Appl. Phys. Lett. **67**, 1928 (1995)

[30] C. Van de Walle, C. Stampfl, J. Neugebauer, M. D. McCluskey, N. M. Johnson, J. Nitride Semicond. Res **4S**1, G10.4 (1999)

[31] T. Onuma, S. Chichibu, A. Uedono, T. Sota, P. Cantu, T. M. Katona, J. F. Keading, S. Keller, U. K. Mishra, S. Nakamura, S. P. DenBaars, J. of Appl. Phys. **95**, 2495 (2004)

[32] P. Cantu, S. Keller, U. Mishra, S. DenBaars, Appl. Phys. Lett. **82**, 3683(2003)

[33] A Fujioka, K Asada, H Yamada, T Ohtsuka, T Ogawa, T Kosugi,D Kishikawa and T Mukai, Semicond. Sci. Technol. **29,** 084005 (2014)

[34] https://www.ifkp.tu-berlin.de/fileadmin/i1/Kneissl/UV_LED_Efficiency_2017.pdf

[35] T. Takano, T. Mino, J. Sakai, N. Noguchi, K. Tsubaki, and H. Hirayama, Applied Physics Express, **10**, 031002 (2017)

Chapter 6: Reactor Designs and Substrates

In this chapter we will discuss everything prior to growing. In particular the two reactors that were used for the UV project and the substrates which were available to grow AlGaN/AlN structures on.

MOCVD reactors suffer from particle/defect generation from gas phase pre-reactions, wall coatings, depletion, back diffusion, re-evaporization, etc. and must all be considered when growing on the reactor. Schematics of the Veeco p-75 Turbodisc reactor and Taiyo Nippon Sanso SR4000HT reactors will be displayed and the advantages/disadvantages to each system will be discussed. Growth conditions such as temperature, gas flow, and pressure will also be discussed in relation to the reactor of interest and how it affects the growth of AlN and AlGaN for this project.

This section will also discuss the growth of AlN on foreign and native substrates. Previous work will go into detail regarding crystal quality, surface morphology and other microstructural characteristics to help in deciding which substrate was the best choice for the UV project. The reduction of threading dislocations is crucial in choosing an appropriate substrate, but so is the price.

6.1 Reactor Design

Two reactors were used during the growth of AlN and AlGaN for this generation of the UV project. The first reactor was the Veeco P-75 Turbodisc. After it' shortcomings became apparent, the university upgraded to SR4000HT made by Taiyo Nippon Sanso.

6.1.1 Veeco P-75 Turbosisc

The Veeco P-75 Turbodisc reactor was the first reactor used for the UV project. It is a vertical reactor, where gas passes down from the top and over and across the wafer. The reactor pressure ranges from 50-1000 torr, but is run at low pressure for AlN growths (100 torr). The substrate temperature can reach a maximum temperature of 1130 °C. The maximum flow rate of total gas flowing into the reactor is 250 standard liters per minute. The spindle rotates at a maximum revolution of 1,500 revolutions per minute. One advantage of the vertical reactor is that it is combined with rotation of the substrate, which radially grades the reactant concentration to counter reactant depletion and maintain uniformity in composition and thickness, which is non-existent in horizontal reactors. Another advantage to the vertical reactor is that it can be rotated at speeds where the viscous drag generates a pumping action, which counters thermal buoyancy and brings the streamlines down onto the surface. This pulling of the streamline combined with controlling reactant distribution has produced very high quality epitaxial films [1].

A cross-section and plan view schematic of the vertical MOCVD reactor chamber and flow flange is illustrated in Fig. 6.1 (a) and 6.1 (b), respectively. In Fig. 6.1 (a) the reactor free height is approximately 10 cm, with a susceptor diameter of 7.62 cm. Fig. 6.1 (b) illustrates the location of the alkyl, hydride and carrier gas nozzles on the flow flange. Fig. 6.1 (c) is a schematic illustrating the positioning of the alkyl inner/outer injectors on the flow flange. The alkyl inner/outer injectors are positioned an optimal distance from one another to provide the best growth rate and deposition uniformity over the wafer [2].

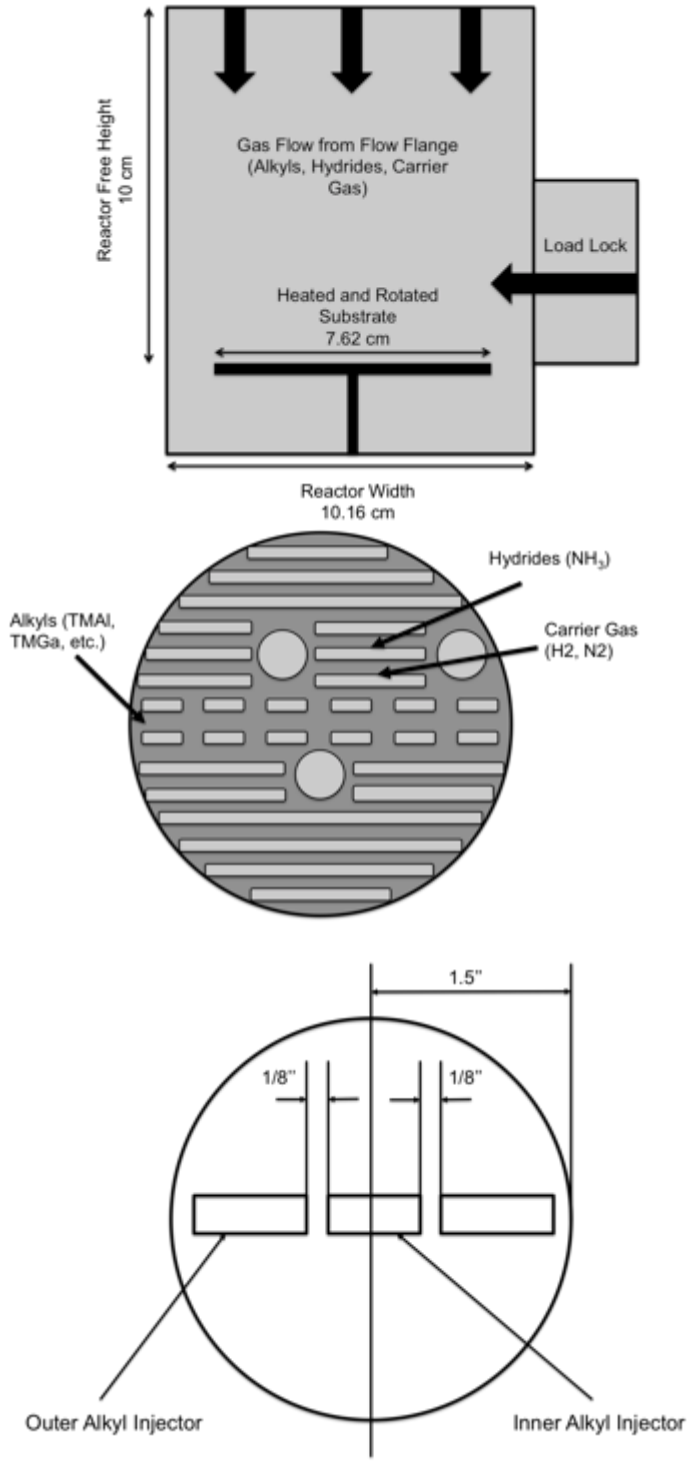

Fig. 6.1 (a.) A cross-section and **(b.)** plan view of the vertical MOCVD reactor chamber and flow flange. **(c.)** Schematic illustrating the positioning of the alkyl inner/outer injectors on the reactor flow flange.

6.1.2 SR4000HT

The SR4000HT is a low-pressure MOVPE reactor with a susceptor capacity of three 2-in.-diameter wafers. Fig. 6.2 shows a schematic of the reactor. This horizontal reactor was equipped with a trilayer gas injection nozzle to suppress the hazardous pre-reaction effectively in the gas phase. In addition, a new heater unit was designed to achieve growth temperatures up to 1300°C with a uniformity of ±1 °C to obtain a high-quality AlN layers.

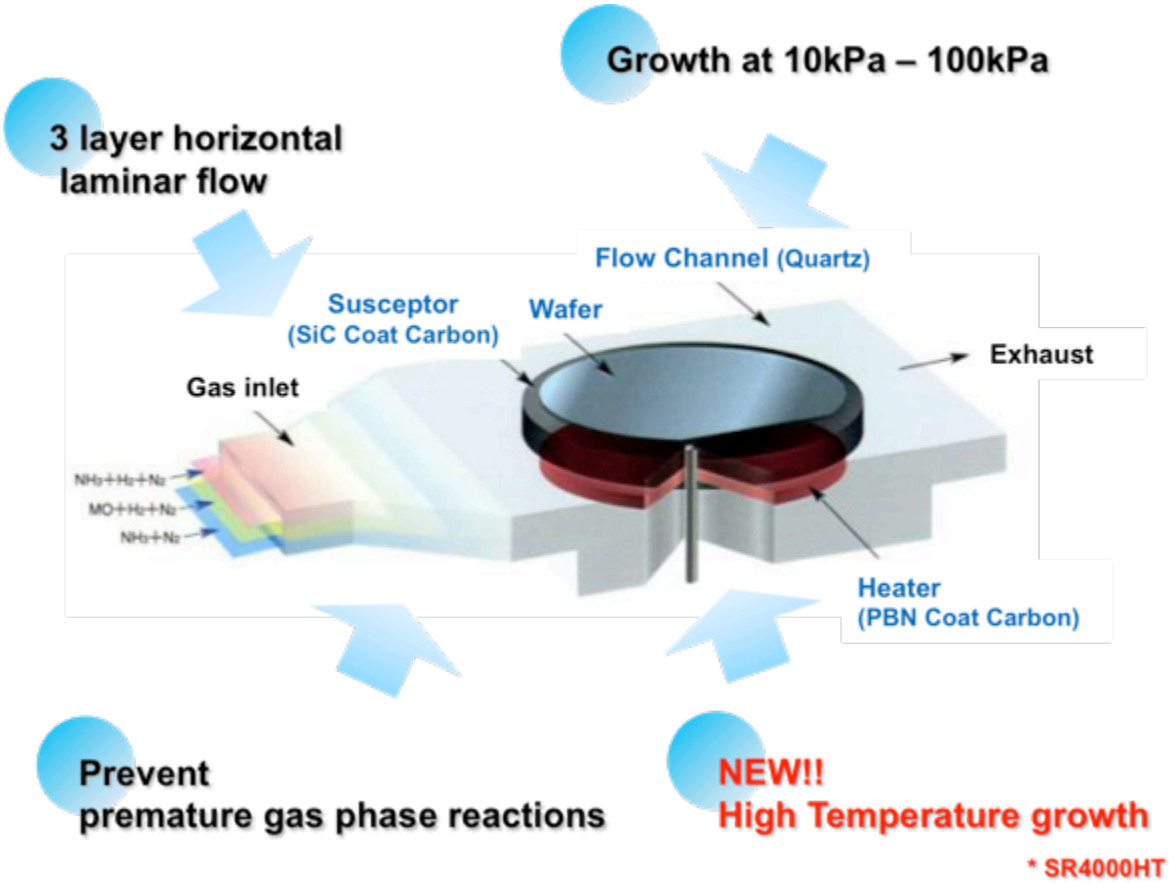

Fig. 6.2 Schematic of TNSC high temperature MOCVD SR4000HT (figure provided by Taiyo Nippon Sanso)

There are two major factors that make this design of horizontal reactors achieve such precise growth uniformity. The first is the design of the heating system in the reactor. The heater is set up below the susceptor and is surrounded by a radiation shield that is controlled independently to achieve a uniform temperature on the growth surface. The susceptor is 250 nm in diameter and is heated by electrical resistance heaters. The wafers are rotated with the susceptor to attain a uniform growth at approximately 10 revolutions per minute.

The other factor is the trilayer gas injection nozzle discussed previously. In this reactor, the group V species and hydrogen carrier gas, group III species and hydrogen carrier gas, and purging gas flows reach the reactor separately, and come in via upper, middle, and lower channels, respectively. Each flow is controlled independently to discover an optimum growth condition. This trilayer separation method is used to improve the organometallic consumption because any unnecessary gas flow in the upper stream is eliminated. It is also quite effective in reducing the V/III ratio as the concentration of hydride gases is controlled separately by a change in the upper to middle flow channel [3-5].

One of the main advantages for the UV project that the SR4000HT provides is the increase in growth temperature. Fig. 6.3provided by Taiyo Nippon Sanso shows the increase in growth temperature as a function of distance from the susceptor center. The blue data points show the variability in the surface temperature before adding a Boron Nitride (BN) cover over the top and bottom flow channel. The temperature is approximately 1285 °C around the wafer pocket. The red data points are recorded after using a Boron Nitride cover over the top and bottom flows channel. A marked increase in

temperature is noted with the BN covers, where the surface temperature increased to approximately 1310 °C with a variability of around 20 °C.

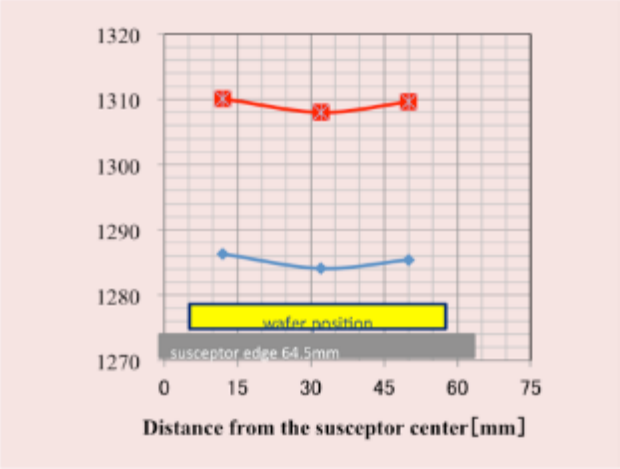

Fig. 6.3 Growth Temperature Variability in SR4000HT as Function of Distance From the Susceptor (Figure Provided by Taiyo Nippon Sanso)

Fig. 6.4 displays the variability in the on- and off-axis rocking curve FHWM of AlN grown by Taiyo Nippon Sanso using the SR4000HT as a function of the distance from the wafer center as perfomed by Taiyo Nippon Sanso. The results show good uniformity over the whole wafer by adjusting the temperature uniformity of the AlN growth as shown previously in Fig. 6.3. The FWHM of the (0002) omega rocking curve scans are approximately 225 arc seconds for a 3 μm thick film as grown by Taiyo Nippon Sanso. The $(10\bar{1}2)$ omega rocking curve scan FWHM show more variability than the on-axis FWHM, as to be expected. The values range from 400 arc seconds to approximately 425 arc seconds as we move from the center to wafer edge. Overall, these results are quite acceptable as there is always a ~30 arc second variability in FWHM omega rocking curve scan.

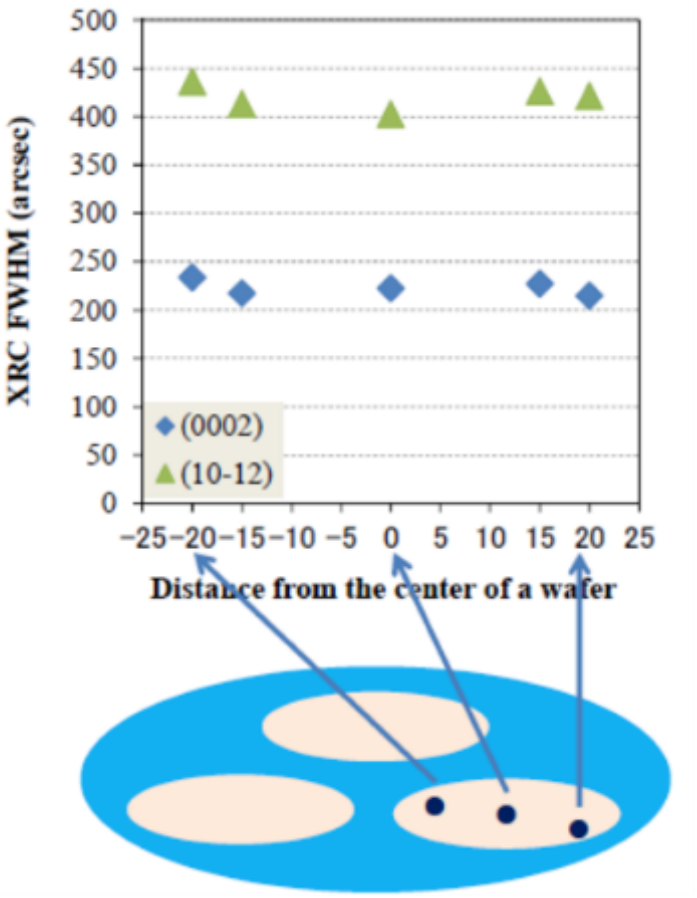

Fig. 6.4 Rocking Curve FWHM Variability in SR4000HT (Figure Provided by Taiyo Nippon Sanso)

Finally, the SR4000HT will also be used to grow AlGaN. Fig. 6.5 was provided by Taiyo Nippon Sanso and displays the projected growth rate of AlGaN using the SR4000HT. The growth rate is plotted as a function of growth temperature for varying V/III ratios. It is shown that high V/III ratios (1488) have a lower growth rate (3.5 μm/hr) compared to ~7 μm/hr at low V/III ratios (744). Lowering the V/III ratio by half, increased the growth rate two fold. Additionally, changing the ratio of TMAl/MO from 0.5 to 0.6 does not affect the growth rate.

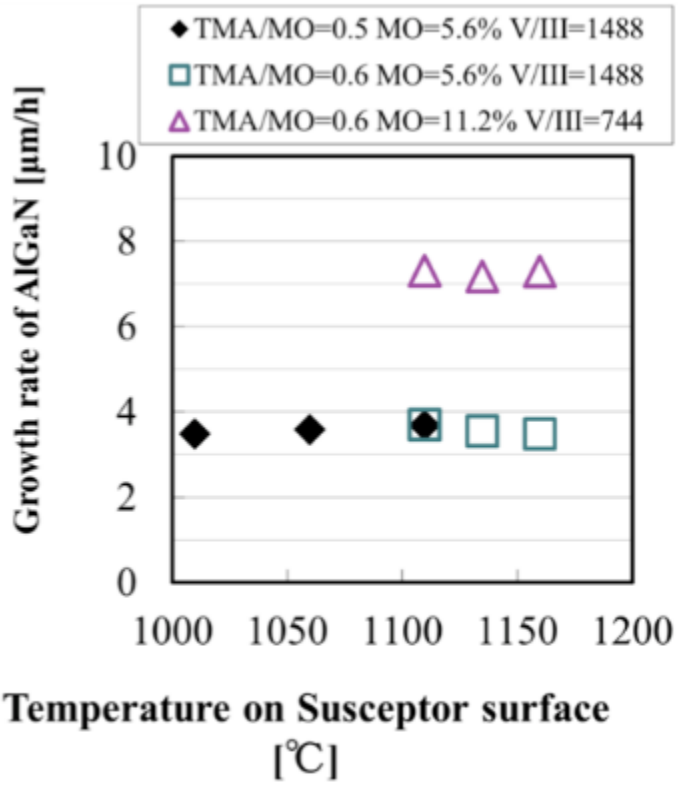

Fig. 6.5.Growth Rate of AlGaN as a function of temperature for SR4000HT (Figure Provided by Taiyo Nippon Sanso)

6.2 Substrate Selection: Sapphire, Silicon Carbide and Bulk AlN.

6.2.1 Sapphire

Sapphire is the most common substrate choice for the growth of AlN layers. To begin with, it is fully transparent at low wavelengths (all the way down to 170 nm), which makes it ideal for UV devices and it is also fairly cheap and easy to come by. Asif Khan utilized a pulsed atomic layer epitaxy (PALE) technique to deposit AlN/AlGaN layer structures over sapphire to reduce the number of defects and nonradiative

recombination. His group was the first to report milliwatt power deep UV LEDs over sapphire with an emission wavelength of 278 nm using AlGaN MQWs. [6].

The primary disadvantages to using sapphire substrates come from its insulating features; the fabrication of vertical devices cannot be realized without removing the substrate. It also contains a large oxygen content, which will contaminate the films when grown at exceedingly high temperatures [7].

6.2.2 AlN Substrates

Ideally, UV LEDs with high percent Al content AlGaN would be deposited on native AlN substrates. Implementing complicated growth techniques / fabrication methods would no longer be necessary to compensate for heteroepitaxial mismatch. Unfortunately the AlN bulk crystal technology is still in the developmental stage, and products on the market are fairly expensive and unreliable in terms of the threading dislocation density reported. Recently, groups such as Sltako Zitar's at North Carolina State University have been growing AlGaN on native AlN substrates as they work closely with Hexatech, a company that grows single crystal AlN in North Carolina. Growing on AlN substrates would obviously hold numerous advantages, however at this stage of the project at UCSB, it is not financially responsible or feasible to do so.

6.2.3 Silicon Carbide

Silicon Carbide (SiC) doped n-type with phosphorus, holds numerous advantages over sapphire as a substrate for AlN deposition. The lattice mismatch between SiC and the entire AlGaN materials system is much less than with sapphire. The coefficient of

thermal expansion of SiC (4.0 x 10^{-6} K^{-1}) is close to that of AlN (4.15 x 10^{-6} K^{-1}) compared to sapphire (7.1 x 10^{-6} K^{-1}). Phosphorus-doped SiC is also a conducting substrate, making it suitable for use in vertically conducting devices [8,9].

An advantage for SiC substrates is the reduction in impurities when depositing AlN on SiC at high V/III growth conditions. AlN on sapphire is very susceptible to high impurities because of aluminum's affinity for oxygen, which is abundant in sapphire and released during a high temperature bakes/growths. Growing at low pressures, which is typical when growing AlN / AlGaN, increases impurity incorporation. When growing material on sapphire substrates, low V/III ratios are necessary but unfortunately also increase impurity incorporation. The carbon and oxygen impurities compete with nitrogen for the group V lattice site. Secondary Ion Mass Spectroscopy (SIMS) data (from Craig Moe's thesis [7]) of AlN grown on SiC and sapphire (Fig. 6.6) shows that the impurity incorporation is higher for sapphire. The oxygen impurities in AlN is two to five orders of magnitude higher on sapphire than on SiC, due primarily to the sapphire substrate's high oxygen content [10].

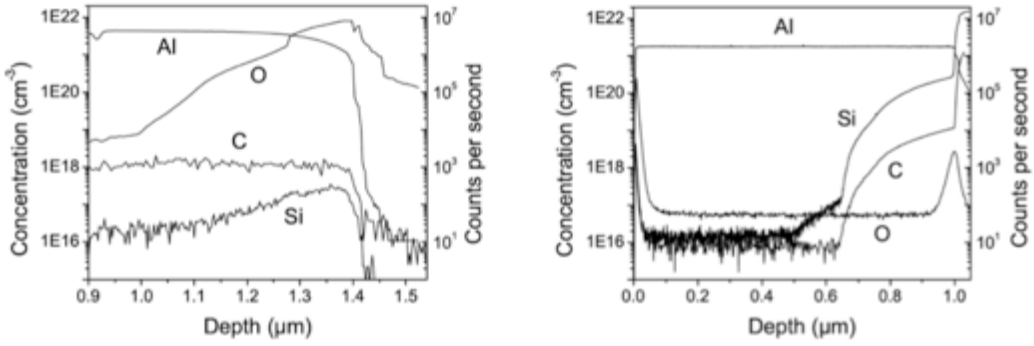

Fig. 6.6 SIMS of AlN growth on sapphire and SiC [7]

For the reasons discussed above, we have decided to use SiC as the substrate of choice for the deep UV project. However, SiC's small band gap relative to that of AlGaN at the compositions necessary for emission in the deep UV spectrum presents a major disadvantage to growing on SiC. A significant portion of the light emitted from the quantum well will be immediately reabsorbed by the SiC substrate. For this reason, special attention must be given to the substrate removal process in order to improve light extraction.

One of the most important features of this project is removing the SiC. This is a completely separate and very challenging project undertaken by my colleague, Burhan Saifaddin. Without this process any UV effort on SiC would be pointless. The final step after growth of the epitaxial layers is to process them into LEDS. For the deep UV project, a flip chip process will be undertaken on the epi grown on c-plane SiC substrates. Fig. 6.7shows the epi structure before and after the flip chip process. The initial SiC substrate is removed via chemical mechanical polishing and a Bosch-like etch, i.e. inductively coupled plasma(ICP) using SF_6. Al/Ni/Au will then be deposited on the thin p++ layer to protect the surface, and mesa etching is performed on the n-AlGaN. The N-face will be roughened in KOH to increase light extraction. The LED will then be wafer bonded to an insulative SiC substrate, and a thin layer of insulative SiO_2 will be deposited between it and the p-metal mirror. For more detailed information please refer to Burhan Saifaddin's papers and thesis.

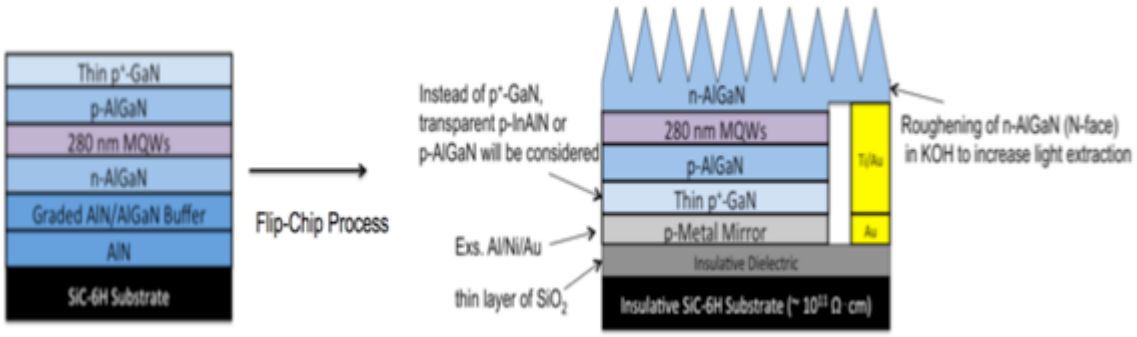

Fig. 6.7 Flip Chip Process for UV-C LEDs using Bosch-like Etch developed by Burhan Saifaddin.

6.3 Conclusions

In this chapter we introduced the MOCVD reactors that were used for the UV project. The vertical single load Veeco P-75 Turbodisc was initially the main reactor, however in 2016 UCSB upgraded to a Taiyo Nippon Sanso SR4000HT which could grow at low pressures like the Veeco, however had the capability of growing the AlN layer at 1300°C and has a trilayer gas injection nozzle to reduce parasitic pre reactions which will be discussed in detail in the next chapter.

The substrates available for the project were also introduced. Though sapphire is the most popular and AlN is the most ideal, SiC was chosen for its similarities to AlN. The SiC removal process is crucial to the success of the deep UV project and is done by Burhan Saifaddin. UCSB will attempt this foreign substrate approach before looking into AlN substrates.

6.4 References

[1] http://www.structuredmaterials.com/pdfs/modeling.paper.pdf

[2] C.B. Cooper III, M.J. Ludowise, V. Aebi, R.L. Moon, J. Electron. Mater **9**, 299 1980

[3] T. Arai, J. Hidaka, H. Tokunaga, K. Matsumoto, J. of Cryst. Growth, **170**, 88 (1997)

[4] K. Uchida, H. Tokunaga, Y. Inaishi, N. Akutsu, K. Matsumoto, Mat. Res. Society, **449**, 129 (1997)

[5] K. Matsumoto, T. Arai, H. Tokunaga, Vacuum, **51**, 699 (1998)

[6] J. P. Zhang, M. A. Khan, W. H. Sun, H. M. Wang, C. Q. Chen, Q. Fareed, E. Kuokstis, J. W. Yang, Appl. Phys. Lett. **81**, 4392 (2002)

[7] C.Moe, UCSB Dissertation Thesis, Growth and Fabrication of Deep Ultraviolet Light Emitting Diodes on Silicon Carbide Substrates, (2007)

[8] Y. Taniyasu, M. Kasu, N. Kobayashi, Appl. Phys. Lett. **81**, 1255 (2002).

[9] S. Keller, P. Cantu, C. Moe, Y. Wu, S. Keller, U. K. Mishra, J. S. Speck, S. P. DenBaars, Jpn. J. Appl. Phys. **44**, 7227 (2005).

[10] F. Nakamura, S. Hashimoto, M. Hara, S. Imanaga, M. Ikeda, H. Kawai, J. Cryst. Growth **195**, 280 (1998)

Chapter 7: Growth of AlN

In this chapter we will discuss the two efforts to grow AlN for the UV project at UCSB. The first effort was on the Veeco P-75 Turbodisc reactor. It was the primary reactor for UV since it was the only low-pressure reactor at UCSB. However, we were quick to discover that this would not be a sustainable method to grow high Al content AlGaN/ AlN due to parasitic pre reactions and low growth rates and efficiency. After some time, UCSB purchased the SR4000HT from Taiyo Nipon Sanso, which was a signiicant upgrade from the Veeco for reasons that we will explain in this chapter. Primarily, we could grow at higher temperatures, and the reactor geometry was specifically designed to reduced prereactions.

7.1 Source Efficiency of AlN on Veeco P-75 Turbodisc

7.1.1 Initial AlN growths

To start off and get an idea of the condition of the reactor, a temperature series and V/III series of AlN on SiC were investigated. The precursors used were TMAl and NH_3 with H_2 and N_2 as carrier gasses.

Fig. 7.1 plots the growth rate and growth efficiency as a function of the growth temperature. Growth efficiency is defined as the growth rate divided by the group III molar flow rate. A growth temperature regime from 1000 °C to 1150 °C was investigated, where the temperature was controlled by varying the current set point of the heating filament in the reactor. The three growths performed had current set points of 81 amps, 84 amps, and 87 amps, with a growth temperature of 1069 °C, 1105 °C, and 1134

°C, respectively. From Fig. 7.1, it is noted that a decrease in growth rate and efficiency was observed.

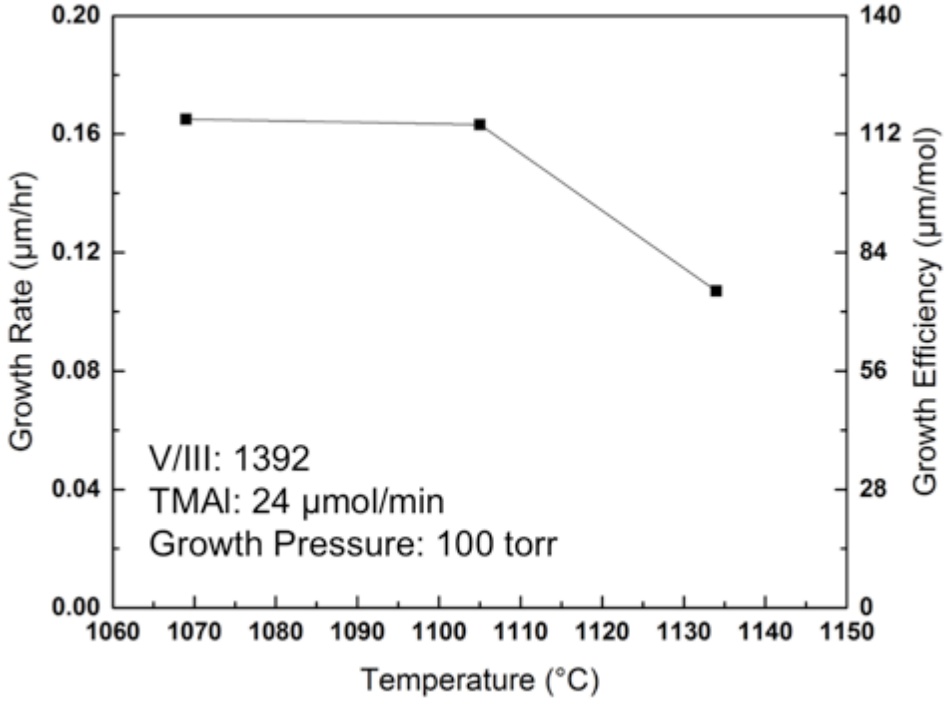

Fig. 7.1 Dependence of growth rate and the growth efficiency on temperature of AlN growth on SiC.

The second growth study investigated the variation in the V/III ratio (NH_3 to TMAl) from 88 to 1276. Fig. 7.2 plots the dependence of growth rate and growth efficiency on the V/III ratio. The flow rate of NH_3 was varied while TMAl was held constant at 26.2 µmol/min. The growth time was 60 minutes and the temperature was held constant at 1130°C with a current set point of 87 amps. The V/III ratios investigated were 1276, 638, 318, and 88, with NH_3 flow rates of 750, 375, 187, and 100 sccm, respectively. The studies indicated that increasing the V/III improved the surface quality and morphology due to increased amount of material reaching the susceptor. However,

the interactions between NH_3 and TMAl in the gas phase before reaching the susceptor also increased, which decreases the growth rate and covers the reactor wall in metalorganic (MO) source.

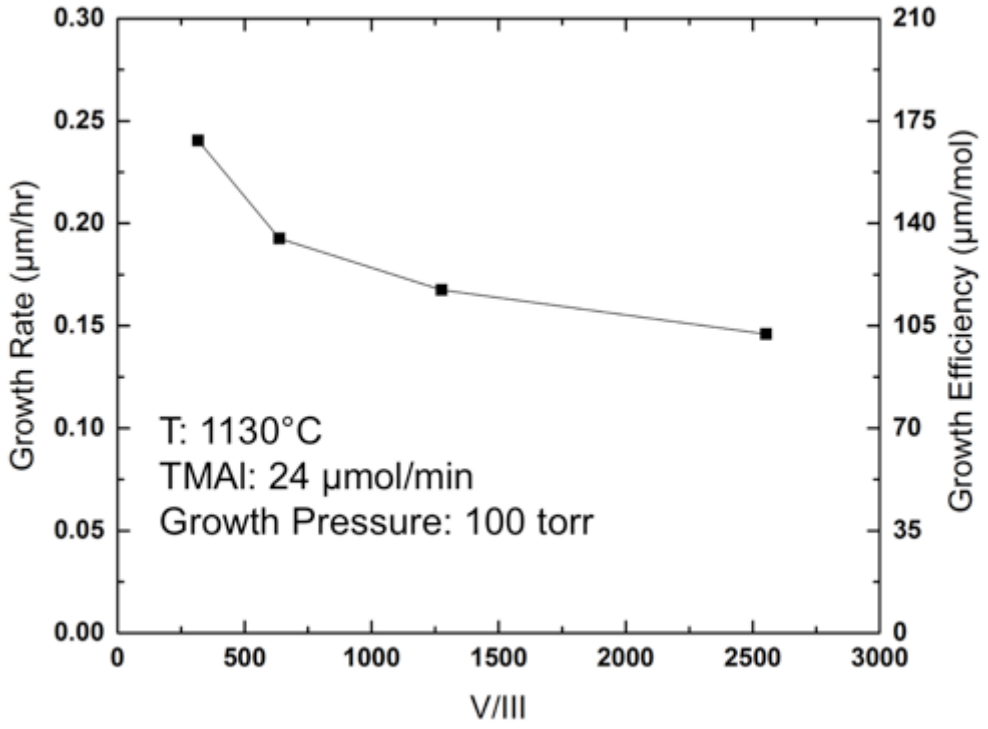

Fig. 7.2 Growth rate and growth efficiency as a function of V/III ratio

The max growth efficiency for the temperature series was 116 μm/mol and 166 μm/mol for the V/III series. These two results are remarkably low. A "good" value is considered to be ~1,000 μm/mol, so one can note that this reactor is not operating at it's optimal source efficiency. The task of growing uniform, high-quality AlN layers is complicated by the interaction of the group III trimethylaluminum (TMAl), and group V ammonia (NH_3) precursors in the gas phase, leading to adduct formation [1-7]. These adducts have the potential to undergo elimination reactions to produce volatile polymers

upstream of the susceptor and exacerbate parasitic source consumption during crystal growth [8-11]. As these interactions occur in the gas phase, they suppress the growth rates and lead to inefficient precursor usage [12]. Instead of contributing to the growing crystal, a white powder is deposited on the reactor walls of the growth chamber [13].

A parameter to quantify these pre-reactions is growth efficiency, which is defined as the growth rate divided by the group III molar flow rate [14]. Studies have reported that decreasing the reactor pressure, growth temperature, and V/III ratio can significantly reduce pre-reactions, thereby improving the growth rate and growth efficiency [15-20]. Though AlN has been demonstrated at low V/III ratios (10-100), impurity uptake increase as the V/III ratio is decreased, since carbon and oxygen compete with nitrogen for the group V lattice site [21]. Additionally, pulsed flow methods have shown improved growth rates for both vertical and horizontal reactors [22-24]. In this section, precursor dilution is investigated to reduce parasitic pre-reaction and improve the growth efficiency of AlN.

7.1.2 Precursor Dilution Methods

The growth chamber pressure, and temperature were held constant at 100 torr and 1130 °C, respectively. In following experiments, the total molar flow of TMAl was fixed at 24 μmol/min and the NH_3 partial pressure was held constant at ~15 torr. The V/III ratio was kept above 1000, since previous work has shown that large V/III ratios yield superior AlN quality with much narrower full width at half maximum (FWHM) of x-ray rocking curves (omega scan) for (0002) and $(20\bar{2}1)$ reflections [21, 25]. The spindle rotation rate was 1300 rpm to generate a thin and uniform boundary layer, and to prevent

gas recirculation. The growth chamber is designed in such a way that group III precursors, NH_3, and carrier gasses are supplied via separate channels (Fig. 7.3).

In this study, two TMAl precursor dilution methods were explored to reduce pre-reactions. In Method A, the total gas flow (including the NH_3 flow) into the growth chamber was increased via the carrier gas and NH_3 channels in Fig. 7.3. Fig. 7.3(a) demonstrates the gas lines (bold red lines), used for the incremental increase of H_2, N_2, and NH_3 injected into the growth chamber, while holding the dilution flow through the Alkyl channels constant at 1.56 slm. Given that the total flow was increased by 3.4 slm, the NH_3 flow was also increased to maintain a fixed NH_3 partial pressure. In Method B, the dilution flow (N_2) in the Alkyl channels used for group III precursor injection was increased. The carrier gas flow and NH_3 flow through the carrier gas and NH_3 channels were held constant at 8.5 slm. Given that small change in total flow (1.3 slm) relative to Method A, it is not necessary to change the NH_3 to maintain a constant NH_3 partial pressure. Fig. 7.3(b) shows the gas line used for the increase of the dilution flow (N_2) through the Alkyl channels. The bold blue lines represent the N_2 gas lines providing TMAl dilution prior to entering the growth chamber.

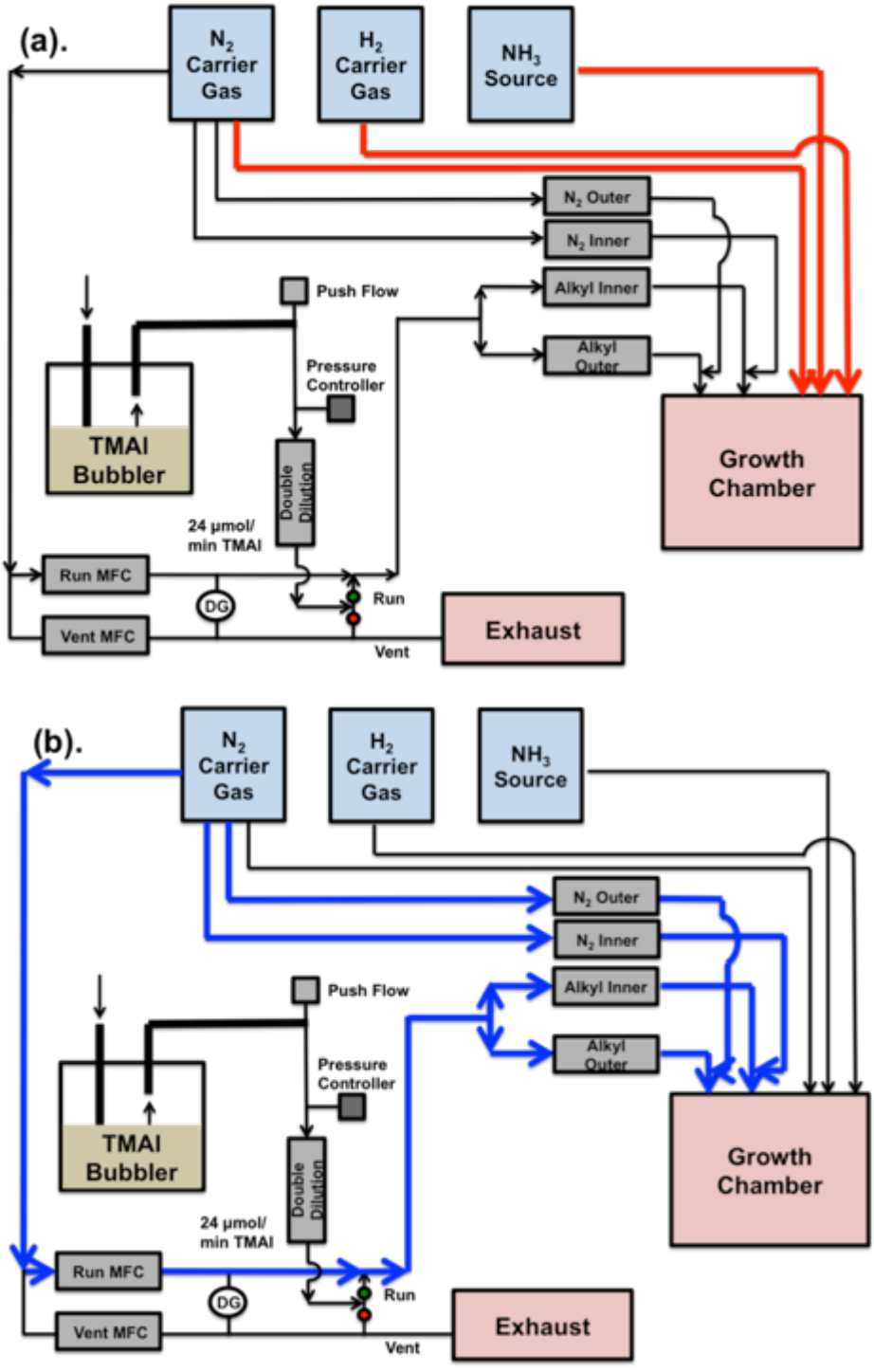

Fig. 7.3 Schematic of the MOCVD reactor and corresponding gas lines. **(a)** Method A: The carrier gas and NH_3 channels (bolded in red) used for the increase of H_2, N_2, and NH_3 directly into the growth chamber, while holding the Alkyl channels constant **(b)** Method B: Gas lines used for the carrier gas increase through the Alkyl channels for group III precursor injection (blue), while holding the carrier gas through the carrier gas channels constant.

The film thickness was measured using a Filmetrics F20 thin film measurement system, which determines the film thickness by measuring the intensity of light reflected from the thin film over a range of wavelengths then comparing it to a calculated reflectance spectrum for the material of interest. The samples were then cross-sectioned and gold coated to verify the film thickness using an FEI XL30 30 kV scanning electron microscope.

A Panalytical X'Pert Materials Research Diffractometer was used to investigate the FWHM of x-ray rocking curve (omega scan) for the (0002), and $(10\bar{1}2)$, reflections, using an open detector in a double axis configuration with a four-bounce monochromator in the incident beam. The $(10\bar{1}2)$ orientation used a skew symmetric orientation.

7.1.3 Results for Improving Efficiency

The dependence of the growth rate and growth efficiency on the total gas flow are shown in Fig. 7.4 using Method A and Method B. The growth rate is on the left axis of ordinates, and the growth efficiency, which is linearly proportional to growth rate, is plotted on the right axis of ordinates for both methods. In an ideal case, both methods should have the same outcome, as increasing the total gas flow leads to a reduction in the TMAl partial pressure, reducing the growth rate, as demonstrated using Method A, when the gas flow into the growth chamber was increased via the carrier gas and NH_3 channels. The results depicted in Fig. 2 show that using this injection scheme, the growth rate and efficiency decreased from 0.31 μm/hr to 0.13 μm/hr and 218 μm/mol to 92 μm/mol, respectively.

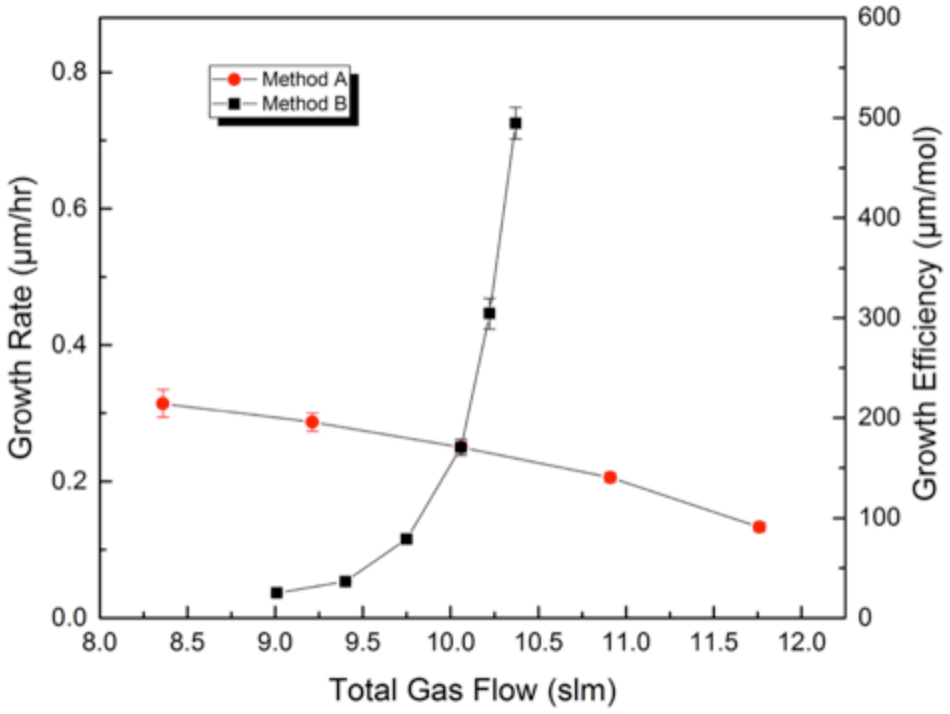

Fig. 7.4 The dependence of the growth rate and growth efficiency on the dilution method. In Method A, the total gas flow (including NH_3) into the growth chamber was increased via the carrier gas and NH_3 channels. In Method B, the dilution flow (N_2) in the Alkyl channels used for group III precursor injection was increased.

However, increasing the carrier gas flow via the dilution flow in the Alkyl channels exhibited a very different behavior. In contrast to the results obtained in Method A, Method B demonstrated a marked increase in the growth rate and growth efficiency. Fig. 2 demonstrates that when using Method B, an 18-fold increase in growth rate from 0.04 μm/hr to 0.73 μm/hr occurred, while the growth efficiency also increased from 26 μm/mol to 502 μm/mol. The MFCs were increased to their maximum values before the growth rate and efficiency could saturate.

Furthermore, the utilization of the injected precursor molecules was evaluated by determining the ratio of number of moles of Al in the film to the number of moles of

TMAl entering the growth chamber in a given time period. This metric assumed a 60-minute growth time under a constant molar flow of 24 μmol/min (1440 μmoles TMAl) on a SiC substrate with a 5.08 cm diameter. The efficiency improved from 0.003 to 0.068, when the flow of N_2 through the Alkyl channels increased. Therefore under the most efficient growth parameters using Method B, 6.8 % of Al atoms from the injected TMAl were utilized for AlN layer growth. For comparison, 6.02% of Ga atoms from the injected TMGa were used for the standard GaN growth using the same reactor configuration. Thus, for our reactor configuration, we have achieved similar growth efficiency for TMAl as TMGa.

In Method A, there was a significantly larger change in the total flow into the reactor, compared to Method B. In Method A, the carrier gas dilution increased by a total of 3.4 slm. This large change in overall total gas flowing directly into the growth chamber via the carrier gas channels reduced the amount of time that the precursors resided in the hot zone, which can reduce pre-reactions. However, if gas phase reactions do not play a role or are unaffected, the increase in gas flow leads to a reduction in the boundary layer thickness and decreases the TMAl partial pressure, which by itself would result in a growth rate reduction, as discussed above.

In Method B, there was much less change in total flow, as the group III dilution flow was increased by only 1.3 slm. In this case, contrary to Method A, growth rate and efficiency significantly improved. Increasing the dilution flow (N_2) in the Alkyl channels used for group III precursor injection lowered the concentration of reactant in the gas phase, thereby suppressing pre-reactions. However, contrary to Method A, the pre-reaction suppression dominates over reactant dilution, resulting in improved growth rate

and higher Al source efficiency. Diluting the TMAl precursor flow prior to entering the growth chamber (through the Alkyl channels) rather than inside the growth chamber (through carrier gas channel) led to a significant reduction in pre-reactions and more Al species reached the substrate surface. This also led to reduced reactor wall deposits, noted by visual inspection of the reactor wall during maintenance. The stark contrast between the two methods used to increase the total carrier gas flow illustrates the impact of specific reactor design components on the chemical reactions in the gas phase above the wafer and their impact on the crystal growth process.

The FWHM of the (0002) and ($10\bar{1}2$) omega scans as a function of thickness/growth rate are illustrated in Fig. 7.5 for the AlN thin films grown using Method B. The growth time was 1 hour for all samples. A reduction in the FWHM of the omega scans is observed as the film thickness increased with increasing thickness as previously observed by Bauer *et* al [26]. The annihilation of dislocations observed by the reduction in the FWHM over large thicknesses emphasizes the need to grow thick AlN buffer layers for optical device, while flowing precursor in an efficient manner. The thickest AlN film (0.73 μm) with the highest efficiency (502 μm/mol) had (0002) and ($10\bar{1}2$) FWHM values of 82 and 704 arc seconds, respectively.

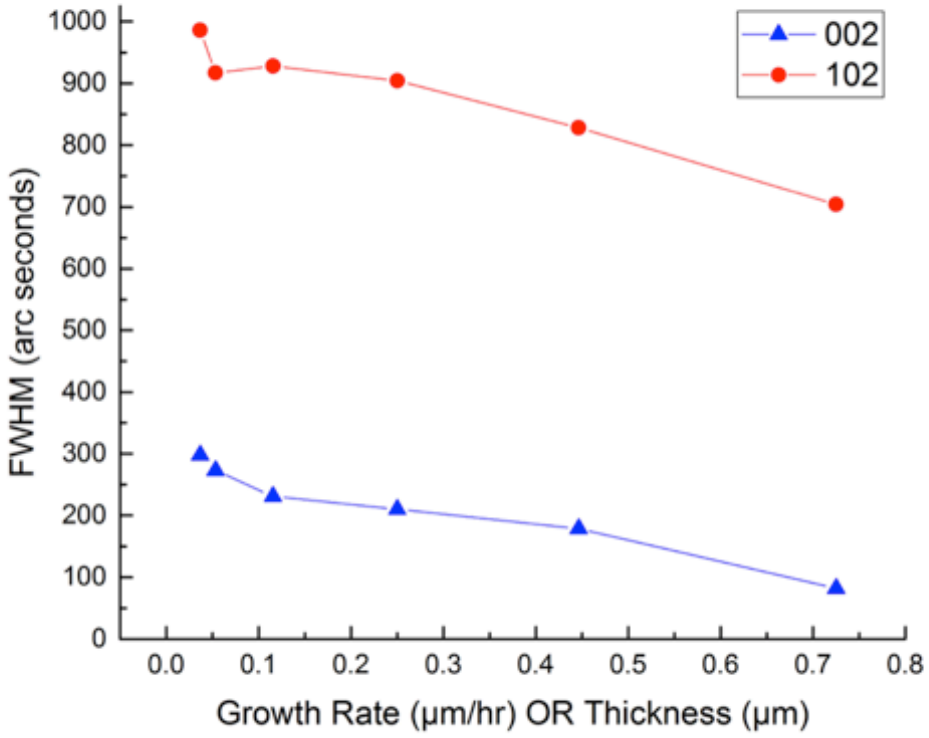

Fig. 7.5 FWHM of (0002) and (102) omega scan reflections as a function of growth rate or thickness.

7.2 AlN on the TNSC SR4000HT

After realizing that a high efficiency UV LED would not be feasible on the P-75 Turbodisc MOCVD, primarily because of the temperature constraints and poor growth efficiency compared to other more robust reactors in the MOCVD laboratory, the TNSC SR4000HT was acquired. This was a grand undertaking in terms of growth, primarily because all recipes would have to be started essentially form scratch and would require much optimization. In this section we will discuss in detail the growth of AlN and defect reduction mechanisms, which were utilized to grow high quality AlN on SiC.

7.2.1 Single Layer AlN

Initial growths of AlN consisted of a single layer of AlN atop a thin AlN nucleation layer (50-100 nm) on a 250 µm SiC substrate. The first investigation was finding an optimal thickness for the buffer layer. Fig. 7.6 plots the on- and off-axis rocking curve FWHM as a function of the AlN buffer layer thickness. As the buffer layer was grown thicker, the off-axis rocking curve FWHM values decreased, and the on-axis values remained roughly the same. At 1 micron the on- and off-axis FWHM was 300 and 590 arc seconds, respectively. The thicknesses investigated were 300, 400, 750, and 1000 nm.

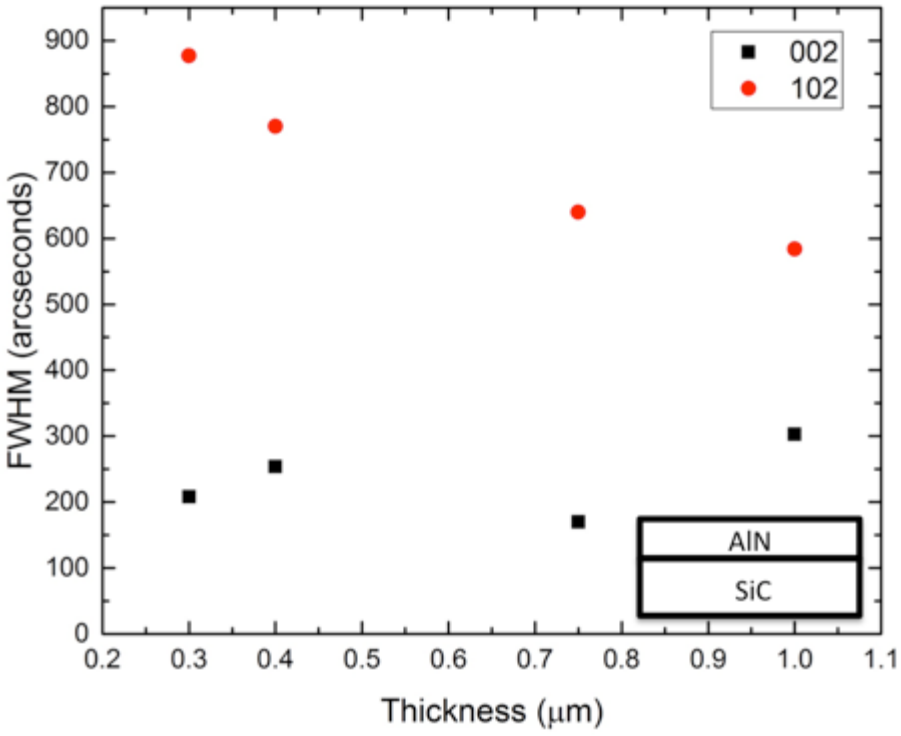

Fig. 7.6 Rocking Curve FWHM as a function of Single Layer AlN Thickness

However as the thickness increased, the AlN began to develop deep cracks propagating through the epitaxial structure and developing large ridges where cracks had overgrown, as seen in Fig 7.7, which shows AFM height retrace scans for the thicknesses investigated in this study, 300, 400, 750, and 1000 nm. After 400 nm, which displays smooth step flow morphology, the AlN layer at 750 nm and 1000 nm had large cracks and overgrown ridges where cracks had formed on the surface. This was obviously detrimental to the device structure and was to be avoided. The AFM scans are representative of the sample meaning that these cracks are seen throughout the sample surface, including the center of the epi, not just the edges, where cracking is common and acceptable. At 300 nm, the AlN takes the form of the underlying SiC substrate; as the SiC's scratch marks from polishing are visible on the height retrace scan. This is not detrimental to the overall device structure and is not a current leakage pathway, like a crack would be.

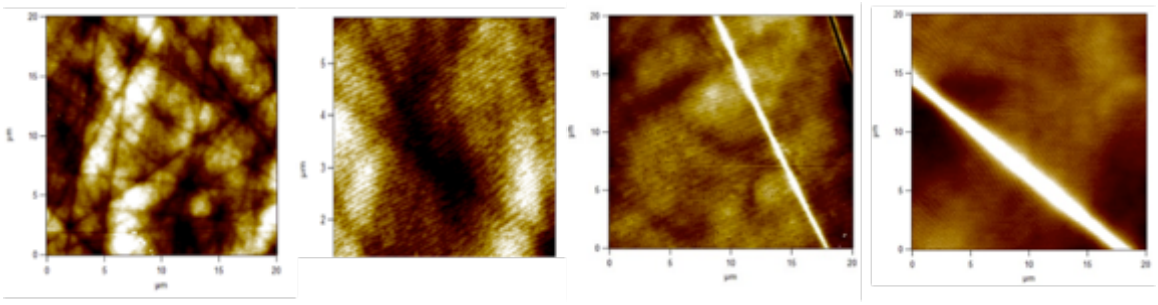

Fig. 7.7 AFM height retrace of AlN on SiC at 300, 400, 750, and 1000 nm, respectively. At 300 nm the polishing marks from the SiC are still visible. With increased thickness, cracks begin to appear.

The on- and off-axis FWHM give an indication of the dislocation density in the sample, however the most accurate way to determine the density of dislocations (screw,

edge, or mix) is with plan view transmission electron microscopy. This method will be discussed in detail in the following section. The 300 nm sample was further investigated with TEM to determine the dislocation density and is seen in Fig. 7.8, along with a calculated dislocation density of 1 x 10^{10} cm^{-2}. From Kneissl *et al*, this puts the projected I.Q.E. of a 280nm device at just under 5%, with this dislocation density. Obviously, this is not an acceptable metric and much works needs to be undertaken to reduce the dislocation density for the sake of future devices even lighting up. The following section will discuss a method by which the dislocation density is reduced.

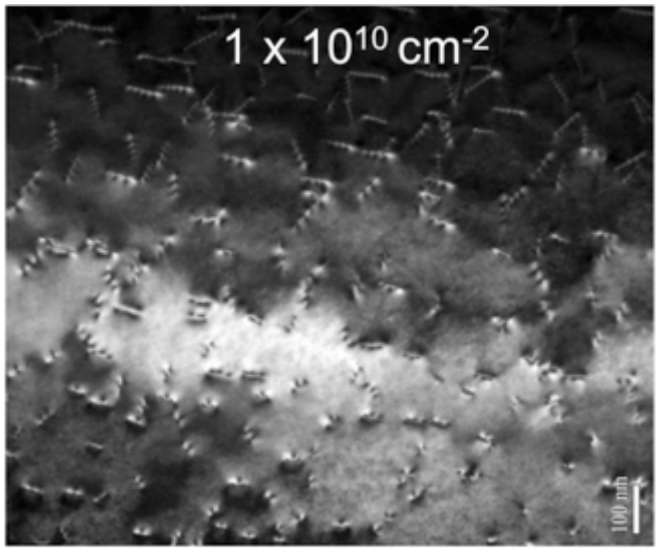

Fig. 7.8 Plan-View TEM of Single Layer AlN

7.2.2 Modulated Growth of AlN

In MOCVD, TDs originate from the growth mechanism of AlN on SiC. During the initial (nucleation) stage of growth, there is a high density of three-dimensional (3D) AlN islands nucleating on the SiC surface. Taniyasu *et al* reports that these islands twist around each other, generating a high density of edge dislocations at the grain boundaries

during island coalescence. After coalescence, the side facets of the 3D islands expand laterally, leading to the inclination and bending of TD such that they annihilate with each other. Taniyasu *et al* further states that increasing the 3D island size and further enhancing lateral growth can further reduce the TDD. Following these initial stages of 3D growth, AlN then grows in the two dimensional (2D) mode and edge dislocations propagate along the [0001] growth direction [27,28].

A technique to improve the crystal quality and reduce the dislocation density of AlN is to use high temperatures (HT) growths to aid the surface mobility of Al atoms and increase the diffusion length. Another method is to include a reduced temperature (RT) buffer layer/interlayer [29,30].

In 2008 Chen *et al* used a multilayered AlN structure, alternating between the 2D and 3D growth mode to grow high quality AlN on SiC by metalorganic chemical vapor deposition (MOCVD). This method was termed modulated growth. Chen *et al* were able to achieve (002) and (102) x-ray rocking curve full width half max (FWHM) of 86 and 363 arcsec, respectively. The result is tabulated in Table 7.1, which also includes other works by groups who used similar techniques, such as an intermediate temperature interlayer or multilayered structure, to reduce the dislocation density of AlN on foreign substrates [31-37]. The typical interlayer temperature was between 800-1100 °C, the interlayer thickness varied from 25-300 nm, with 3 interlayers. All groups grew the multilayered AlN by MOCVD with the exception of Chen *et al* (2010), which used molecular beam epitaxy (MBE).

Table 7.1: Literature results for x-ray rocking curve FWHM and threading dislocation density for multilayered AlN on foreign substrates

Group	(002) arcsec	(102) arcsec	Threading Dislocation Density (cm^{-2})	Substrate
Chen *et al* 2008	86	363	N/A	SiC
Chen *et al* 2010	110	900	6×10^{9} cm^{-2}	Sapphire
Kitagawa *et al* 2014	241	448	3.9×10^{8} cm^{-2}	SiC
Li *et al* 2015	349	659	1.25×10^{9} cm^{-2}	Sapphire
Chen *et al* 2015	35	575	1.85×10^{9} cm^{-2}	Sapphire
Zhang *et al* 2015	311	548	N/A	Sapphire
Guo *et al* 2017	100	400	N/A	Sapphire

One can note that the majority of the reported dislocation densities in Table 7.1 are in the low to mid x 10^{9} cm^{-2}. Kneissl *et al* (2011) reported that these dislocation densities act as areas of non-radiative recombination, leading to an IQE of around ~10-30% for the AlGaN multi-quantum wells (MQWs) in UV emitters [38,39]. This simulated work does not take into account other non-radiative recombination pathways, however does elucidate how important it is to reduce the TDD.

In this work, Chen *et al*'s (2008) modulated growth AlN structure is emulated, with the effort of further reducing the TDD. We will demonstrate how varying the interlayer growth temperature of the AlN film can reduce the (102) rocking curve FWHM via x-ray diffraction (XRD) and the edge dislocation density verified by transmission electron microscopy (TEM), all while maintaining smooth step flow morphology characterized by atomic force microscopy (AFM).

7.2.2.a Experimental Layout for Dislocation Reduction using Modulated Growth

A schematic of the growth structure is shown in Fig. 7.9. The HT layers' growth temperature and V/III ratio were 1250°C and 166, respectively. The RT interlayers' V/III

ratio was 1068 and the growth temperature was varied from 1200, 1100, 1080, 1000, 900, to 800°C. The growth chamber pressure for the HT and RT interlayers were 100 and 300 torr, respectively. The growth rate for the HT and RT interlayer were 10 and 1.5 A/s, respectively. The total thickness of the structure was 2.5 μm..

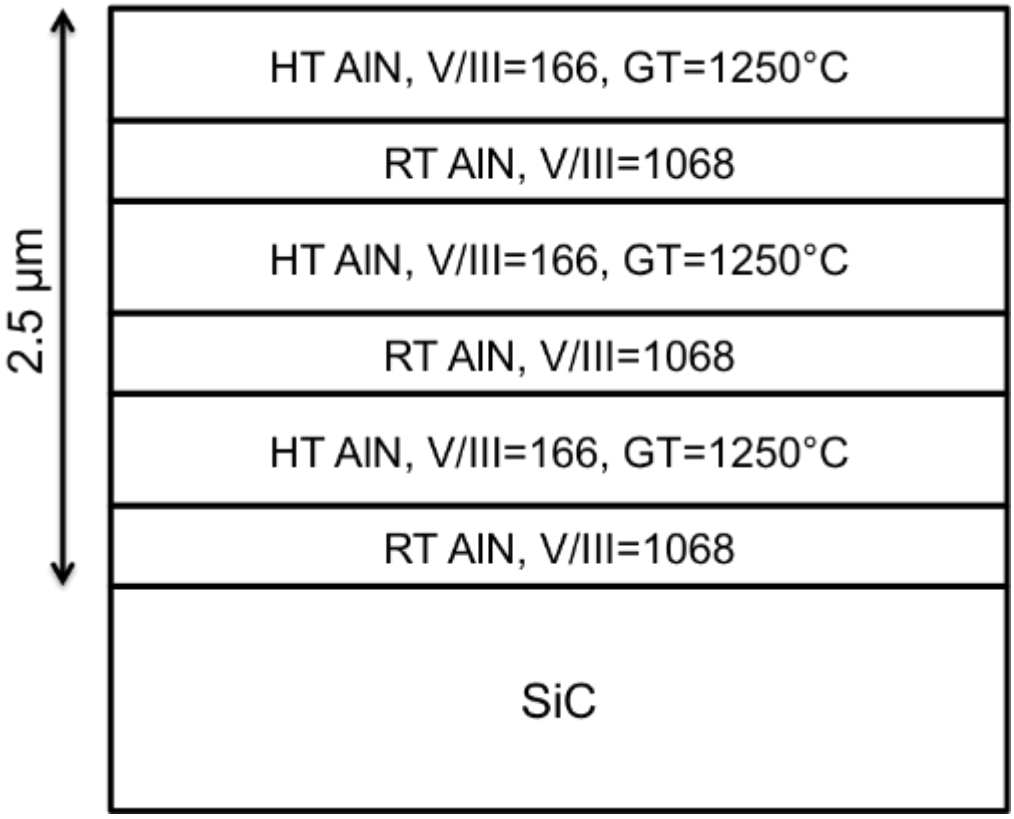

Figure 7.9. Schematic of RT/HT AlN Structure.

A Panalytical X'Pert Materials Research Diffractometer (MRD) was used to measure the x-ray rocking curve (omega scan) for the (0002) and $(10\bar{1}2)$ reflections, using an open detector in a double axis configuration with a four-bounce monochromator in the incident beam. The $(10\bar{1}2)$ orientation used a skew symmetric orientation.

An Asylum Research MFP3D atomic force microscope was used to investigate the surface morphology of the AlN layers qualitatively by verifying terraced atomic structures on the HT layer and surface. The RT interlayer was also scanned to see the change in morphology with decreasing growth temperature. The root mean squared (RMS) roughness was then recorded to quantify the roughness of the surface of interest.

The plan-view and cross-section TEM samples were prepared using a FEI Helios Dualbeam Nanolab 650 focus ion beam (FIB) system. The TEM images were recorded with an FEI Tecnai G2 Sphera Microscope w/ EDS System operated at 200 kV.

7.2.2b Determining Dislocation Density in Modulated Growth of AlN

Figure 7.10 displays the dependence of the (002) and (102) x-ray rocking curve FWHM on the RT interlayer growth temperature, while holding the HT layer growth temperature constant at 1250 °C. Note that as the temperature is decreased from 1200 °C to 1000 °C the (102) FWHM decreased from 587 to 250 arcsec. Then at 900 °C, the (102) FWHM increased up to 491 arcsec. The on-axis (002) FWHM decreased to 70 arcsec as the growth temperature decreased to 1000 °C. However, at 900 °C the (002) FWHM increased to 271 arcsec. The FWHM for the on- and off-axis scan at the RT interlayer growth temperature of 800 °C was not measurable, presumably due to poor crystallinity of the RT interlayer.

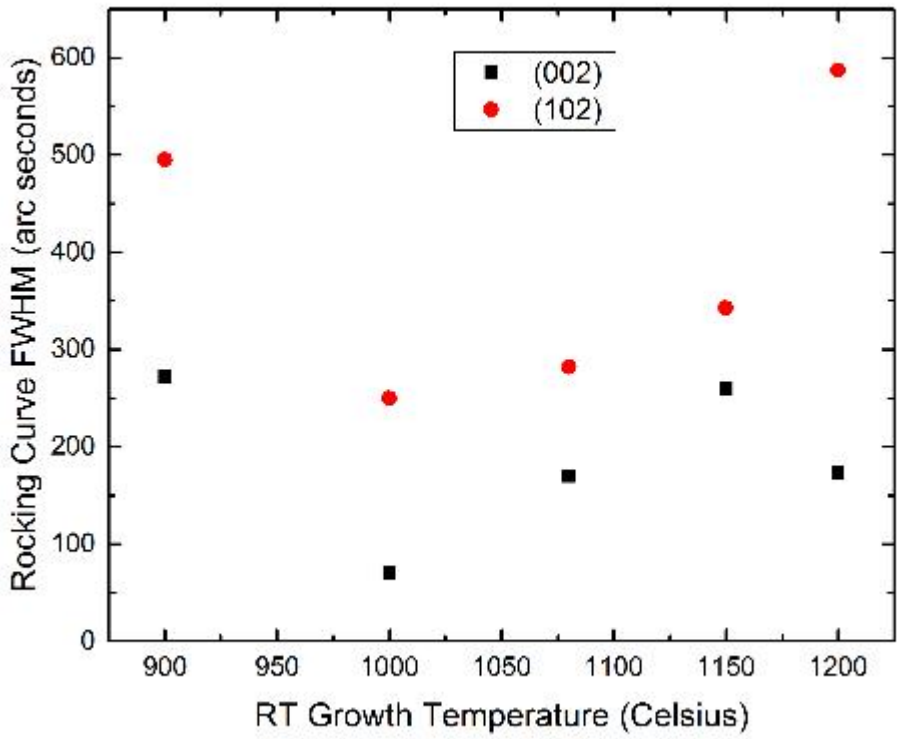

Figure 7.10. (0002) and $(10\bar{1}2)$ Rocking Curve FWHM as a function of RT interlayer growth temperature.

To investigate how reducing the RT interlayer growth temperature impacted the surface morphology, a separate structure was grown that included just one RT interlayer. Figure 7.11 displays a schematic of the alternative structure.

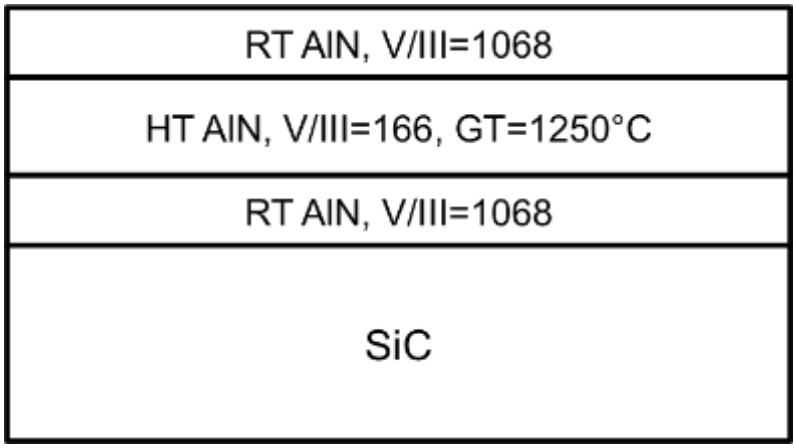

Figure 7.11. Schematic of HT/RT AlN Structure for RT Morphology Verification.

Figure 7.12 displays the 5 μm x 5 μm AFM height retrace scans for the structure in Fig. 7.11 while varying the RT interlayer growth temperature. It is clear that as the growth temperature decreased, the surface morphology deviated from step flow growth to more three dimensional growth features, most specifically at 1000 °C. The RMS roughness also increased as the temperature decreased. At 900 °C, pits formed at the surface (RMS roughness of 4.73 nm) and at 800 °C there was no evidence of a specular smooth surface, with a RMS roughness of 129 nm.

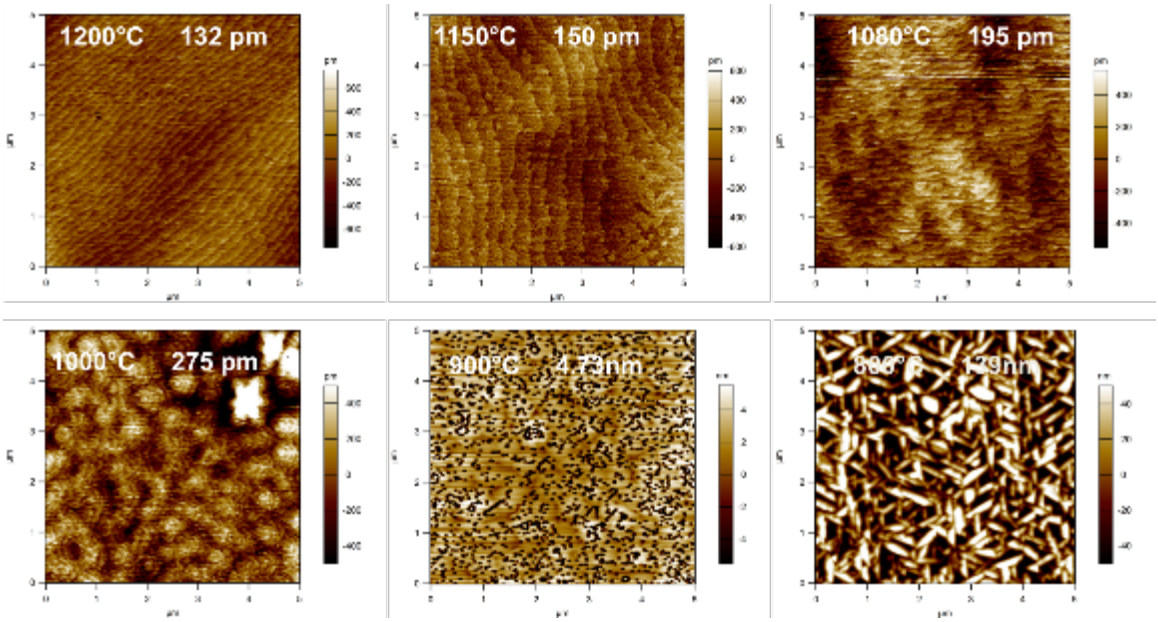

Figure 7.12. 5 µm x 5 µm AFM images displaying RT interlayer surface morphology. RT growth temperature and RMS roughness ranging from (top left) 1200 °C and 132 pm, (top center) 1150 °C and 150 pm, (top right) 1080 °C and 195 pm, (lower left) 1000 °C and 275 pm, (lower center) 900 °C and 4.73 nm, (lower right) 800 °C and 129 nm.

Figure 7.13 displays the 20 µm x 20 µm AFM height retrace scans for the surface of the full structure (Fig.7.9) for varying RT interlayer growth temperatures. Areas representative of the sample surface were selected. Cracks were visible at the edges using an optical microscope (not shown), however were not present at the center of the sample. From 1200 °C to 1000 °C the films exhibited a smooth step flow morphology, with the steps in the a-direction. At 900 °C, the film surface began to exhibit pits and surface defects, and then at 800 °C the sample surface roughened and no longer demonstrated step flow morphology.

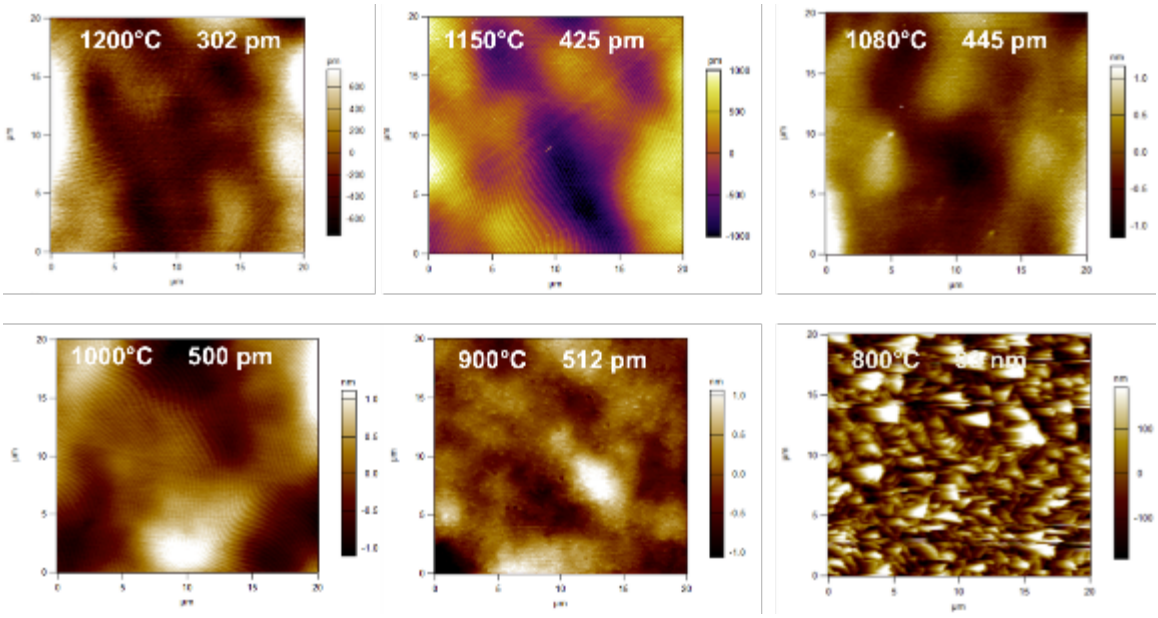

Figure 7.13. 20 μm x 20 μm AFM images displaying morphology for surface of full structure for different RT growth temperatures. RT growth temperature and RMS roughness ranging from (top left) 1200 °C and 302 pm, (top center) 1150 °C and 425 pm, (top right) 1080 °C 445 pm, (lower left) 1000 °C and 500 pm, (lower center) 900 °C and 512 pm, (lower right) 800 °C and 93 nm.

Heying *et al* (1996) reports that the (102) reflection is a more reliable indicator of structural quality; therefore it would be of interest to further analyze the microstructure of the AlN layers that show a trend of decreasing (102) x-ray rocking curve peak width [40] with TEM. The structures corresponding to the 1200, 1150, and 1000°C RT growth temperatures were investigated. Using the invisibility criterion $\mathbf{g}\cdot\mathbf{b} = 0$, the dislocation type can be identified, where $\mathbf{g} = 11\bar{2}0$ was used to make edge threading dislocations visible. Figure 7.14 displays dark field plan view (PV) TEM images under weak beam conditions for $\mathbf{g} = 11\bar{2}0$. From the plan view TEM images, the edge dislocation density can be determined. The reported edge dislocation density for the 1200 °C, 1150 °C, and 1000 °C RT growth temperatures was 8x 10^9 cm^{-2}, 3 x 10^9 cm^{-2}, and 7 x 10^8 cm^{-2}, respectively. The screw dislocation density for these structures was less than 10^7 cm^{-2}.

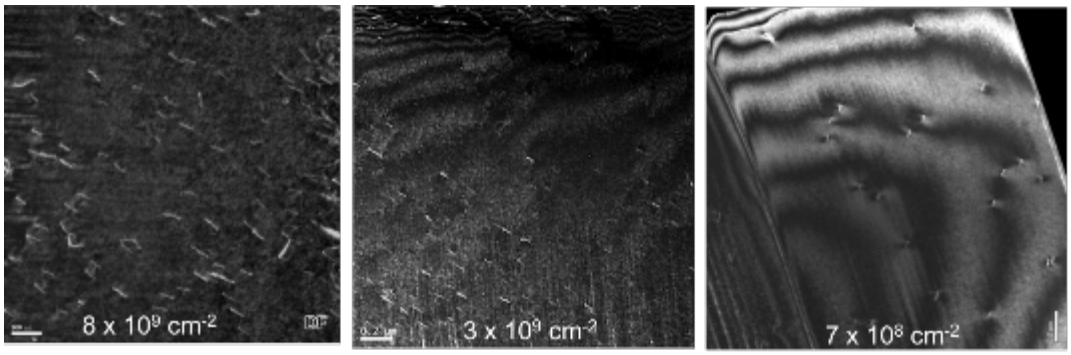

Figure 7.14. Reduction in Dislocation Density in AlN via Plan View Dark Field <1$\bar{1}$20> TEM Image.

Figure 7.15 displays the cross section TEM images of the multiple RT interlayer structure with a RT interlayer growth temperature of 1000 °C. The AlN with a RT interlayer growth temperature of 1000 °C was selected because it displayed the lowest on- and off-axis rocking curve FWHM from Fig. 7.10 and displayed the lowest recorded dislocation density via PV TEM from Fig.14. Figure 7.15a and 7.15b display two-beam dark field images in **g** = $\bar{1}100$ and **g** = 0002, around the [11-20] zone axis. The sample was then tilted 30° to the adjacent [01-10] zone axis, with **g** = $\bar{2}110$ (Fig. 7.15c). The bottom portion of the figures is a product of sample preparation. Using **g** = $\bar{1}100$ (Fig. 7.15a) it was verified that no stacking faults were present in the AlN and with **g** = 0002 (Fig. 7.15b), it was verified that the screw dislocation density was negligible (pure edge dislocations are not visible in **g** = 0002 diffraction condition). Fig. 7.15c shows a cross section image using **g** = $\bar{2}110$. This image displays how with a reduced interlayer growth temperature, the TD inclination increases and thus enhances TD-TD interactions. The TDD is decreased via fusion and annihilation reactions.

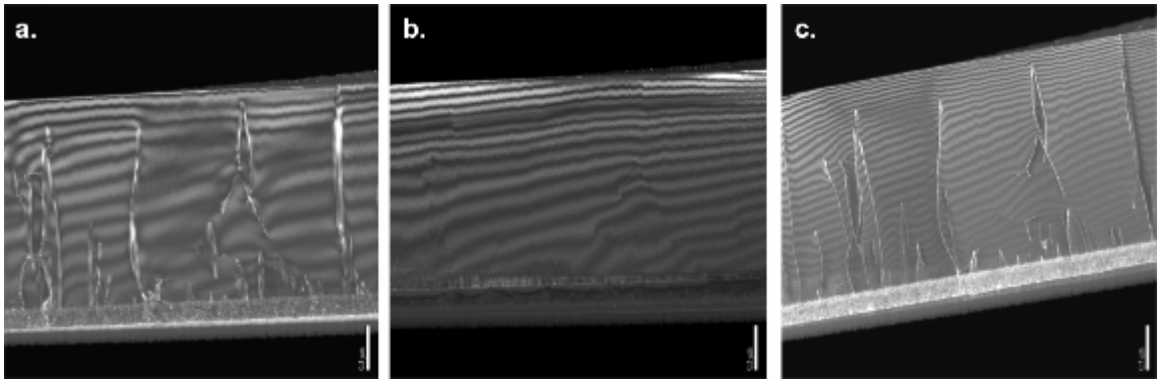

Figure 7.15. Cross section TEM of the RT/HT AlN with RT growth temperature at 1000°C. **a. g** = $\bar{1}100$, **b.** g=0002, and **c. g** = $\bar{2}110$. The bottom portion of the figure is a product of sample preparation. The waves present in the AlN layers are due to image contrast.

7.2.2c Analysis of Defect Reduction and Comparison Alongside Literature Values

The purpose of reducing the RT interlayer growth temperature was to increase the roughness of the interlayer by achieving the 3D growth mode. Enhancing the interlayer roughness promotes TD inclination, such that interactions between neighboring TDs occur. The mechanism of TD reduction is by TD-TD interaction, which leads to fusion and annihilation at the RT interlayers. It is evident from Fig. 7.12 that at a RT interlayer temperature of 1000 °C, the interlayer morphology shows distinct three dimensional features, while still maintaining smooth step flow morphology at the surface, as shown in Fig. 7.13. The reduction in (102) FWHM in Fig. 7.10 from 587 arcsec to 250 arcsec as the RT interlayer was decreased to 1000°C verifies the TDD reduction as does the PV TEM images from Fig. 7.14.

As the temperature was decreased from 1000 °C to 900 °C, the (102) x-ray rocking curve peak width in Fig. 7.10 increased from 250 arcsec to 491 arcsec. Additionally, for the RT interlayer growth temperature of 900 °C, the surface morphology in Fig. 7.13 and Fig. 7.14 began to develop pits and surface defects which

were not present in the previous high temperature images. As the RT interlayer growth temperature was further decreased to 800 °C, the surface morphology roughened and was no longer smooth and step flow. Additionally the rocking curve scans showed no peaks. At these temperatures, the mechanism of defect reduction was no longer dominant.

The TEM images in Fig. 7.14 recorded the reduction in dislocation density. At the lowest favorable RT growth temperature (1000 °C), the dislocation density was 7 x 10^8 cm^{-2}. At this dislocation density, the estimated threading dislocation-limited IQE from Kneissl *et al* would be approximately 60%, almost twice as high as the majority of Table 7.1 and a significant improvement from when the RT growth temperature was 1200 °C, where the dislocation density was 8 x 10^9 cm^{-2}, which corresponds to an estimated IQE of just ~5%.

Figure 7.16 displays the threading dislocation density reported in the literature alongside the ones reported in this work as a function of the (102) rocking curve FWHM. The solid data points indicate that the dislocation density was determined via TEM, i.e. this investigation (black squares), as well as Li *et al* (2015) and Chen *et al* (2010). The half filled data points indicate that the dislocation density was determined by other methods. The dislocation density in Chen *et al* (2015) was estimated by an equation taking into account the rocking curve FWHM values [41]. The edge dislocation density in Kitagawa *et al* (2014) was estimated via a selective etching technique and using a scanning electron microscope (SEM) [42].

Plan view TEM is the preferred method for determination of edge dislocation density in III-nitrides. Primarily because one can target the specific diffraction condition that makes the dislocation of interest visible. As described earlier, $\mathbf{g} = 11\bar{2}0$ is used to

make edge dislocations visible. Relying solely on rocking curve FWHM for dislocation determination can be misleading, as other mechanisms can lead to reduction in FWHM, such as thickness and mosaicity. Electron channeling contrast imaging (ECCI) is believed to be an accurate method to determine dislocations using SEM, however this method was not used in Kitagawa *et al*.

For the work presented in this manuscript it is evident that the dislocation density reported via TEM is correlated with the (102) FWHM, i.e. as the FWHM decreases, so does the threading dislocation density. At a RT growth temperature of 1000 °C, the AlN in this work reported the lowest (102) FWHM of 250 arcsec with a dislocation density of 7×10^{8} cm^{-2}.

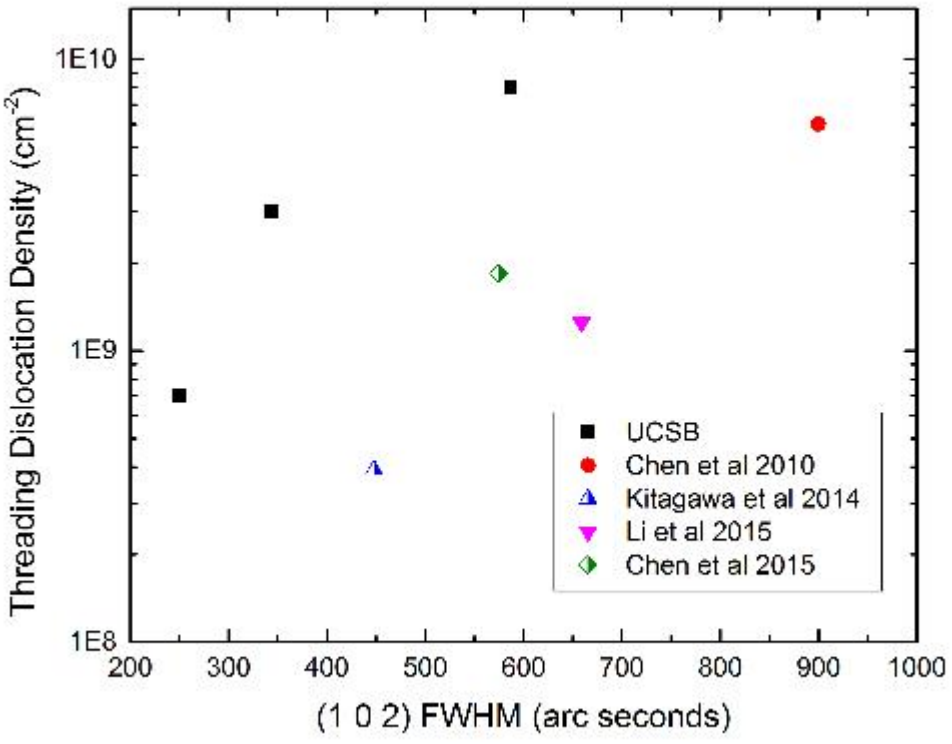

Figure 7.16. Threading Dislocation Density as a Function of $(10\bar{1}2)$ Rocking Curve FWHM.

7.3 Conclusions

Using the Veeco P-75 Turbodisc, two approaches to precursor dilution were investigated to improve the growth rate and efficiency of AlN thin film growth and eliminate parasitic pre-reactions via MOCVD. Increasing the carrier gas and NH_3 flowing through the carrier gas and NH_3 channels while holding the dilution flow through the Alkyl channels and TMAl molar flow constant did not affect the pre-reactions and the growth rate decreased with increasing precursor dilution. On the other hand, diluting the TMAl concentration via the Alkyl channels while holding the flow of carrier gas and NH_3 through the carrier gas and NH_3 channels constant resulted in a substantial increase in growth rate and marked improvement in the growth efficiency. The results show an 18x increase in growth rate and efficiency of AlN films and better efficiency of source utilization compared to GaN growths. As expected, the structural quality of the AlN films increased with increasing thickness as indicated by the reduction of the FWHMs of the (0002) and $(10\bar{1}2)$ x-ray diffraction peaks

Using the TNSC SR4000HT, Chen *et al*'s (2008) modulated technique for AlN was replicated with the goal of further reducing the threading dislocation density of AlN via MOCVD. The growth temperature of the RT interlayer was investigated to see the impact on improving the crystal quality. At 1000°C the (102) rocking curve FWHM was 250 arcsec and the dislocation density via TEM was 7×10^8 cm^{-2}. At this growth condition, the threading dislocations inclined and annihilated themselves, acting as an effective method for defect reduction.

References

[1] T.G. Mihopoulos, V. Gupta, K. F. Jensen, J. of Cryst. Growth **195**, 733 (1998)

[2] A. S. Lisovenko, K. Morokuma, A. Y. Timoshkin , J. Phys. Chem. A **119**, 744 (2015)

[3] A.V. Kondratyev, R.A. Talalaev, W.V. Lundin, A.V. Sakharov, A.V. Tsatsulnikov, E.E. Zavarin, A.V. Fomin, D.S. Sizov, J. Cryst. Growth **272**, 420 (2004)

[4] F. Nakamura, S. Hashimoto, M. Hara, S. Imanaga, M. Ikeda, H.Kawai, J. Crystal Growth **195**, 420 (1998)

[5] S. Kim, J. Seo, K. Lee, H. Lee, K. Park, Y. Kim, C.-S. Kim, J. of Cryst. Growth **245**, 247 (2002)

[6] J. Randall Creighton, G.T. Wang, W.G. Breiland, M.E. Coltrin, J. of Crystal Growth **261**, 204 (2004)

[7] S. Ruffenach-Clur, O. Briot, J.L. Rouviere, B. Gil, R.L. Aulombard, Mater. Sci. Eng. B **50**, 219 (1997)

[8] C.P. Kuo, J.S. Yuan, R.M Cohen, J. Dunn and G.B. Stringfellow, Appl. Phys. Lett., **44**, 550 (1984)

[9] G.E. Coates, M.L.H. Green, and K. Wade, Organometallic Compounds: The Main Group Elements, Vol. I, 3rd ed., London: Meuthen &Co., LTD, (1967)

[10] Koichi Nakamura a, Osamu Makino b, Akitomo Tachibana, Koh Matsumoto, J. of Organometallic Chemistry **611**, 514 (2000)

[11] M. E. Coltrin, J.R. Creighton, C.C. Mitchell, J. of Cryst. Growth 287 (2006)

[12] C.H. Chen, H.Liu, D. Steigerwald, W. Imler, C.P. Kuo, M.G. Crawford, J. of Electronic Materials **25**, 1004 (1996)

[13] D.G. Zhao, J.J. Zhu, D.S. Jiang, Hui Yang, J.W. Liang, X.Y. Li, H.M. Gong, J. of Cryst. Growth **289**, 72 (2006)

[14] C.B. Cooper III, M.J. Ludowise, V. Aebi, R.L. Moon, J. Electron. Mater **9**, 299 (1980)

[15] J. Han, J.J. Figiel, M.H. Crawford, M.A. Banas, M.E. Bartram, R.M. Biefeld, Y.K. Song, A.V. Nurmikko, J. of Cryst. Growth **195**, 291 (1998),

[16] S.J. Bass, C. Pickering and M.L. Young, J. Cryst. Growth **64**, 68 (1983),

[17] M. Ludowise, MO of III-V Semicoductors, J. Appl. Phys., **58**, R31 (1980)

[18] D.G. Zhao, J.J. Zhu, D.S. Jiang, Hui Yang, J.W. Liang, X.Y. Li, H.M. Gong, J. of Cryst. Growth **289**, 72(2006)

[19] J. Stellmach, M.Pristovsek , O. Savas, J.Schlegel, E.V.Yakovlev, M.Kneissl, J. of Cryst. Growth, **315**, 229 (2011)

[20] A. Kakanakova-Georgieva, R. R. Ciechonski, U. Forsberg, A. Lundskog and E. Janzén, Crystal Growth & Design **9,** 880 (2009)

[21] S. Keller, P. Cantu, C. Moe, Y. Wu, S. Keller, U. K. Mishra, J. S. Speck, S. P. DenBaars, Jpn. J. Appl. Phys, **44**, 7227 (2005)

[22] D. Endres,S. Mazumder, J. of Cryst. Growth, **335**, 42 (2011)

[23] H.J. Kim, S. Choi,D.Yoo , J.H. Ryou , R.D.Dupuis, J. of Cryst. Growth, **310**, 4880 (2008)

[24] H.J. Kim, S. Choi, D. Yoo, Jae-Hyun Ryou, Russell D. Dupuis, R. F. Dalmau, P. Lu, Z. Sitar, Appl. Phys. Lett., **93**, 4880 (2008)

[25] C.Moe, UCSB Dissertation Thesis, Growth and Fabrication of Deep Ultraviolet Light Emitting Diodes on Silicon Carbide Substrates, (2007)

[26] G. Bauer, W. Richter, Optical Characterization of Epitaxial Semiconductor Layers, Springer, “High Resolution X-Ray Diffraction” Ch 6, (1996)

[27] S. Yamada, J. Kato, S. Tanaka, and I. Suemune, A. Avramescu and Y. Aoyagi, N. Teraguchi and A. Suzuki, Appl. Phys. Lett., **78**, 3612 (2001)

[28] Y. Taniyasu, M. Kasu, and T. Makimoto, J. Cryst. Growth **298**, 310 (2007)

[29] E. D. Bourret-Courchesne, K. M. Yu, M. Benamara, Z. Liliental-Weber, and J. Washburn, J. Electron. Mater. **30**, 1417 (2001)

[30] K. Jeganathan, M. Shimizu, and H. Okumura, Appl. Phys. Lett. **86**, 191908 (2005)

[31] Z. Chen, S. Newman, D. Brown, R. Chung, S. Keller, U. K. Mishra, S. P. Denbaars, and S. Nakamura, Appl. Phys. Lett. **93**, 191906 (2008)

[32] Z. Chen, H. Zhi-Biao, R. Fan, H. Jian-Nan, L. Yi, Chin. Phys. Lett. **27**, 058101 (2010)

[33] S. Kitagawa, H. Miyake, and K. Hiramatsu, Jap. J. of Appl. Phys. **53**, 05FL03 (2014)

[34] X.Li, Y.Wei, S.Wang, H.Xie, T.Kao, M. Satter, S. Shen, P.D. Yoder, T. Detchprohma, R.D. Dupuis, A.M. Fische, F.A.Ponce, Phys. Status Solidi **252**, 76 (2015)

[35] S. Chen, Y. Li, Y. Ding, S. Li, M. Zhang, Z. Wu, A. Fang, J. Dai, C. Chen, J. of Electr. Materials **44**, 217 (2015)

[36] X. Zhang, F. J. Xu, J. M. Wang, C. G. He, L. S. Zhang, J. Huang, J. P. Cheng, Z. X. Qin, X. L. Yang, N. Tang, X. Q. Wang and B. Shen, Cryst. Eng. Comm. **17**, 7496 (2015)

[37] Y. Guo, Y. Fang, J.Yin, Z. Zhang, B. Wang J. Li, W. Lu, Z. Feng, J. of Cryst. Growth **464**, 119 (2017)

[38] S. Karpov and Y.N. Makarov, Appl. Phys. Lett. **81**, 4721 (2002)

[39] M. Kneissl, T. Kolbe, C. Chua, V. Kueller, N Lobo, J. Stellmach, A. Knauer, H. Rodriguez, S. Einfeldt, Z. Yang, N. M. Johnson and M. Weyers, Semicond. Sci. Technol. **26,** 014036 (2011)

[40] B. Heying , X. H. Wu , S. Keller , Y. Li , D. Kapolnek , B. P. Keller , S. P. DenBaars , and J. S. Speck, Appl. Phys. Lett. **68**, 643 (1996)

[41] S. R. Lee, A. M. West, A. A. Allerman, K. E. Waldrip, D. M. Follstaedt, P. P. Provencio,D. D. Koleske, Appl. Phys. Lett. **86**, 241904 (2005)

[42] I. Y. Knoke, P. Berwian, E. Meissner, J. Friedrich, H. P. Strunk, and G. Müller, J. Cryst. Growth **312**, 3040 (2010).

Chapter 8: Growth of AlGaN

In this final chapter, we will discuss the growth of aluminum gallium nitride. The deposition of AlGaN onto AlN continues by the step flow growth mode established by the underlying AlN and is initially strained to the AlN, relaxing only after a sufficient thickness has been achieved. When grown on sapphire, an AlN/AlGaN superlattice is required to prevent cracking of thick AlGaN layers. However, for the case of AlN layers grown on SiC of at least 250 nm, no superlattice is required [1].

The first portion of this chapter will be devoted to optimizing the growth of AlGaN and the different parameters which were investigated to change the Al content (wavelength emission) and the roughness of the film. The second portion will focus on the growth and electrical characterization of AlGaN:Si.

8.1 Growth Optimization for Undoped AlGaN

The growth of AlGaN in this chapter was done entirely on the Taiyo Nippon Sanso SR4000HT. As mentioned previously, I was the first graduate student to use this new reactor at UCSB; therefore optimal growth parameters were unknown. In this section we will discuss the process by which we determined how to accurately calculate the Al composition by cathodoluminescence and reciprocal space maps. Additionally we will discuss how different "knobs and dials," i.e. growth temperature, precursor flow, etc. were varied to tune the Al composition and roughness of the films for the different AlGaN layers in a UV LED.

8.1.1 Determining Aluminum Composition

At the start, determining the Al composition was a challenge. The majority of growers use a PL setup to calibrate their alloy compositions after a growth for quick feedback. However, the majority of them grow InGaN/GaN structures and there are dedicated lasers/ PL setups for this wavelength / materials system.

For the UV group, the PL laser setup only goes down to 265 nm. Given that the compositions of many of our films will be emitting at much lower wavelengths (between 230-260nm) for the varying AlGaN layers of the UV device structure, there is no quick feedback loop for this. For reference, the relationship between the Al composition and wavelength emission is plotted in Fig. 8.1 [2]. Therefore, we had to resort to other methods.

The first method by which one can calculate the Al composition is with cathodoluminescence (CL). CL was performed using an FEI Scanning electron microscope (SEM) with a Gatan MonoCL4 system to obtain panchromatic cathodoluminescence spectra. Scans were taken with beam excitation energies in the range of 5-10 kV, corresponding to electron penetration depths in GaN of approximately 150 – 500 nm as calculated using the method described in [3]. This method is convenient because several samples can be placed on the stage and probe numerous samples, depending on their size. Additionally, CL only provides information on the emission wavelength and its spatial dependence (including regions of strong nonradiative recombination such as threading dislocations) Using Fig. 8.1, one can then translate the wavelength to an alloy composition.

The second method was by using XRD. Reciprocal space maps for the $(10\bar{1}5)$ reflection of AlN were measured using the Panalytical X'Pert Materials Research Diffractometer. The incident beam was a Ge (220) two-bounce Bartels monochromator with a pre-collimating mirror. The diffracted beam optics used was a Ge (220) with a 3D Pixcel detector. This method tells you exactly what the composition is, as well as the state of coherency with the underlying AlN substrate. The downside with this method is that it can only do one sample at a time, and RSMs generally take at least a few hours for accurate and detailed scans, which are always preferable.

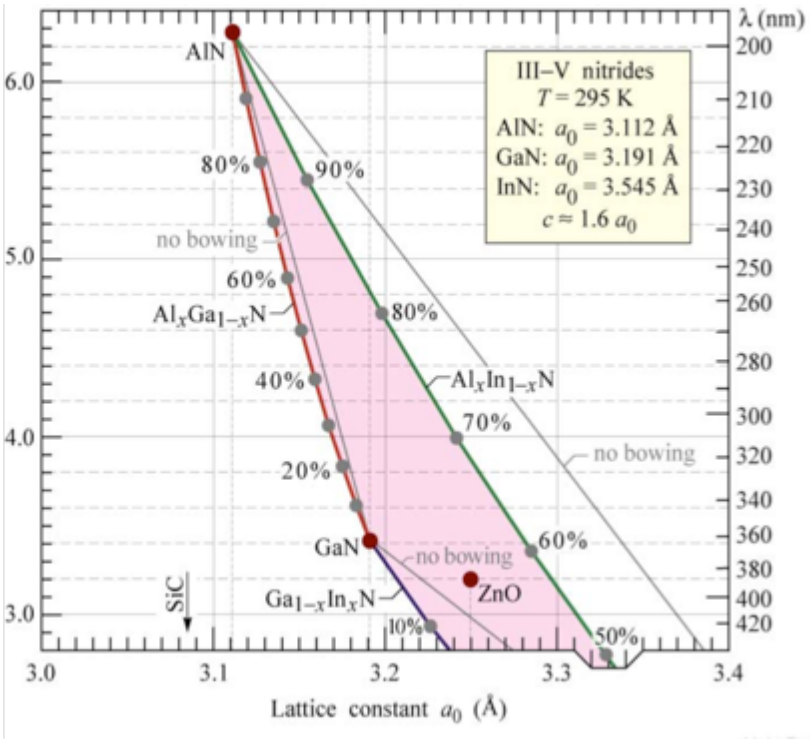

Figure 8.1 Dependence of emission wavelength on lattice constant for AlGaN.

Fig. 8.2 plots the Al composition derived from CL and Fig 8.1 as a function of Al composition from RSM for a variety of samples grown over the past few years with the

SR4000HT. One can note that for any given sample the Al% measured from the two independent methods are in good agreement with one another. This is a great result, because one method can then be used to back up the other. For sensitive growths, Al% was usually determined via RSMs. For quick feedback, CL was the go to technique for Al % determination.

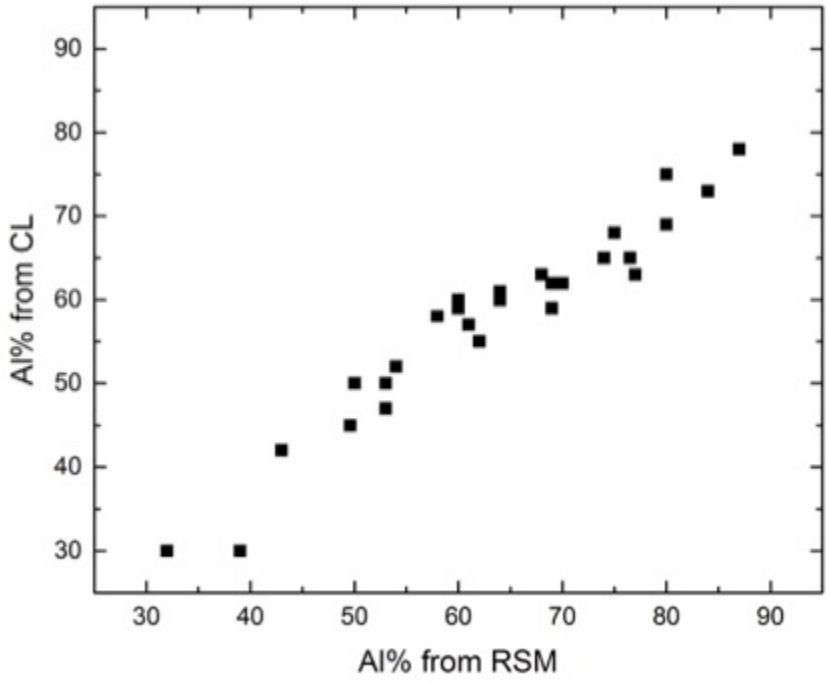

Figure 8.2 Aluminum Composition Calculations from CL and RSM. A downward bowing is observed for the band gap of AlGaN due to Vegard's Law and can be seen in the CL composition. The RSM result is therefore more accurate.

8.1.2 Optimizing Aluminum Composition

The full UV LED structure will contain AlGaN at varying Al compositions. The quantum well will have ~42% Al to emit at 280 nm. Ideally, the n-AlGaN, p-AlGaN, and

barrier layer will be 65% Al, so as to enhance carrier confinement in the well. However, growing AlGaN at such high Al mole fractions will be a challenge, as mentioned previously. Therefore, a composition between 50-65% for these layers is also acceptable, as long as it does not absorb the light coming out of the well. In this section we will discuss how changing the gas flow and temperature affect the Al composition.

Fig. 8.2 plots the Al% as a function of growth temperature. The Al% increases linearly with temperature, when the TMAl, TMGa, and NH_3 are held constant as shown at the bottom of the plot. Given that higher temperatures promote smooth step flow morphology, growths at 1250 °C will be used moving forward

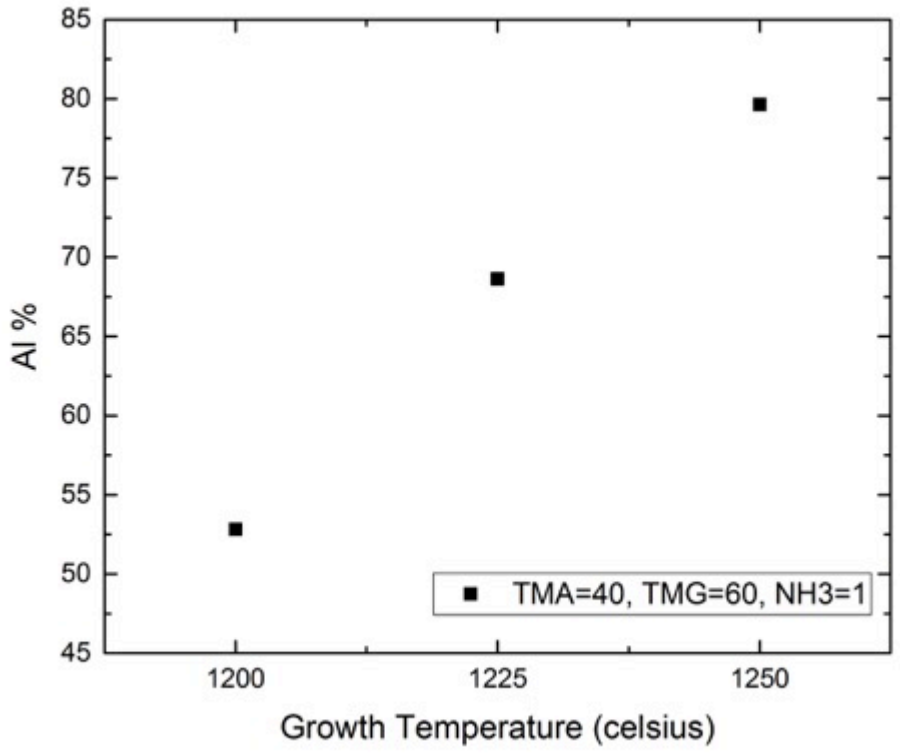

Figure 8.2 Aluminum Composition as a function of Growth Temperature at TMAl flow of 40 sccm, TMGa flow of 60 sccm and NH_3 flow of 1slm.

Fig. 8.3 plots the Al composition calculated by CL as a function of varying TMAl flow. As the TMAl was varied from 40 to 160 sccm, essentially quadrupled, there was little change in the Al%. The temperature, TMGa, and NH_3 were held constant at 1250°C, 30 sccm, and 1 slm, as shown in the bottom right of the figure. From this, one can gather that after a certain TMAl flow, the Al species saturates and no longer takes the place of a Ga atom adsorbing on the surface. Therefore for the sake of the conserving MO source, it would be wise to use a smaller TMAl flow, as it does not impact the Al content in the AlGaN.

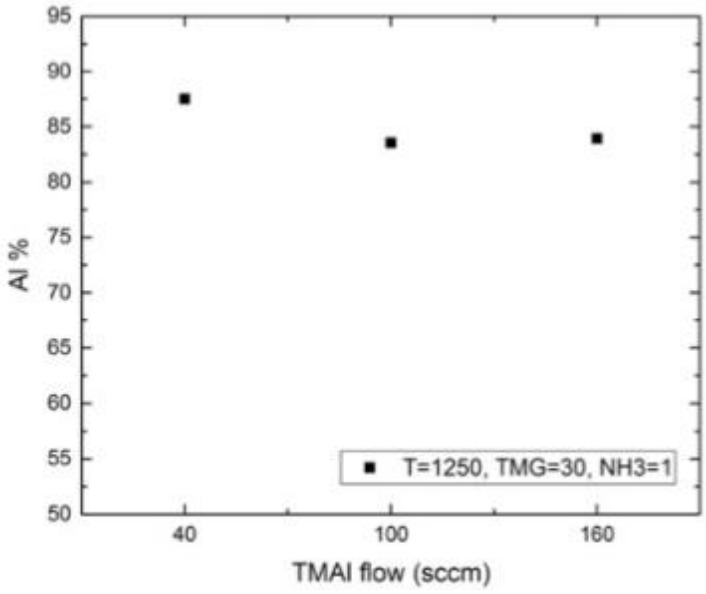

Figure 8.3 Dependence of aluminum content in AlGaN as a function of TMAl flow for a growth temperature of 1250 C and TMGa flow of 30 sccm and NH_3 flow of 1 slm.

Fig 8.4 plots the dependence of Al content on the NH_3 flow. From the plot it is evident that regardless of the other conditions in the legend, there is a direct correlation

between the Al content in the AlGaN and NH_3 flow, which makes it a convenient way of changing the alloy composition, as is the growth temperature. As the ammonia flow is increased, the Al content decreases. The Group V source is not primarily used to change growth rate or alloy composition as it is not the limiting factor (the group III source is). NH_3 is also used at a much larger volume than the group III precursors, on the order of slm, not sccm.

However, with increasing ammonia flow, we also see an increase in pre-reactions between TMAl and/or TMGa with NH_3, which suppresses the group III source, i.e. TMGa from adsorbing onto the surface and therefore lowering the aluminum composition. When combined with a large TMGa flow as the red circular data points show (TMGa = 160 sccm), the change in Al composition is even more evident as we see almost a 30% decrease in Al% after increasing the ammonia flow by just 1slm.

For smaller TMGA flows, i.e. the upside down purple triangles or blue triangles (TMGa=10), the change in Al% is less evident, though still inversely proportional. An interesting note is that we were able to accomplish growing ~ 60 % Al for varying ammonia flows and growth conditions, which is beneficial because it is the composition of interest for the thicker layers in the device structure, or at least in the optimal composition window (50-65% Al).

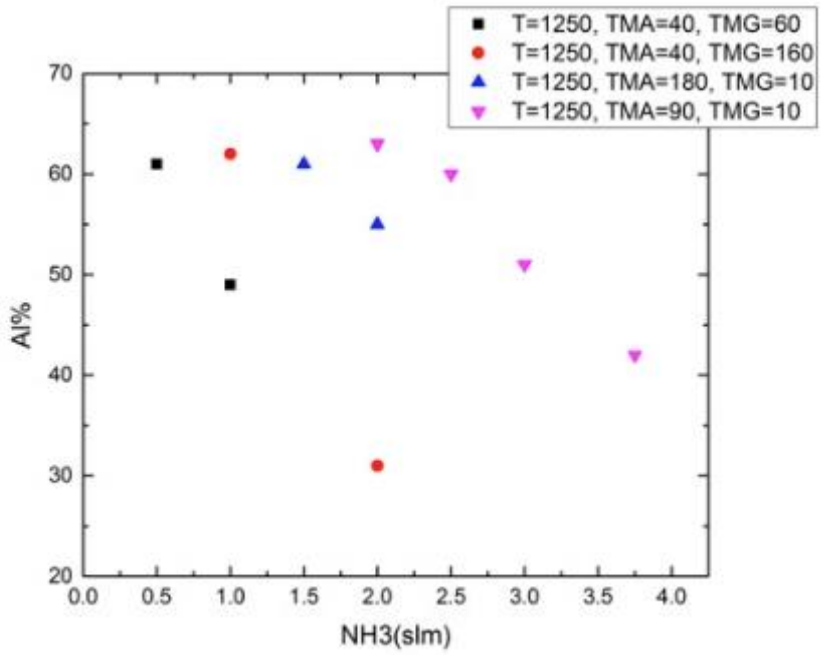

Figure 8.4 Dependence of Aluminum composition as a function of NH_3 flow. Increasing the NH_3 flow decreases the Al composition. There is a larger drop in composition with increased TMGa flow.

Fig. 8.5 plots the Al composition as a function of TMGa flow for varying TMAl and NH_3 flows, which are seen in the legend. Unlike varying TMAl, when varying TMGa, the Al composition does change, especially at higher NH_3 flows (2 slm), as shown in the previous plot (Fig. 8.4). This is most evident in the triangular data points, which have the higher ammonia flow. For lower ammonia flows and TMAl flows, changing the TMGa does not heavily impact the Al content in the AlGaN, which is a conclusion we can safely come to after analyzing the previous plots, however would be convenient when small changes in the Al% want to be made.

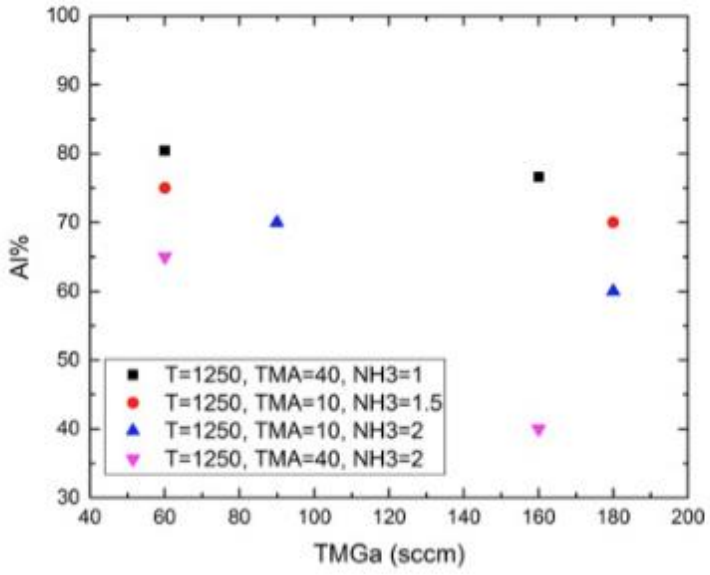

Figure 8.5 Aluminum Composition as a function of TMGa flow. Higher NH_3 flows shows more pronounced changes in the Al composition.

Finally, to summarize our finding the two most practical growth variables to turn to control the composition of AlGaN is the temperature and TMGa flow. Though NH_3 was shown to vary the Al%, it is not the rate-limiting source that is traditionally used to vary conditions in III-nitrides. TMAl was shown to have little impact on the Al content in the AlGaN. Therefore, Fig. 8.6 plots the wavelength emission recorded by CL as a function of TMGa flow for varying temperature conditions ranging from 1200 °C to 1050 °C. Note from the figure, that varying the temperature and TMGa flow can target different layers of the UV structure.

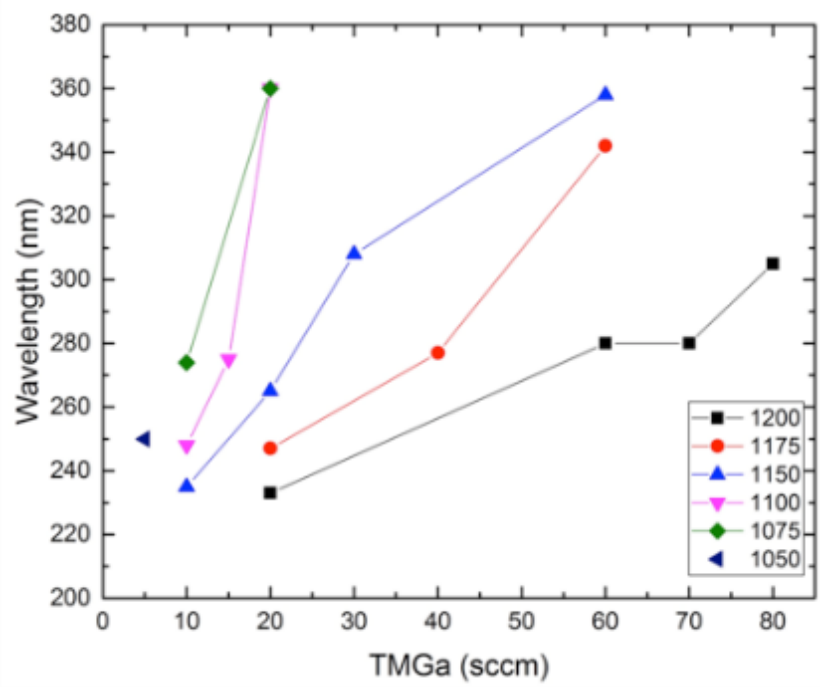

Figure 8.6 Dependence of the CL wavelength emission on the TMGa flow for a range of growth temperatures.

8.1.3 Minimizing the Roughness of AlGaN

The roughness of the AlGaN layers is investigated next. It is important to have smooth films with low root mean squared (RMS) roughness. Smooth underlayers are ideal when depositing the active region, as it provides less variation in your wavelength emission. At the very least, we would like to have AlGaN films with a RMS roughness under 1nm. Just like when tuning the Al composition, one can use the same "knobs and dials" to decrease the roughness of our layers, i.e. growth temperature, TMAl, TMGa, and NH_3 flow.

Fig. 8.6 plots the RMS roughness as a function of growth temperature with the TMAl, TMGa, and NH_3 held constant at 40 sccm, 60 sccm, and 1slm, respectively. One can note that the roughness is reduced six-fold over a growth temperature increase of

50°C. At 1250°C, the surface has a roughness of approximately 1nm, which is an acceptable starting off point. The AlGaN growth temperature and will be held constant at 1250°C unless otherwise specified due to doping.

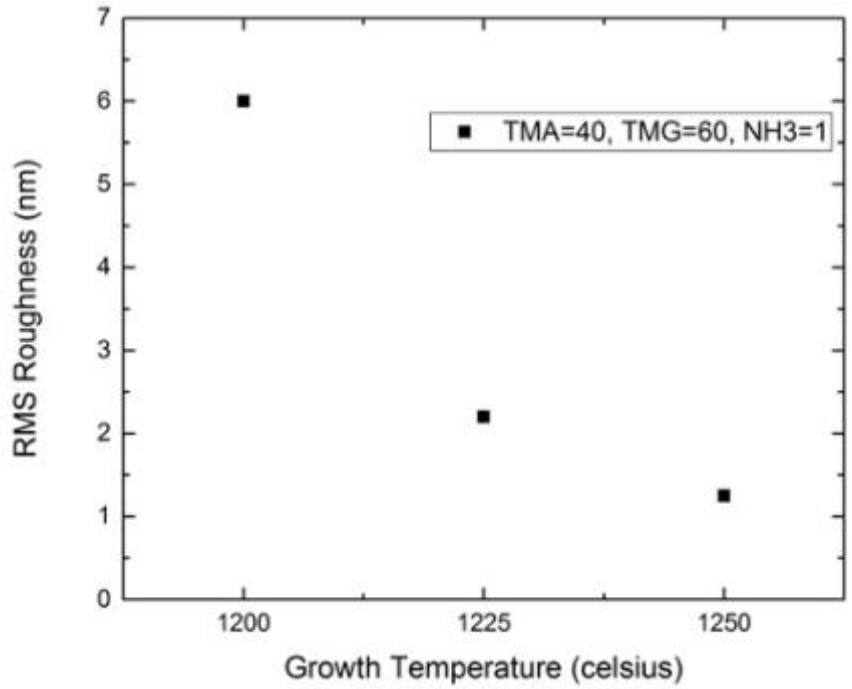

Figure 8.7 Dependence of the film roughness on growth temperature for AlGaN films with TMAl flow of 40 sccm, TMGa flow of 60 sccm and NH_3 flow of 1 slm.

Fig. 8.7 plots the RMS roughness as a function of TMAl. The flow of TMAl does not change the roughness by much. Increasing the TMAl four-fold sees a marginal change in the RMS roughness and it essentially stays around 1nm. Therefore, it is not a viable "knob" to change to get the roughness below 1nm. However, for future growths, it would be ideal to flow less TMAl, so that precursor can be spared.

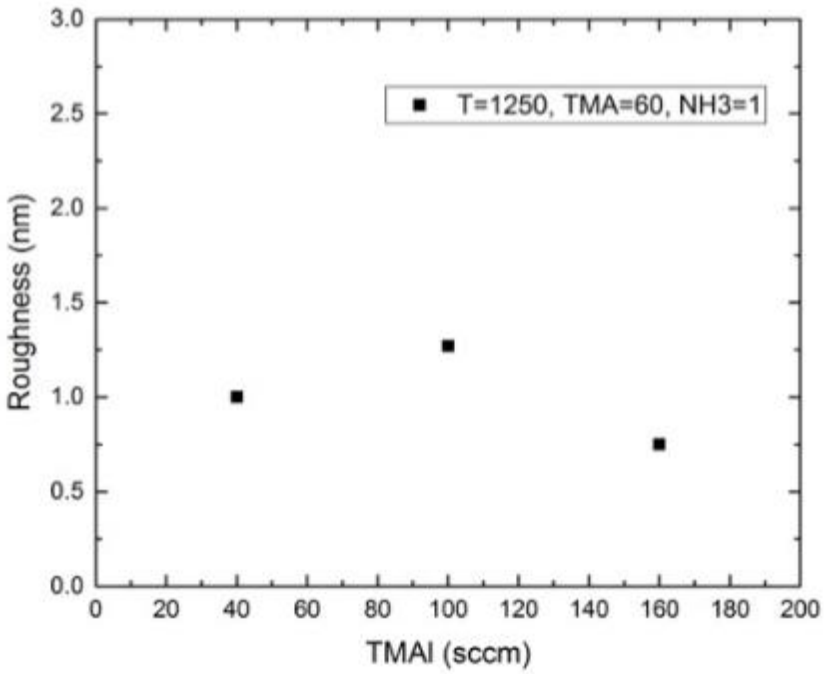

Figure 8.8 RMS Roughness as a function of TMAl flow at temperature of 1250 °C, TMAl flow of 60 sccm, and NH_3 flow of 1 slm

Fig 8.8 plots the RMS roughness as a function of the ammonia flow. Regardless of TMAl flow, the optimal flow for a RMS roughness below 1 nm seems to be between 1.5 slm and 2.5 slm. This result is made clear by focusing on the triangular data points that have a TMAl flow of 180 sccm (right side up triangle) and 90 sccm (upside down triangle), but the same growth temperature (1250 °C) and TMGa flow (10sccm). At NH_3 flows less than 1.5 slm, the roughness reaches 6 nm, however this is also in part due to the high TMGa flow (60 and 160 sccm) in comparison to the blue and purple triangular data points (TMGa = 10sccm). At NH_3 flows greater than 2.5 slm, there is a gradual increase in the roughness as more ammonia is used (upside down purple triangles), however the low TMGa flow (10 sccm) prevents the roughness from getting as high as the results using 60 or 160 sccm of TMGa. Therefore to obtain RMS roughness below 1

nm, a growth temperature of 1250 °C, low TMAl flow (~40-60 sccm), low TMGa flow (~10-20 sccm), and NH_3 flow between 1.5-2.5 slm is desirable. Of course reactor conditions will fluctuate and reactor maintenance will require growers to re-calibrate growth conditions. Therefore these studies should be taken as a guide and an aide in finding optimal conditions, but these conditions are by no means set in stone.

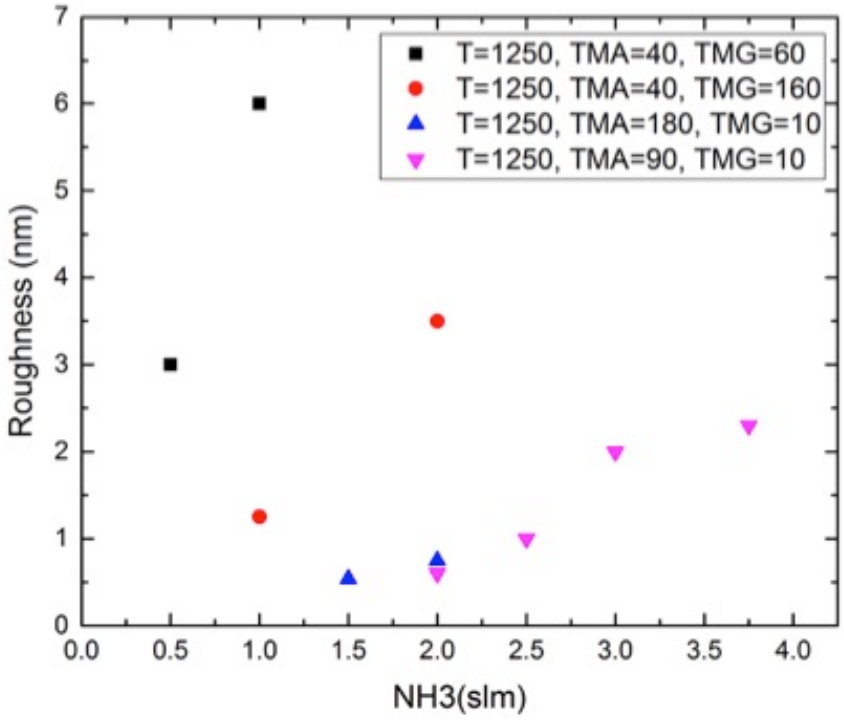

Figure 8.9 Dependence of surface roughness as a function of NH_3 flow for AlGaN films. The optimal NH3 flow for low roughness films, regardless of other conditions, is between 1.5-2 slm.

Fig. 8.10 is a plot showing the change in roughness as a function of Al composition for a variety of AlGaN samples grown on the SR4000HT, ranging from 10% Al to 75% Al. Within the plot are AFM height retrace scans showing the surface morphology at Al compositions of interest, more specifically 45% Al, 55% Al, and 65%

Al. Using the optimized conditions mentioned previously, we were able to grow a wide range of AlGaN samples at varying Al compositions and keep the roughness below 0.5 nm. Additionally, as we increased the Al composition toward more desired wavelengths for our UV device structure, the RMS roughness was actually lower. The RMS roughness was 0.12, 0.075, and 0.07 nm at 45, 55, and 65% Al, respectively. Furthermore we can see from the height retrace scans that as we increase the Al composition the morphology of the AlGaN surface improves. One notes how with increased Al composition, step flow morphology is produced with clear and defined step edges, most notably at 65% Al.

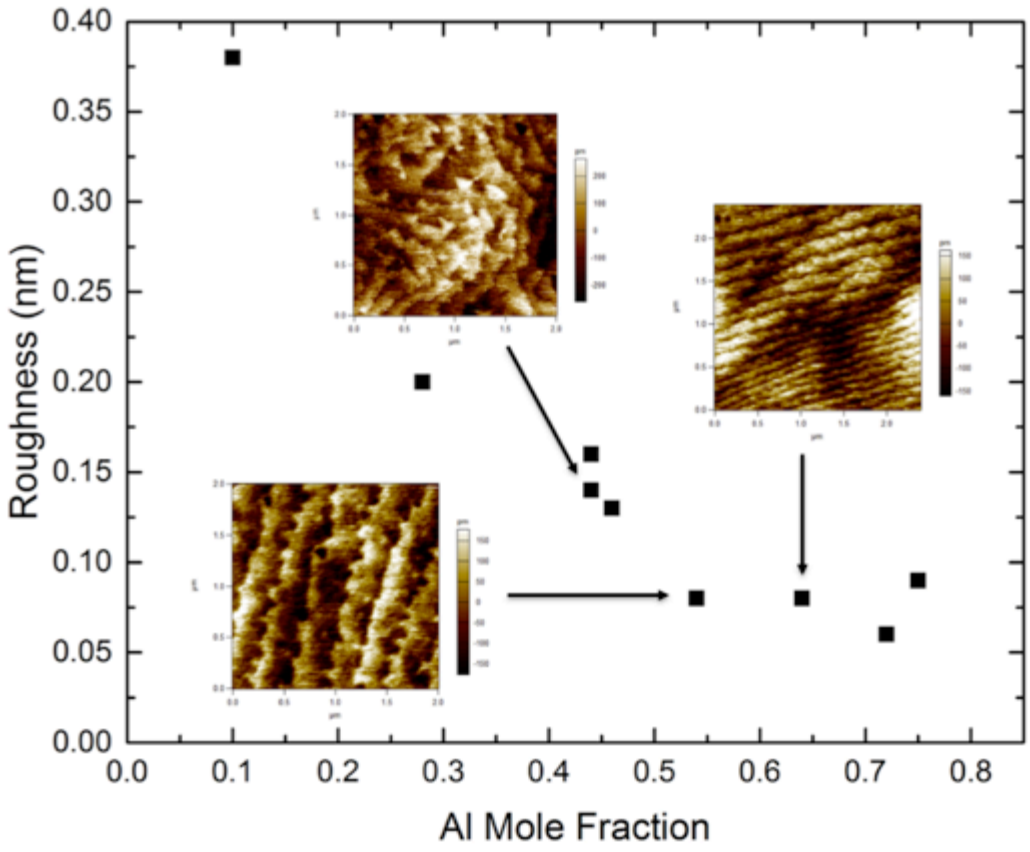

Figure 8.10 RMS Roughness as a function of Al Mole Fraction

8.2 Electrical Characterization of Silicon Doped AlGaN

In this section we will discuss the electrical characterization of silicon doped AlGaN. We will first focus on varying the parameter in the MOCVD that controls the flow of disilane (S_2H_6), which is the Si precursor. We will also investigate the incorporation of Si in AlGaN via secondary ion mass spectroscopy (SIMS) and then compare it to the electron concentration determined by the Hall measurement. We will then measure the electron mobility, which is also determined using the Hall effect. Finally, we will discuss the resistivity of AlGaN:Si as a function of Al composition.

8.2.1 Silicon and Electron Concentration

As mentioned, Si_2H_6 is traditionally the precursor used to dope III-nitrides n-type. Using the SR4000HT, the disilane flow is controlled by a series of mass flow controllers (MFCs) that control the source, dilution, and injection of disilane into the MOCVD reactor chamber during a growth. Given that there are three separate MFCs, which control the disilane flow, it is convenient to have a relation between them, expressed as the effective flow. The effective flow of Si is displayed in Eq. 1

$$[Si\ eff.] = \left(\frac{[MFC\ Source\ ]}{[MFC\ Source\ ]+[MFC\ Dilution\ ]}\right) * [MFC\ injection\ ] \qquad (1)$$

where each term is the volume of gas (sccm) that flows through the respective MFC that it belongs to (Source, Dilution, Injection).

Following a growth, the doping concentration can be measured and calculated using SIMS with Dr. Tom Mates. SIMS is a tool used to analyze the chemical composition of thin films by hitting a position on the surface of the sample with a focused primary ion beam, then collecting and analyzing the ejected secondary ions. The SIMS has two primary ion sources, cesium and oxygen. The mass/charge ratios of these secondary ions are measured with a mass spectrometer to determine the elemental composition of the surface. Depending on the sample, it can achieve a depth resolution of 2 nm. Masses from 1 amu to 360 amu can be detected, and the mass resolution is sufficient to eliminate nearly all interferences. SIMS is the most sensitive surface analysis technique, with elemental detection limits ranging from parts per million to parts per billion.

The electron concentration in AlGaN:Si is measured by the Hall effect. When current is flowing in one direction and a magnetic field is present in an orthogonal direction, an electric field is created orthogonally to both the current flow and the magnetic field. The measured voltage created by the induced electric field is called the Hall voltage. The Hall coefficient is the induced electric field divided by the current density and the applied magnetic field. The Hall coefficient can then be used to calculate the density of the charged carriers from Si doping.

When a mobile charged particle, such as an electron, is within an electric field, the charged particle will feel a force and flow current in that respective direction. If a magnetic field is present perpendicular to the moving charge carrier, then it will also experience a Lorentz force, which is perpendicular to both the electric and magnetic field.

A derivation of the Hall voltage for electrons in a semiconductor with a magnetic field in the z-direction is as follows [4]. Current (I) flows in the x-direction:

$$I=J_x wt=qnv_x wt \tag{2}$$

where $J_x$is the current density, q is the charge, n is the concentration of electrons, v_x is the velocity of electrons, t is the thickness of the semiconductor in the direction of the magnetic field, and w is the thickness of the semiconductor in the third direction. In steady state, no net charge flows in the y-direction, and the electrical (E) and magnetic forces (B) in this direction are balanced:

$$F=q\ [E+(v\times B)]=0 \tag{3}$$

$$E_y=(v_x * B_z) \tag{4}$$

Substituting the current for the velocity, v_x:

$$E_y=((I/qnwt)*B_z) \tag{5}$$

Since we measure the Hall voltage and not the electric field in the y-direction:

$$V_H=-E_y * w \tag{6}$$

$$V_H/w=-((I/qnwt)*\mathrm{B_z}) \tag{7}$$

The equation can be rearranged with the Hall coefficient, $R_H=1/qn$:

$$V_H=\mathrm{R_H}*(\mathrm{I}*\mathrm{B_Z}/\mathrm{t}) \tag{8}$$

Once the Hall coefficient is known, the carrier concentration and mobility of the carriers can be calculated from the Hall coefficient and the current:

$$n=1/qR_H \quad (9)$$

$$\mu=R_H I/wtE_x \quad (10)$$

We will now discuss how the electrical characterization of AlGaN:Si was done, specifically the processing techniques necessary to fabricate samples for electrical testing. Burhan Saifaddin and Christian Zollner processed all samples. First, as-grown samples were cleaved into squares for Van der Pauw testing using Indium. Four contacts were deposited onto the samples' corners using In solder wire. Samples were then measured in a LakeShore Hall system, using LakeShore's commercially available software to automate the van der Pauw measurements and calculations.

Samples that showed promising results with indium dots, i.e. had good mobility and carrier concentration values, were selected for more detailed study. These samples were cleaned in boiled HCl to remove In residue, then cleaned in solvent. Using standard photolithography techniques, Ti/Al/Ni/Au contacts were deposited using e-beam evaporation, and Greek cross mesa structures were etched into the AlGaN using reactive ion etching in a chlorine-based chemistry. To form ohmic contacts, samples were annealed under flowing nitrogen at 830° C.

Fig. 8.11 is a plot showing the concentration of Si atoms determined via SIMS and the concentration of electrons determined using the Hall measurement as a function of the effective flow of silicon used in the growth step. At 1 sccm the Si concentration was determined to be ~ 4 x 10^{18} cm^{-3} and the electron concentration was ~ 8 x 10^{17} cm^{-3} while at 4 sccm, the Si effective flow was close to 2 x 10^{19} cm^{-3} and the electron concentration was 4 x 10^{18} cm^{-3}. As we incrementally increase the Si effective flow, the

Si concentration incrementally increases as well. Furthermore, after 1 sccm Si effective flow the electron concentration does not seem to increase with increasing Si effective flow. It fluctuates between 2-4 x 10^{18} cm^{-3}.

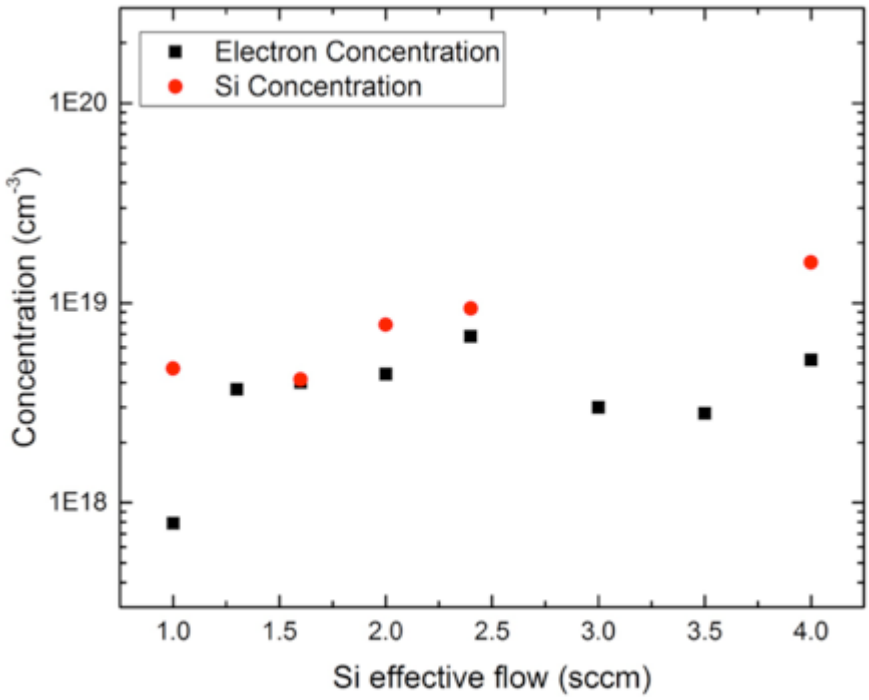

Figure 8.11 Dependence of measured electron and Si concentration on the effective disilane flow for AlGaN layers with nominal Al content 50% and thickness ~300nm.

Fig. 8.12 plots the difference between the Si concentration and the electron concentration from Fig. 8.11 as function of Si effective flow. From 1 to 2.5 sccm in Fig. 8.12, the difference is approximately 2 to 4 x 10^{18} cm^{-3}, where at ~1.5 sccm, the difference is an order of magnitude lower (10^{17} cm^{-3}). However, at 4 sccm the difference between the Si and electron concentration is ~ 1.1 x 10^{19} cm^{-3}, an order of magnitude greater than at the lower Si effective flows.

There can be a few reasons for this. One reason could be that under the present growth conditions, the electron concentration has saturated and no matter how much disilane you flow, it just won't fully adsorb and contribute to electron flow. Another reason could be that Si is not fully ionized due to compensation by unintentional impurities such as oxygen, which we know are present in large quantities because of its affinity to aluminum. A great way to test this for future students would be to do SIMS again in a nearby region of the sample and look for and quantify the concentration of oxygen. It would be interesting to see if matches the difference between the Si and electron concentration.

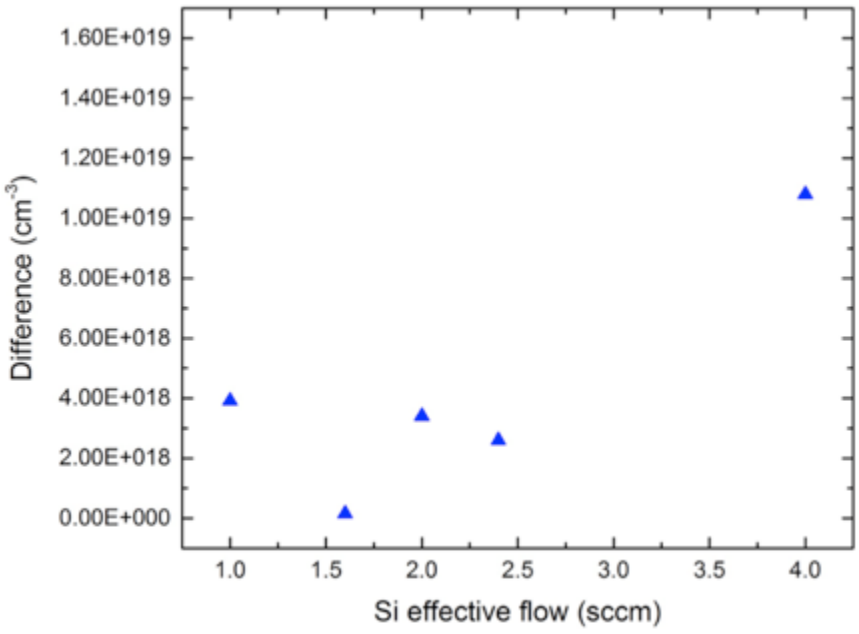

Figure 8.12 Difference between Electron and Si Concentration as a function of Si effective flow

8.2.2. Electron Mobility in AlGaN:Si

Mobility is a measure of how easily carriers move through a material and as mentioned earlier is measured by the Hall effect. Measuring the electron mobility is one of the best ways to quantify material without performing other characterization steps like TEM or XRD to get a sense of the material quality. This is because defects, such as crystal lattice imperfections or TDD, will scatter electrons/charge carriers and reduce the electron mobility.

For the AlGaN materials system, electron mobility is known to decrease with increasing Al% composition, which is a problem when trying to realize high quality deep UV LEDs, which must have high Al compositions. This is partly due to the large threading dislocation density present in the material as the Al% is increased. Therefore to achieve high mobility values, it is important to grow AlGaN:Si on low dislocation density AlN layers.

Fig. 8.13 plots the mobility of AlGaN:Si as a function of Al composition. Fig. 8.13a is AlGaN:Si grown at UCSB on AlN layers with TDDs 3 x 10^9 cm^{-2}, 7 x 10^8 cm^{-2}, and 9 x 10^9 cm^{-2}, respectively. Fig. 8.13b are the mobility values from the literature alongside the data points determined at UCSB.

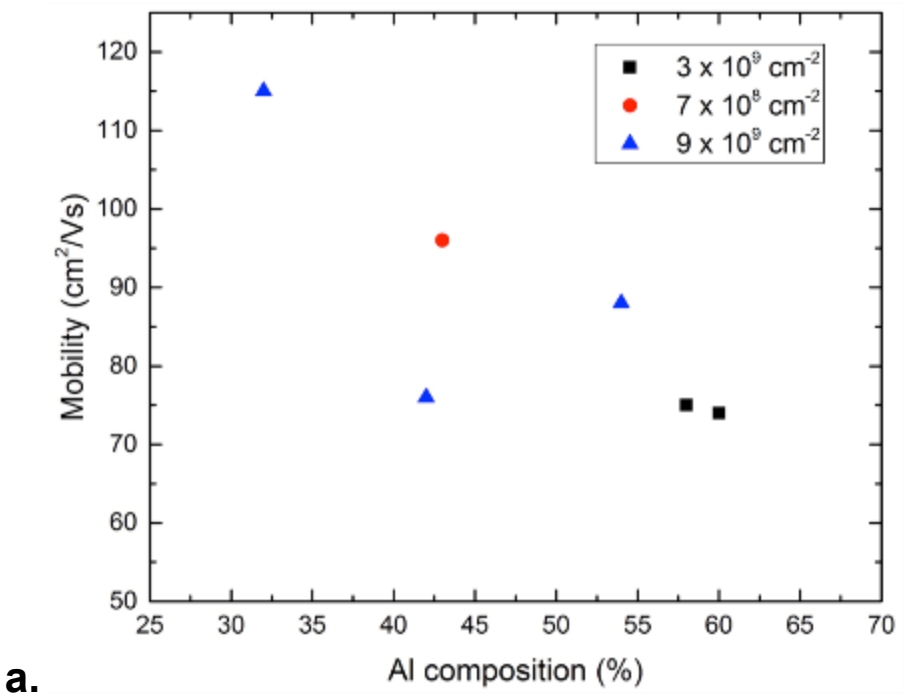

a.

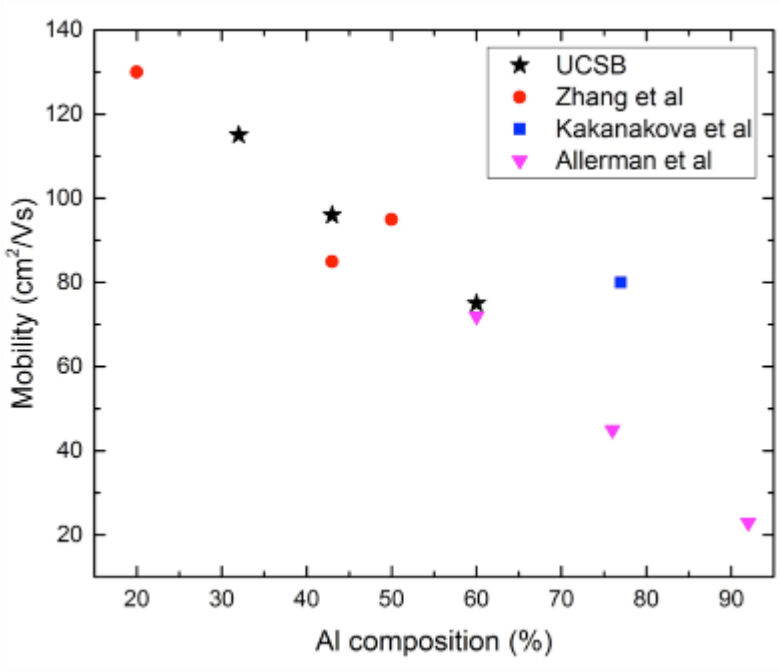

b.

Figure 8.13 Electron Mobility for Varying Dislocation Densities for **(a.)** UCSB and **(b.)** Literature as a Function of Al composition

All growths in Fig. 8.13a had a Si effective flow of ~1.5 sccm. Now with

increasing dislocation density we should expect the electron mobility to decrease, as well as with increasing Al%. At 9 x 10^9 cm^{-2}, we have results ranging from 32 to 55% Al. At 32% the electron mobility is 115 cm^2/Vs (5.2 x 10^{18} cm^{-3}). As we increase the Al% to 42% the mobility drops to 72 cm^2/Vs. When it further increased to 55% Al, the mobility increased to 88 cm^2/Vs. The reason why the higher composition has a larger mobility is because the electron carrier concentration at 42% Al was 3.7 x 10^{18} cm^{-3} and at 55% it was 8 x 10^{17} cm^{-3}. The lower electron concentration allows for greater electron mobility. The variance in electron concentration for the same Si effective flow is likely due to reactor conditions drifting. At 3 x 10^9 cm^{-2} there are two data points (58 and 60% Al), which have essentially the same mobility (75 and 72 cm^2/Vs, respectively), with a carrier concentration of ~3.6 x 10^{18} cm^{-3} for both. At 7 x 10^8 cm^{-2}, the sample had an alloy composition of 4

2 % Al, with an electron mobility of 96 cm^2/Vs, which is 20 cm^2/Vs greater than the result with the same Al% but a larger TDD (9 x 10^9 cm^{-2}). The carrier concentration was 4 x 10^{18} cm^{-3}. The mobility increased by 26%, an example of how lowering the TDD can improve the mobility of AlGaN:Si.

Fig. 8.13b compared the literature results with material grown at UCSB [5-8]. All growths in the literature were on sapphire substrates. From a first glance we can see that as the Al % is increased there is a general decrease in the mobility of electrons in AlGaN:Si. The material made by Zhang *et al* ranged from 20% to 43% to 50% Al with a TDD of 5 x 10^8 cm^{-2}. The electron mobility for these compositions were 130, 85, and 95 cm^2/Vs, respectively. At 43% Al, the mobility is lower than the one reported at the same composition by UCSB, even though it has a slightly lower TDD. The carrier

concentration was fixed at ~ 2.2 x 10^{18} cm^{-3}. Kakanakova and Allerman *et al* focused on higher Al%. Kakanakova *et al* reported 80 cm^2/Vs at 77% Al, however did not report a TDD. The carrier concentration was 1.74 x 10^{18} cm^{-3} Allerman *et al* also investigated high Al% (60, 76, 92% Al) and reported mobilities of 72, 45, and 23 cm^2/Vs, respectively, all with a TDD of 7 x 10^9 cm^{-2}. The carrier concentrations were 2.6 x 10^{18} cm^{-3}, 3.5x 10^{18} cm^{-3}, 1.6 x 10^{17} cm^{-3}, respectively. The UCSB data points (black stars) are competitive with the UV community in the ranges from 30%-60% Al.

8.2.3 Resistivity in AlGaN:Si

The best metric for the electrical characterization of the material is electrical conductivity or its reciprocal, electrical resistivity. It is essentially a materials ability to either conduct or resist an electric current. For n-type material, i.e. AlGaN:Si, it is expressed as a product of the mobility, carrier concentration and electron charge; as shown by Equation 9:

$$\sigma=1/\rho= \mu*n*q \qquad (9)$$

where σ is the electrical conductivity, ρ is the electrical resistivity, μ is the electron mobility, n is the electron concentration, and q is the charge of an electron. The SI unit for conductivity is Siemens per meter (S/m) and for resistivity it is ohm-meter (Ω-m). Moving forward we will represent the data in terms of resistivity (mΩ-cm).

Resistivity is a more complete way of determining the electrical characteristics of the material because it takes into account both the mobility and carrier concentration. Additionally, the resistivity increases with increasing Al% composition.

Fig. 8.14 plots the resistivity of AlGaN:Si as a function of Al composition. As the Al % is increased there is a general increase in resistivity in AlGaN:Si, as to be expected. Fig. 8.14a is AlGaN:Si grown at UCSB on AlN layers with TDDs 3 x 10^9 cm^{-2}, 7 x 10^8 cm^{-2}, and 9 x 10^9 cm^{-2}. Fig. 8.14b are literature values for varying groups in the UV community alongside material grown at UCSB.

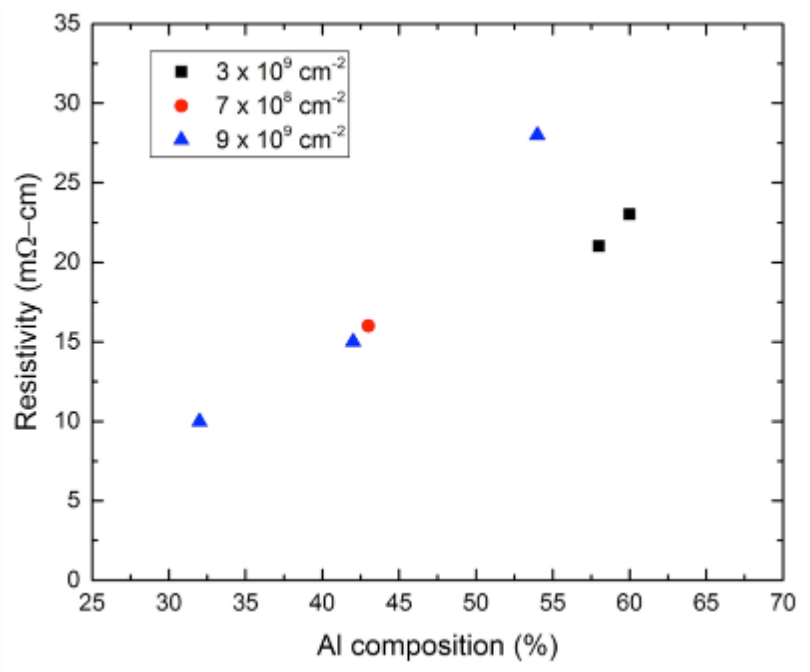

a.

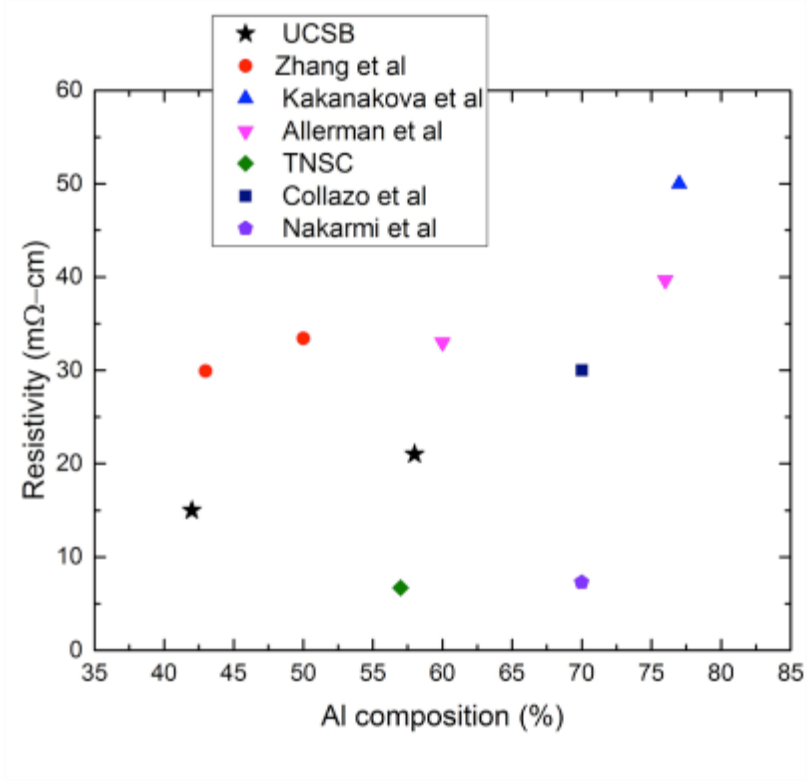

b.

Figure 8.14 Resistivity for Varying Dislocation Densities for **(a)** UCSB and **(b)** Literature as a Function of Al composition.

For Fig. 8.14a, at 9 x 10^9 cm^{-2}, we have data ranging from 32 to 55% Al. At 32% the resistivity is 10 mΩ-cm. As we increase the Al%, the resistivity increases to 15 mΩ-cm at 42%Al, and then 28 mΩ-cm at 54% Al. At 3 x 10^9 cm^{-2} there are two data points (58 and 60% Al), which have a resistivity of 21 and 23 mΩ-cm. At 3 x 10^9 cm^{-2}, the resistivity values are lower than the 9 x 10^9 cm^{-2} results at around 55-60% Al. The material with the lowest TDD (7 x 10^8 cm^{-2}) has a resistivity of 16 mΩ-cm at 43% Al. If we compare this alongside the 9 x 10^9 cm^{-2} sample at 42% Al, the resistivity is almost the same (15 mΩ-cm). It is suspected that in the 7 x 10^8 cm^{-2} sample, contact resistance due to processing variability increased the apparent resistivity of AlGaN:Si. Optimizing the processing of AlGaN:Si, such that undesirable forms of resistance (such as resistive non-ohmic contacts) can be reduced will aid in improving the measured resistivity of AlGaN:Si.

Fig. 8.14b compares literature results for resistivity to the material grown at UCSB. In addition to those discussed in Fig 8.13 a few more reports are added [9-12]. The material made by Zhang *et al* ranged from 20 to 43 to 50% Al with a TDD of 5 x 10^8 cm^{-2}. The resistivity values for these compositions were 19, 29, and 33 mΩ-cm, respectively. Kakanakova *et al* reported 50 mΩ-cm at 77% Al. Allerman *et al* investigated high Al% (60, 76% Al) and reported mobility values of 33 and 39 mΩ-cm, respectively, all with a TDD of 7 x 10^9 cm^{-2}. A report by Ikenaga *et al* from Taiyo Nippon Sanso (TNSC) showed AlGaN:Si with a resistivity of 6.7 mΩ-cm at 57% Al, which is the lowest resistivity reported in this thesis. Collazo *et al* from North Carolina Sate University (NCSU) reported a resistivity of 30 mΩ-cm, the only result here on bulk AlN single crystals; everyone else used the foreign substrate sapphire. Nakarmi *et al*

reported 7.3 and 23 mΩ-cm for 70 and 76% Al. The UCSB data points (black stars) are competitive with the UV community in the ranges from 40%-60% Al.

8.3 Conclusions

In this chapter we discussed how we mapped out the growth parameters and found optimal conditions for growing AlGaN. We found conditions were we could tune and control the Al% by changing the temperature and TMGa flow. Furthermore, we showed that we could achieve all these compositions and maintain an RMS roughness below 0.5 nm. Additionally, we showed the electrical characterization of AlGaN:Si. We found optimal Si effective flow conditions to maximize disilane usage and we achieved an electron mobility and resistivity of 96 cm^2/Vs and 15 mΩ-cm, respectively, for $Si:Al_{0.43}Ga_{0.57}N$.

References

[1] C.Moe, Growth and Fabrication of Deep Ultraviolet Light Emitting Diodes on Silicon Carbide Substrates, (2007)

[2]E.Schubert, Light Emitting Diodes 2nd edition, Cambride University Press, (2006)

[3] S.J. Rosner, E. C. Carr, M. J. Ludowise, G. Girolami, and H. I. Erikson," Appl. Phys. Lett. **70**, 420 (1997)

[4] E.C.H. Kyle, Growth Development of III-Nitrides for Electronic Devices by Molecular Beam Epitaxy, (2016)

[5] J.P. Zhang, H.M, Wang, W.H. Sun, V. Adivarahan, S.Wu, A. Chitnis, C.Q. Chen, M. Shatalov, E. Kuokstis, J.W. Yang and M.A. Khan, J. of Electr. Mat. **32**, 364 (2003)

[6] J. P. Zhang, H. M. Wang, M. E. Gaevski, C. Q. Chen, Q. Fareed, J. W. Yang, G. Simin, and M. Asif Khan, Appl. Phys. Lett., **80**, 3542 (2002)

[7] A. Kakanakova-Georgieva , D. Nilsson , X. T. Trinh , U. Forsberg , N. T. Son , and E. Janzén, Appl. Phys. Lett., **102**, 132113 (2013)

[8] A.M. Armstrong, M.W. Moseley, A.A. Allerman, M.H. Crawford, J.J. Wierer, J. of Appl. Phys. 117, 185704 (2015)

[9] R. Collazo, S. Mita, J. Xie, A. Rice, J. Tweedie, R. Dalmau, and Z. Sitar, Phys. Status Solidi C, **8**, 2031 (2011).

[10] M. L. Nakarmi, K. H. Kim, K. Zhu, J. Y. Lin, and H. X. Jiang, Appl. Phys. Lett. **85**, 3796 (2004)

[11] F. Mehnke, T.Wernicke, H. Pingel, C. Kuhn, C. Reich, V. Kueller, A. Knauer, M. Lapeyrade, M. Weyers, and M. Kneissl, Apply Phys. Lett., **103**, 212109 (2013)

[12] Kazutada Ikenaga, Akira Mishima, Yoshiki Yano, Toshiya Tabuchi, and Koh Matsumoto, Jap. J. of Appl. Phys., **55**, 05FE04 (2016)